COHERENT LIGHT GENERATION VIA COLLECTIVE AND QUANTUM COHERENCE PROCESSES AND BRILLOUIN MICROSCOPY

A Dissertation

by

ANDREW JOSEPH TRAVERSO

Submitted to the Office of Graduate and Professional Studies of
Texas A&M University
in partial fulfillment of the requirements for the degree of

DOCTOR OF PHILOSOPHY

Chair of Committee,	Vladislav V. Yakovlev
Committee Members,	Marlan O. Scully
	Alexei V. Sokolov
	Simon W. North
Head of Department,	George R. Welch

May 2016

Major Subject: Physics

ABSTRACT

New approaches for generating coherent light are of keen interest to the scientific community due to the increasing demand for unique sources tailored to specific applications. In fields like microscopy, remote sensing, and soft X-ray/XUV lasers this interest is especially pronounced as novel techniques would have a profound impact. Here, we present new methods for generating coherent light by inducing collective coherence in the gain medium. In particular, we demonstrate coherent emission produced through four-wave mixing on a dressed state, stimulated Raman by inducing coherence between two vibrational levels via 2-photon coupling, and finally, a remote atmospheric coherent source via strong-oscillatory superfluorescence in atomic oxygen. Four-wave mixing on a dressed state could be used to generate XUV coherent radiation or remote atmospheric sensing, as it produces both a forward and backward propagating field. We observe this in Rb vapor with emission occurring at detunings of up to 30 nm from the transition. Similarly, 2-photon enhanced stimulated Raman could be implemented for XUV generation as well, due to the asymmetric gain observed on the anti-Stokes emission relative to the Stokes in Methane. It is also a great platform for microscopy as it is background-free unlike other conventional methods like CARS and CSRS. Atmospheric lasing via oxygen is a prime candidate for next-generation remote sensing techniques, and here we study its emission mechanisms in depth demonstrating that superfluorescence serves as the main driving process for the observed 845 nm generation. This intense strong-oscillatory emission lends itself for use in coherent Raman techniques. Furthermore, a dual Raman-Brillouin microscope is also presented and demonstrated, which could prove to be a powerful new tool in biomedical and material characterizations applications.

DEDICATION

For My Parents

TABLE OF CONTENTS

Page

LIST OF FIGURES

FIGURE Page

1. INTRODUCTION

The invention of the laser provided an invaluable tool for precision measurements and manipulation of physical systems throughout almost all fields of science and engineering [28, 62]. The key to this advancement came from the unprecedented level of control of the properties of light including its wavelength, duration, energy, phase, and spectral width. As the applications for coherent light have steadily increased so too has the desire for novel approaches to generate coherent light that will push past our current limitations. These limitations in intensity, duration and wavelength ultimately stem from the initial generation of the coherent light.

As it stands, the conventional method of light generation through population inversion has flourished with technologies such as diode, solid state, dye, and gas lasers. These technologies paired with the advent of nonlinear optics techniques such as parametric amplification, and sum (difference) frequency generation have created a diverse menagerie of available coherent sources. Even so, there are still limitations to these technologies as certain wavelength regimes are largely inaccessible. For example, the XUV/X-ray regime offers very few choices [8, 101]. This is due to the difficultly in achieving population inversion as most XUV/X-ray transitions possess too short of a lifetimes and most nonlinear crystals are likely to burn in this frequency regime. In this and other cases an alternative approach would be very attractive.

One such general approach that has garnered considerable interest utilizes the coherence of the gain medium to produce coherent light. This covers a broad swathe of techniques such as superfluorescence, superradiance, lasing without inversion, Mollow gain, and coherent Raman [122, 20, 97, 72]. While these techniques have substantially different implementations they all bypass the need for population inversion

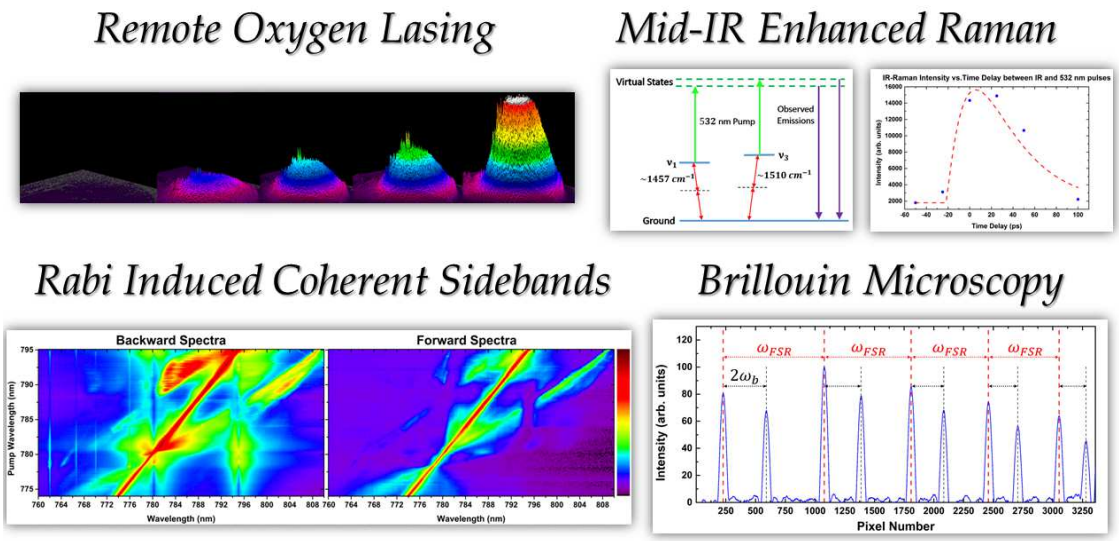

(except for superfluorescence which initiates with an inverted population). Instead most require a strong driving field to induce the coherence and provides a very fine control over the emission process. Beyond this, these processes exhibit other unique characteristics such as bidirectional emission which makes it a very attractive choice for remote sensing applications [37, 106, 118, 48]. Overall, coherence driven emission is a very rich area of study with untapped potential for applications.

1.1 Topics

Fast Rabi Induced Sideband Emission

Here, we describe a unique method for generating directional coherent emission that could be utilized for XUV/X-ray generation and other applications. This approach offers two distinct advantages: it does not require population inversion, and the coherent light is produced very simply by optically pumping a two level transition with a strong field far detuned from resonance. Once produced, the light propagates in both the forward and backward direction along the pump beam and is frequency

shifted further away from resonance than the pump field-i.e. if the pump is blue (red) detuned from the transition, the emission is further blue (red) detuned. We demonstrate detunings of up to 30 nm with a 5 J, 6 ps pump in Rubidium (Rb) vapor. Larger detunings and different wavelength regimes are achievable by scaling up the pump energy and employing different atomic/molecular ensembles.

Coherence Brightened Laser Source for Atmospheric Remote Sensing

We have studied coherent emission from ambient air and demonstrated efficient generation of laser-like beams directed both forward and backward with respect to a nanosecond ultraviolet pumping laser beam [106, 117, 119]. The generated optical gain is a result of two-photon photolysis of atmospheric O_2, followed by two-photon excitation of atomic oxygen. We have analyzed the temporal shapes of the emitted pulses and have observed very short duration intensity spikes as well as a large Rabi frequency that corresponds to the emitted field. Our results indicate that the spiky emission process is due to quantum coherence via cooperation between atoms of an ensemble, which leads to strong-oscillatory superfluorescence. These cooperative nonadiabatic coherence effects cannot be described by rate equations and instead a full set of the Maxwell-Bloch equations must be used. This is similar in nature to Dicke superradiance where atomic coherence is large and can be contrasted with ordinary lasing where atomic coherence is negligible. Understanding this coherence-brightened process in air should lead to improvements in environmental, atmospheric remote sensing and other applications.

Mid-IR Enhanced Coherent Raman

Here, we study a novel scheme for coherent Raman replacing the pump and stokes coupling between the two vibrational states with a mid-infrared (Mid-IR) field which is two-photon resonant with the vibrational transition. The use of the Mid-IR field

provides a much stronger coupling between the vibrational states than the usual pump/Stokes scheme as the detunings from the intermediate level are significantly smaller for the Mid-IR coupling. We demonstrate this process in methane gas using a 6.7 m, 30 ps source for the Mid-IR coupling and a 532 nm, 40 ps source as the probe field. We then construct a generalized analytical model to characterize its unique behavior.

Dual Raman Brillouin Microscope

We present a unique confocal microscope capable of measuring the Raman and Brillouin spectra simultaneously from a single spatial loca-tion. Raman and Brillouin scattering offer complementary information about a materials chemical and mechanical structure, respectively, and concurrent monitoring of both of these spectra would set a new standard for material characterization. We achieve this by applying recent innovations in Brillouin spectroscopy that reduce the necessary acquisition times to durations comparable to conventional Raman spectroscopy while attaining a high level of spectral accuracy. To demonstrate the potential of the system, we map the Raman and Bril-louin spectra of a molded PEGDA hydrogel sample in cyclohexane to create two-dimensional images with high contrast at microscale resolutions. This powerful tool has the potential for very diverse analytical applications in basic science, industry, and medicine.

2. FAST RABI INDUCED SIDEBAND EMISSION

New approaches for generating coherent light are of keen interest to the scientific community due to the ever increasing demand for unique sources tailored to specific applications. In certain fields like remote sensing and soft X-ray/XUV lasers this interest is especially pronounced as a novel technique would have a profound impact[8, 48, 37, 118]. Here, we describe a unique method for generating directional coherent emission that could be utilized for these and other applications. This approach offers two distinct advantages: it does not require population inversion, and the coherent light is produced simply by optically pumping a two level transition with a strong field that is far detuned from resonance. Once produced, the light propagates in both the forward and backward direction along the pump beam and is shifted in frequency further away from resonance compared to the pump field-i.e. if the pump is blue (red) detuned from the transition, the emission is further blue (red) detuned. We demonstrate detunings of up to 30 nm with a 5 μJ, 6 ps pump in Rubidium (Rb) vapor. Larger detunings and different wavelength regimes are achievable by scaling up the pump energy and employing different atomic/molecular ensembles.

The main difficulty for realizing a tabletop X-ray laser by conventional methods is achieving population inversion due to the extremely short lifetimes of the XUV/X-ray transitions. As such, there have been many proposed alternative methods[30, 75, 105] that attempt to overcome this constraint. Among the most successful of these are plasma-assisted lasing[41, 67, 102] which achieves population inversion by ionization/recombination, and high harmonic generation[87, 81] which bypasses the need for population inversion altogether. Despite these successes, there is still a

limited selection of accessible wavelengths and an overall lack of sources within this regime.

Similarly, the use of advanced nonlinear techniques in atmospheric remote sensing has been hindered by the lack of a practical method to generate a counter-propagating coherent source. While there has been some marked success in developing such a technique utilizing the oxygen and nitrogen in the atmosphere as a gain medium[21, 106, 43, 50], these techniques rely on an intense UV pump source, which is not feasible due to the high absorption and scattering rates in atmosphere. A technique that produces a counter-propagating source without the need of a UV pump would have a much easier path to practical implementation.

In this chapter, we propose and demonstrate a unique approach for coherent light generation achieved by coupling a far detuned intense pump field to a two level system. The pump field induces AC Stark splitting in the system and subsequently drives four-wave mixing (FWM) across the transiently split levels. The medium then emits directional, coherent light detuned from the pump frequency by the effective Rabi frequency on a timescale faster than the coherence time of the system, hence the moniker Fast Rabi Induced Sideband Emission (FRISBE). FRISBE is bi-directional in nature, does not require population inversion, and should be attainable in most atomic/molecular systems. Given these attributes, it is a prime candidate for remote sensing and XUV/X-ray applications as well as a potential alternative to other technologies such as parametric generation and chirped pulse amplification (CPA).

It has been demonstrated that it is possible to achieve gain from a strongly driven two level atom even in the absence of population inversion. This effect is called "Mollow gain", and was first shown in sodium gas[72, 113]. Mollow gain is an essentially single atom process, but it was predicted by Boyd[12, 2] that for propagation through dense media, it can be a source of gain that drives non-linear four-wave mix-

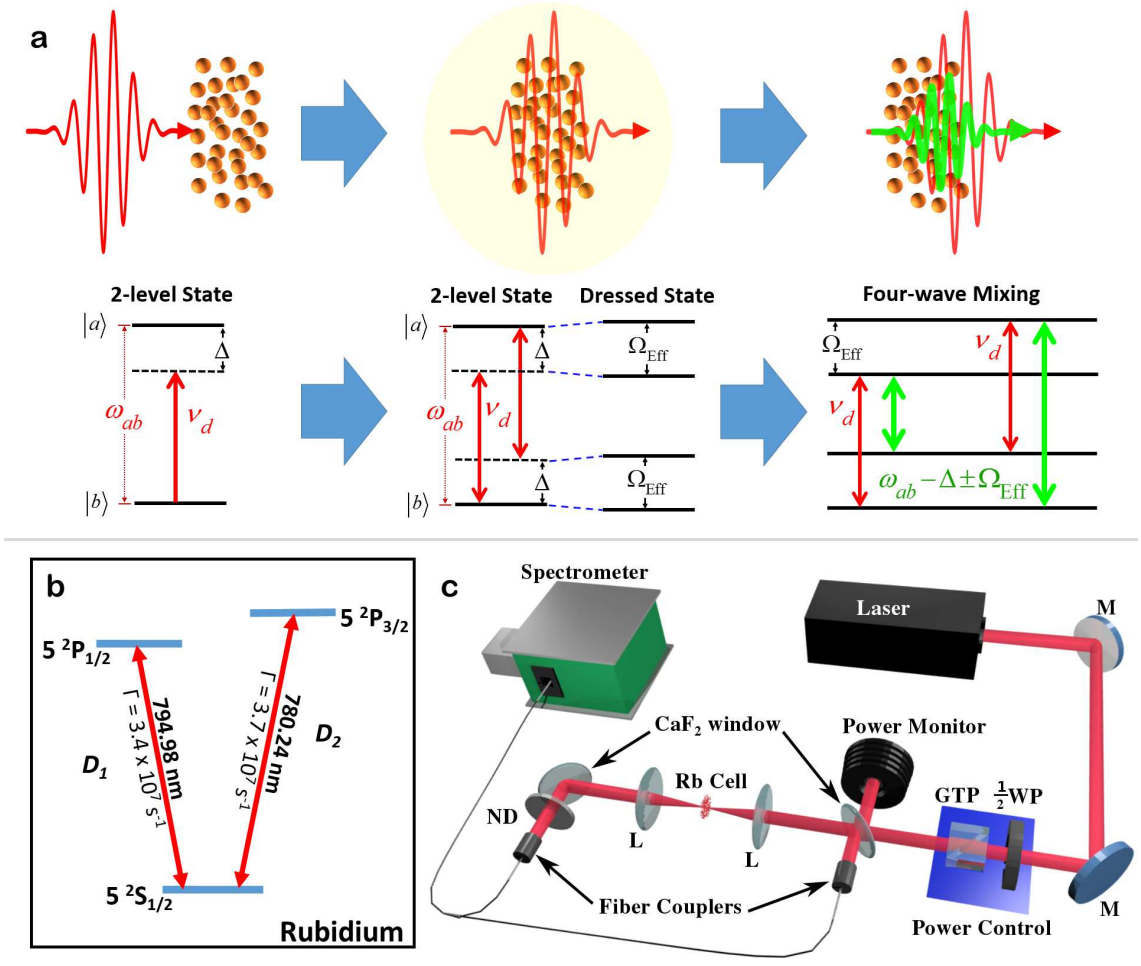

Figure 2.1: **Experimental Setup (a)** Evolution of a two-level system into a Autler-Townes split 4 level picture where both the upper and lower doublet are split by the effective Rabi frequency Ω_{Eff}. Resonant Four wave mixing then occurs where the pump laser acts as both the pump and probe field. **(b)** Simplified energy level diagram of Rubidium atom. Pump laser is tuned from below D_1 line to above D_2 line. **(c)** Diagram of experimental setup. A tunable CW ECDL near 780 nm is used to seed an OPA comprised of a LBO crystal pumped with a 1 mJ 6 ps 532 nm laser. In the figure above the abbreviations represent the following: M-Mirror, Rb-Rubidium Cell, ND-Neutral Density Filter, L-Lens,GTP-Glan-Thompson Polarizer , HWP-Half-wave Plate.

ing (FWM) which can lead to sideband generation. This was proposed as a way to explain "anomalous" sideband generation in atomic vapor, but it is currently unclear whether this is the primary mechanism, as several plausible alternatives were also proposed[51, 16, 26, 19]. In most cases the side-band generation seen in experiments, was seen near resonance and lead to conical emission for one of the sidebands[29, 34]. The difficulty arises because most of these experiments were performed with pump detunings of less than 300 GHz, and near resonance their are other significant effects that come into play such as self-focusing, self-trapping, and substantial changes to the refractive index. In contrast, our studies focus on detunings greater than 300 GHz where near-resonant effects play a negligible role, such that the observed emission is only along the beam path. To adequately explain our observations, we extend Boyd's approach into the non-steady state regime, and to the case of large pump detunings.

To understand this phenomenon, it is useful to consider a two level system with transition frequency ω_{ab} between the ground state $|b\rangle$ and excited state $|a\rangle$ driven by a strong field ν_d (Fig. 2.1a). If the field is strong enough such that the Rabi frequency, $\Omega_d = \frac{\wp \cdot E}{\hbar}$, is comparable to detuning, $\Delta = |\omega_{ab} - \nu_d|$, then the field will induce AC Stark splitting in both the ground and excited states (E is the electric field amplitude and $\wp$ is the electric dipole moment of the transition). Given the energy level splittings, It is convenient to use a "dressed state" picture for a better qualitative illustration of the dynamics(Fig. 2.1a). In the dressed state description, the bare two level system transforms into a four level system where the levels are defined by the eigenstates of the convolution of the atomic system with the driving field. This gives a splitting equal to the effective Rabi frequency, $\Omega_{\text{Eff}} = \sqrt{\Omega_d^2 + \Delta^2}$, for each of the doublets.

Conceptually, this process is analogous to a coherent Raman process driven in

resonance where the pump acts as both the pump and probe fields[12, 34]. The significant difference is that the energy levels in the dressed state picture only exist during the lifetime of the coherence. Initially, the strong drive field induces Mollow gain in the medium producing a weak omni-directional field at the effective Rabi frequencies. Then due to the interaction between the dressed-state energy levels and strong pump field, the Rabi detuned fields are amplified by FWHM in the transient regime as they propagate along the pencil-like pump region. The resulting emission is both in the forward and backward directions with frequencies $\nu_d \pm \Omega_{\text{Eff}}$ while absorption in the gain region occurs at ν_d. For this process to transpire, the coherence must play a significant role, meaning both the Rabi frequency, Ω_d, and the collective atomic frequency, Ω_A, must be much greater than the largest dephasing rate in the system.

2.1 Experiment

To demonstrate FRISBE generation, we chose to study the process in rubidium (Rb) vapor as Rb has a high vapor density at relatively low temperatures and possesses two strong near-infrared (NIR) transitions from the ground states: D_2 $(5^2S_{1/2} \rightarrow 5^2P_{3/2})$ and D_1 $(5^2S_{1/2} \rightarrow 5^2P_{1/2})$ (Fig. 2.1b). Given that the $5^2P_{1/2} \rightarrow 5^2P_{3/2}$ transition in Rb is forbidden and only couples through collisions, we can treat the D_1 and D_2 transitions in Rb atom as two separate uncoupled oscillators. From the dressed state picture, we know that a single two level system will produce two sidebands. Therefore, one would expect Rb, modeled as two uncoupled oscillators, to produce 4 sidebands in total, but this is not the case. In actuality only a single sideband is expected for each oscillator as a single sideband for each 2 level system is nearly degenerate with its respective atomic transition and therefore gets absorbed.

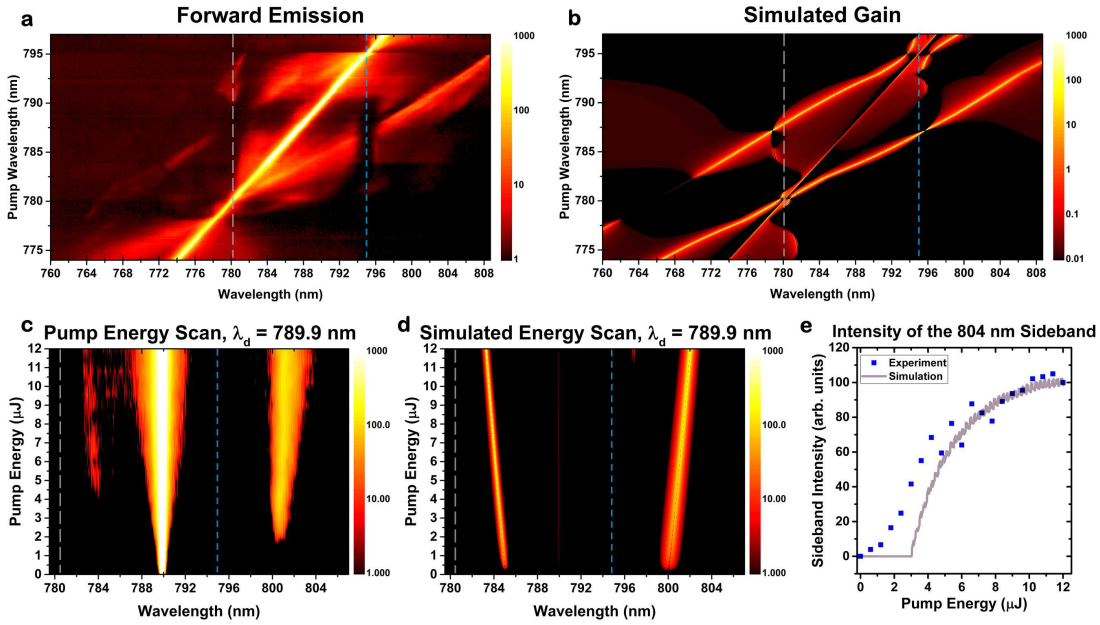

Figure 2.2: **Forward Emission and Simulations (a)** 2D intensity map of the observed emission in the forward direction using a $\sim 10\mu$J pump scanned from 775 to 797 nm. **(b)** 2D map of the simulated gain using a Rabi Frequency of 1.2 THz. The strong central bright field in both **(a)** and **(b)** is indicative of the laser field, whereas the two arms that intersect the laser field at the D_1 and D_2 (795 and 780 nm respectively) are the emitted sidebands. The sideband due to the D_2 and D_1 range from 767 to 808 nm and 762 to 796 nm, respectively. **(c)** 2D intensity map of the observed emission in the forward direction as the pulsed energy was increased and the pump was held constant at 790 nm **(d)** 2D map of the simulated gain in the forward direction as the pump energy was increased and the pump wavelength remained constant at 790 nm. **(e)**(e) Sideband intensity versus the pump energy. The blue dots are the experimental measurements along the sideband at 804 nm. The solid grey curve is the corresponding simulation result.

The Rubidium cell was optically pumped using a narrowband (<0.2 nm linewidth) 6 ps laser tunable from 763 to 798 nm with a maximum pulse energy of 10 μJ focused into the Rb using a 7.5 cm plano-convex focusing lens. The Rubidium itself was enclosed in 2 mm long heated Sapphire cell and heated to temperatures between 200° and 310° C providing Rb densities ranging from approximately 8×10^{14} cm^{-3} to 3×10^{16} cm^{-3}. Given these parameters, the Rabi frequency and atomic drive frequency were estimated to be on the order of $\Omega_d \sim 1$ THz and $\Omega_A \sim 3 \times 10^{13}$ rad/s, respectively. A spectrometer was used to monitor the emission from the cell in both the forward and backward direction as well as orthogonal to the pump beam path to verify directionality.

Initial results revealed two bright emission peaks with detunings from the pump frequency, ν_d, matching the respective effective Rabi frequencies for the D_1 and D_2 transitions. This sideband emission was observed in both the forward and backward direction along the pump beam. While emission from the side was also detected, it was approximately three orders of magnitude weaker. For a full characterization of the emission, the pump wavelength, pump energy, and Rb density were independently varied. The results of the wavelength and energy study are depicted in Fig.2.2.

To verify this behavior, various control experiments were performed. The first of which was just confirm the overall directionality of the emission. To do this, the emission gain region was probed from 90° using a 7.5 cm collection lens and fiber aperture just as was done in the backward direction. To further ensure that the observed backward and side emission could be compared, the emission from both was normalized using the fluorescent lines as the fluorescence expands out uniformly in 4π and thus should be equivalent in every direction. The result of this study can be seen in Fig.2.3. Here, we see that the emission from the side is approximately 1.25% relative to the emission observed in the backward direction. Given that the

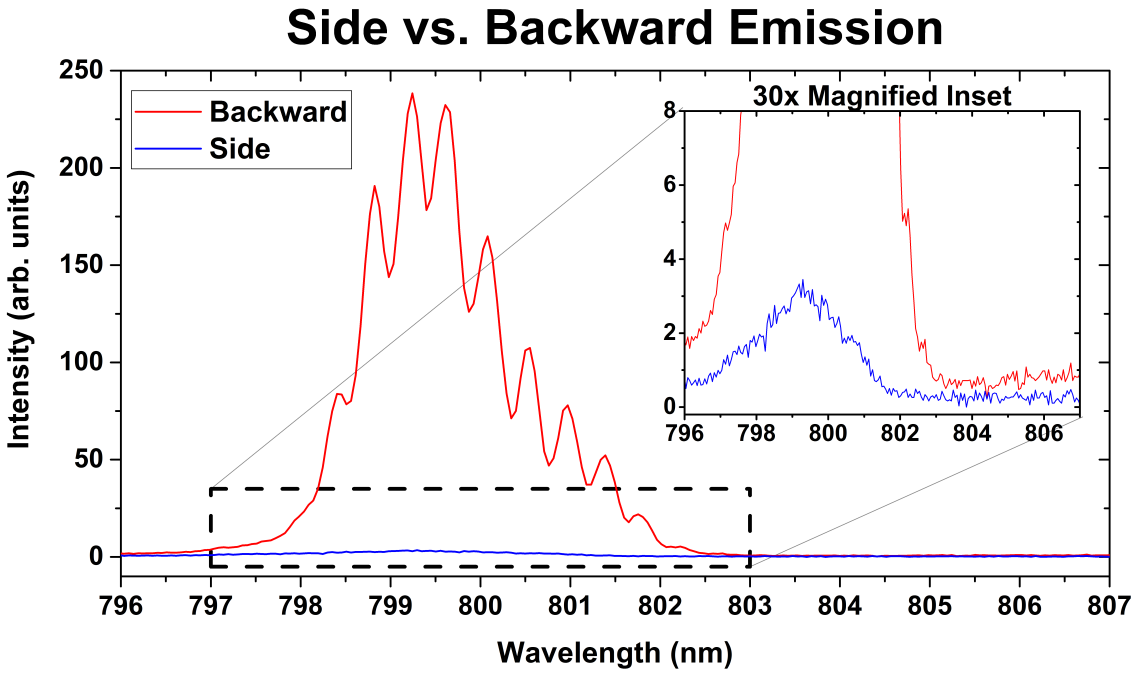

Figure 2.3: **Directionality of Emission** Backward sideband emission compared to sideband emission observed at a 90° angle relative to the pump path. The spectra were normalized using fluorescent lines when the pump source was on resonance in both cases as fluorescence emits uniformly in 4π.

Rb is housed in a sapphire cell, this 1.25% sideband emission observed from the side most likely originates from a reflection of the glass of the cell as glass usually has partial reflections that are approximately 1% to 5% of the main pump source.

To further explore the nature of this emission, similar wavelength and pump power scans were performed using using just the continuous wave (CW) seed laser as the pump source. This CW laser had a maximum output of ∼100 mW and an identical scan range from 765 to 797 nm. The results of the wavelength study depicted in Fig.2.4. In the case of the forward direction, Fig.2.4a reveals that not much is occurring in the CW regime other than absorption of the pump field when near resonance with with the D_1 and D_2 transitions of Rb. Just as with the ps pulses, the pump field is too strong to observe any fluorescent lines without saturating the detector.

In contrast, the backward direction (Fig.2.4b) reveals many interesting features that were also observed in the picosecond pulsed regime. Here, we see the fluorescent lines from the higher Rb transitions when the pump is in near resonance with the D_1 and D_2, but when the pump is directly on resonance with either one, these fluorescent lines disappear. This is likely due to the absorption of pump outside of the focal region by the surrounding Rb. A much larger population of Rb would then absorb radiation of the pump beam and would leave much less of the pump beam to significantly drive those higher transitions. Furthermore, when the pump beam is slightly off-resonant with one of the D_1 and D_2 transitions, butterfly-like emission is observed on both the near resonant transition as well as the far detuned one. This is likely due to significant population transfer through collisions as well as radiation trapping on the transition in the focal volume[58].

With the forward and backward emission in Fig.2.4, we can now make statements about what is the likely cause of certain features observed in the picosecond pump-

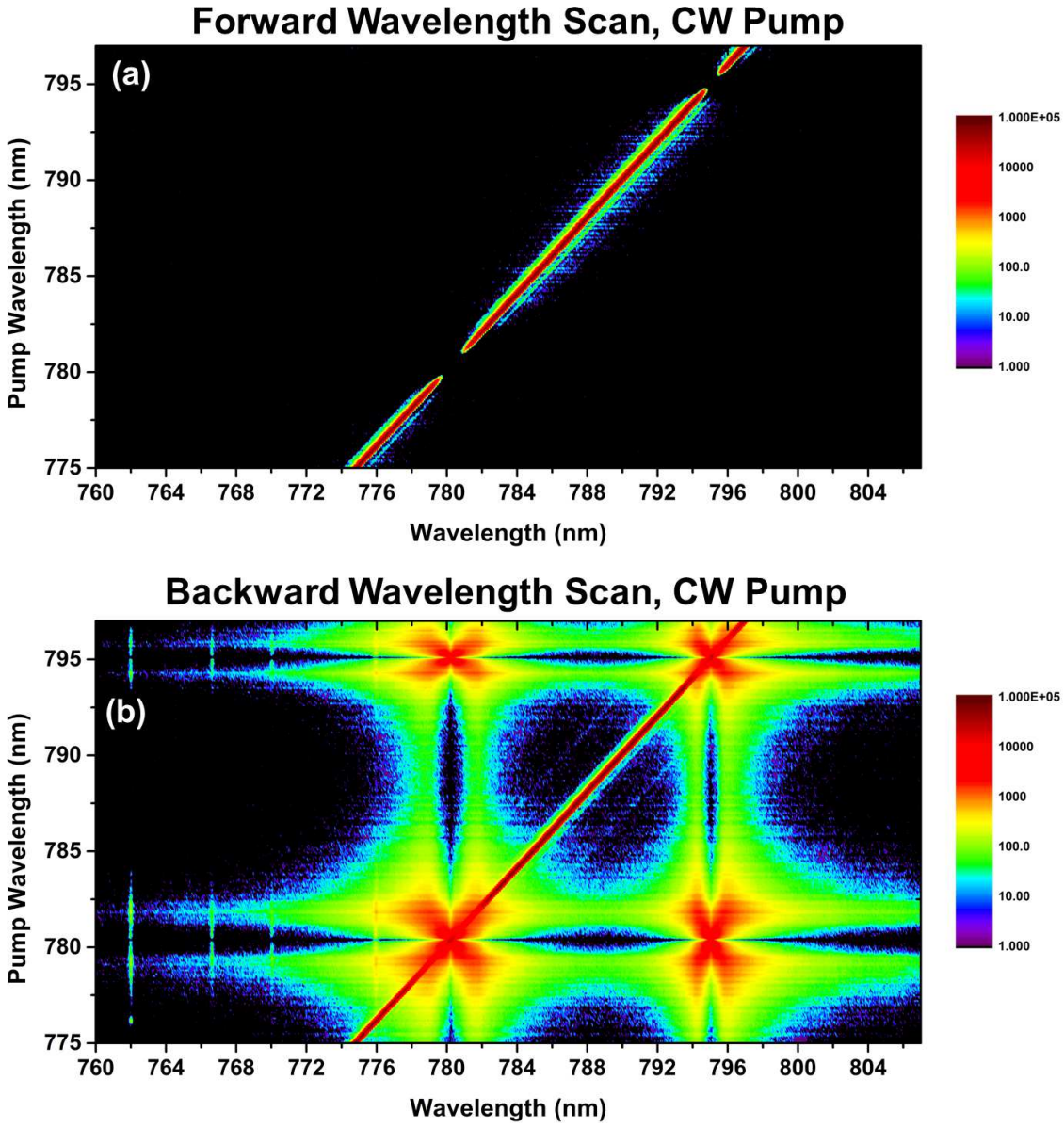

Figure 2.4: **CW Experimental Wavelength Scan (a)** Observed forward emission when a CW pump is scanned from 770 to 797 nm. Strong absorption is observed when the pump is near either of the ground state D_1 and D_2 transitions **(b)** Backward emission for a similar CW pump wavelength scan. Fluorescence from higher order transitions are observed as well as radiation trapping on the D_1 and D_2 transitions at 795 and 780 nm respectively.

ing experiment in Fig.2.2a and Fig.2.7a. Here, we can confirm that the higher order transition lines in Fig.2.7a are just in fact from fluorescence and the butterfly-like features cannot be attributed to any high intensity or coherence effect caused solely by the picosecond pulse. In contrast, the sideband emission observed in the picosecond pumping results is nowhere to be found, which means the sideband emission is entirely due to the intense pumping in the picosecond regime.

Further experiments with the CW pump were undertaken where the pump power was varied while the pump wavelength was held constant at 794.9 nm (Fig.2.5a) and 780.24 nm (Fig.2.5b) so that the pump would be resonant with the D_1 and D_2 transitions, respectively. The emission was observed in the backward direction, as the weak features in the forward direction are not observable without saturating the detector due to the pump beam. In both cases, significant emission was observed on the off-resonant transition, which is highly indicative of significant population transfer through collisions when the pump on (and near) resonant with one of the transitions. This type of effect will likely make modeling the emission process very difficult when the pump field is close to resonance as this population transfer is not insignificant.

To understand the nature of the emission, analytic expressions were derived such that the spectral gain is given as a function of the pump frequency, ν_d, and Rabi frequency, Ω_d, as well as the density of the gas:

$$A_3(z) = \left[\frac{(e^{g_+ z} - e^{g_- z})\left(\kappa_3 A_4^0 - \left(g_- + \alpha_3 + \frac{i\Delta k}{2}\right)A_3^0\right)}{(g_+ - g_-)}\right] e^{\frac{i\Delta k}{2}z} \tag{2.1}$$

$$A_4^*(z) = \left[\frac{(e^{g_+ z} - e^{g_- z})\left(\kappa_4^* A_3^0 - \left(g_- + \alpha_4 + \frac{i\Delta k}{2}\right)A_4^0\right)}{(g_+ - g_-)}\right] e^{\frac{i\Delta k}{2}z} \tag{2.2}$$

Where A_3 & A_4 are the Stokes and anti-Stokes fields respectively, κ_i & α_i are coef-

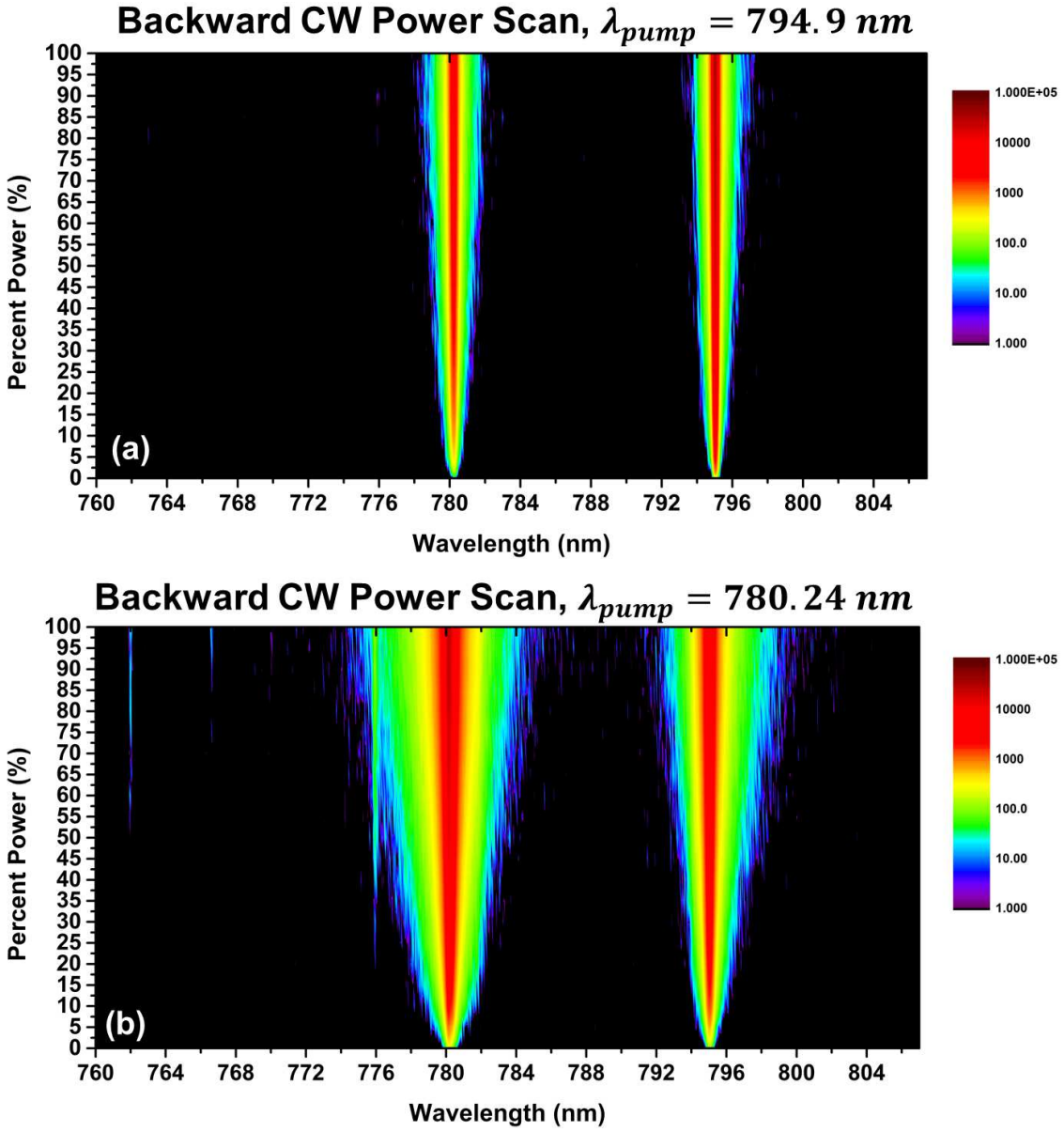

Figure 2.5: **CW Experimental Power Scan (a)** Observed backward emission when the pump power is varied for a CW laser held at 794.9 nm near the D_1 transition of Rb. **(b)** Similarly observed backward emission for a CW laser held at 780.24 nm near the D_2 transition of Rb. In both cases, emission is seen at the off-resonant transition, indicating significant population transfer through collisions.

ficients defined later, and $g_{\pm}$ are the gain coefficents given by:

$$g_{\pm} = \pm\frac{\sqrt{(\alpha_3-\alpha_4+i\Delta k)^2+4\kappa_3\kappa_4^*}-(\alpha_3+\alpha_4)}{2} \tag{2.3}$$

More details about this approach are included later in this chapter.

Following this treatment and using values closely matching experimental parameters, simulations of the gain were performed to confirm the behavior of the emission (Fig. 2.2b & 2.2d). When the pump wavelength is scanned, the model predicts gain at wavelengths detuned from the pump by the effective Rabi frequencies. For the D_1 & D_2 transitions of Rb, this corresponds to gain at two distinct wavelengths, a single sideband for each transition, that moves further from both the pump and transition wavelength as the detuning is increased(Fig. 2.2b). This result is extremely consistent with our experimental observations (Fig. 2.2a).

Similarly, the pump energy study revealed close agreement between experiment and simulations where both exhibited threshold-like behavior (see Figs.2.2c-e. This threshold is caused by the coherence reaching a critical level such that gain overcomes the decoherence of the system. Furthermore, as the pump energy was increased the observed sidebands became further detuned which is in keeping with our model as the effective Rabi, Ω_{Eff}, is dependent upon the pump energy. This shift was especially evident when the pump beam detuning, Δ, was very small in comparison to Ω_d. This is highly indicative that the sideband emission is driven by the coherence of the system.

A threshold-like behavior was also expected and observed when the Rb density was increased2.6. Unlike scanning the pump energy or frequency, the frequencies of the sideband emission remain unchanged as the density is changed. This behavior arises from the need to achieve a critical atomic drive frequency, Ω_A, which is directly

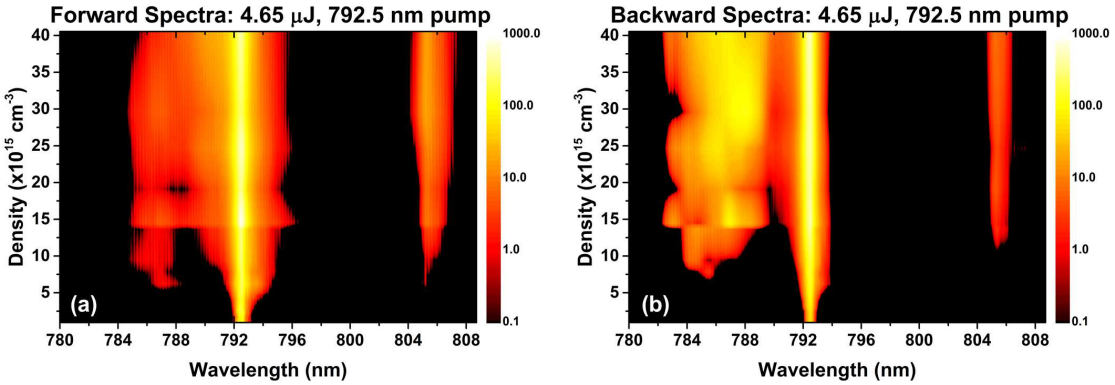

Figure 2.6: **Atomic Density Dependence of Sideband Emission** Spectral measurements of the forward **(a)** and backward **(b)** emission from Rb vapor as a function of atomic density with a fixed pump wavelength of 792.5 nm.

dependent upon the density. Once Ω_A is greater than the decoherence rate, the gain can scale with the length as the emission propagates through. Given the long pencil-like geometry of our gain region, this also provides directionality along the pump path for the emission. This threshold was observed at a Rb density of approximately $\sim 2 \times 10^{15}$ cm^{-3} (~ 220°C).

The observed backward emission exhibited nearly identical behavior as the forward emission(see Fig.2.7). In fact, while the sideband emission behaved identically, our observations in the backward direction proved to be more information-rich due to the lack of the strong driving pump. Without the intense pump field, weaker signals such as fluorescence were observable providing useful information about the population dynamics. In particular, when the pump field was near resonant with the D_1 or D_2 transition, emission at the off-resonant transition was observed as well as fluorescence from some of the upper excited states of Rb. These additional features are indicative of significant population transfer and more complicated dynamics when the pump is near resonant. Conversely, when the pump is far from resonance, these

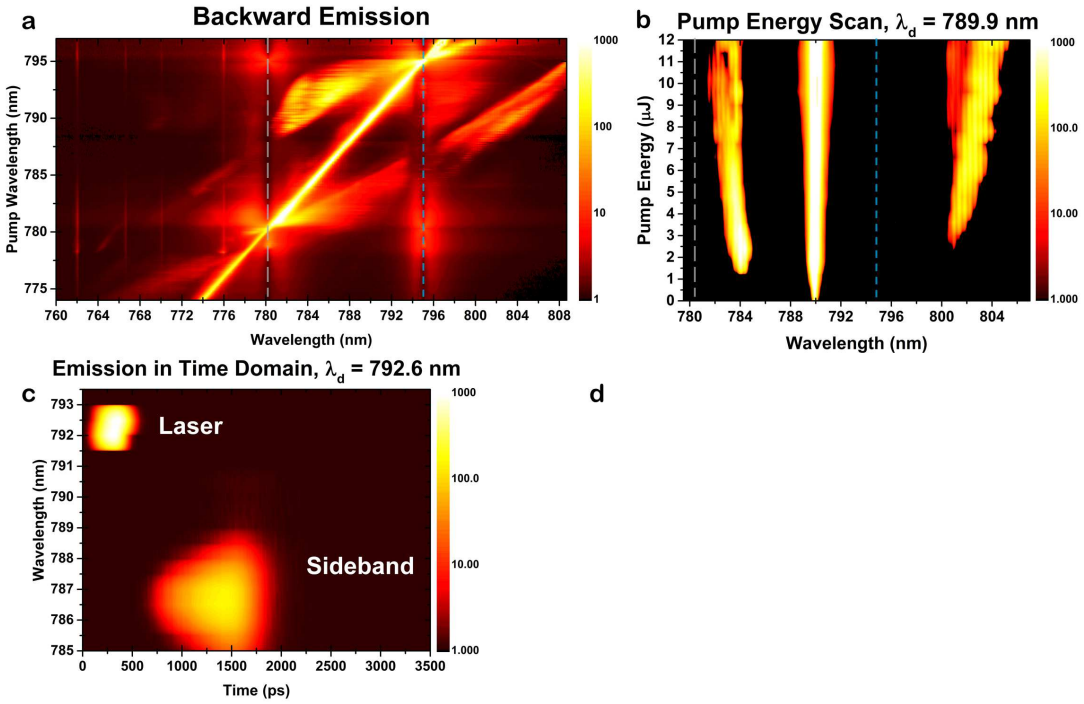

Figure 2.7: **Backward Emission Characteristics and Temporal Dynamics** Spectral measurements of the backward emission from Rb vapor as a function of pump wavelength **(a)** and pump energy **(b)**. **(c)** time-resolved emission of the sidebands. The sideband at 786 nm emits in less than 1 ns, which is on the order of the estimated decoherence time of the system. **(d)** Simulation of the time-resolved sideband emission(CHRIS).

features disappear allowing for a simpler treatment of the system as two separate two-level systems. These additional fluorescent lines were also observed using a CW field as well. No sideband emission was detected using the CW pump.

Next, to characterize the sideband emission in the time domain, we measured the backward emission using time correlated spectral measurements, i.e. a monochromator was paired with a single photon counting photo-multiplier tube (PMT) where the PMT acted as the detector on the output of the monochromator. The pump laser wavelength and monochromator were then alternately scanned to create spectral time profiles. The sideband emission was observed to be time delayed from the laser pulse $\sim 1\ ns$. This is in keeping with our predictions as the coherence needs time to develop before any emission can occur out of the dressed state. The sideband emission duration is much faster (< 1 ns) than the spontaneous emission rate for either of the Rubidium transitions, thus ruling out any fluorescence process and follows the decoherence rate set by the Rb-Rb collision rate of ~ 1 GHz. This short, intense nature of the sideband emission makes it perfectly suited for use in other techniques like coherent Raman, two-photon spectroscopy, and other nonlinear processes.

The time domain setup was also used to characterize the butterfly-like emission as a function of pump energy and atomic density. These features are only observed when the pump was on-resonant with either the D_1 or D_2 transition. Therefore, the laser was held at 795.1 nm, near the D_1 transition, and the backward emission was probed at 780.1 nm near the D_2 as the pump energy and density were varied. The results of these studies are seen in Fig. 2.8. There seem to be two very distinct emission processes occurring, the first of which is a fast emission that occurs right as the pump pulse is propagating through the medium (the pump pulse occurs at ~ 8.5 ns). This quick emission does not seem to have any dependence on the density (Fig. 2.8a), but relies heavily on the pump energy (Fig. 2.8b) where it appears to grow

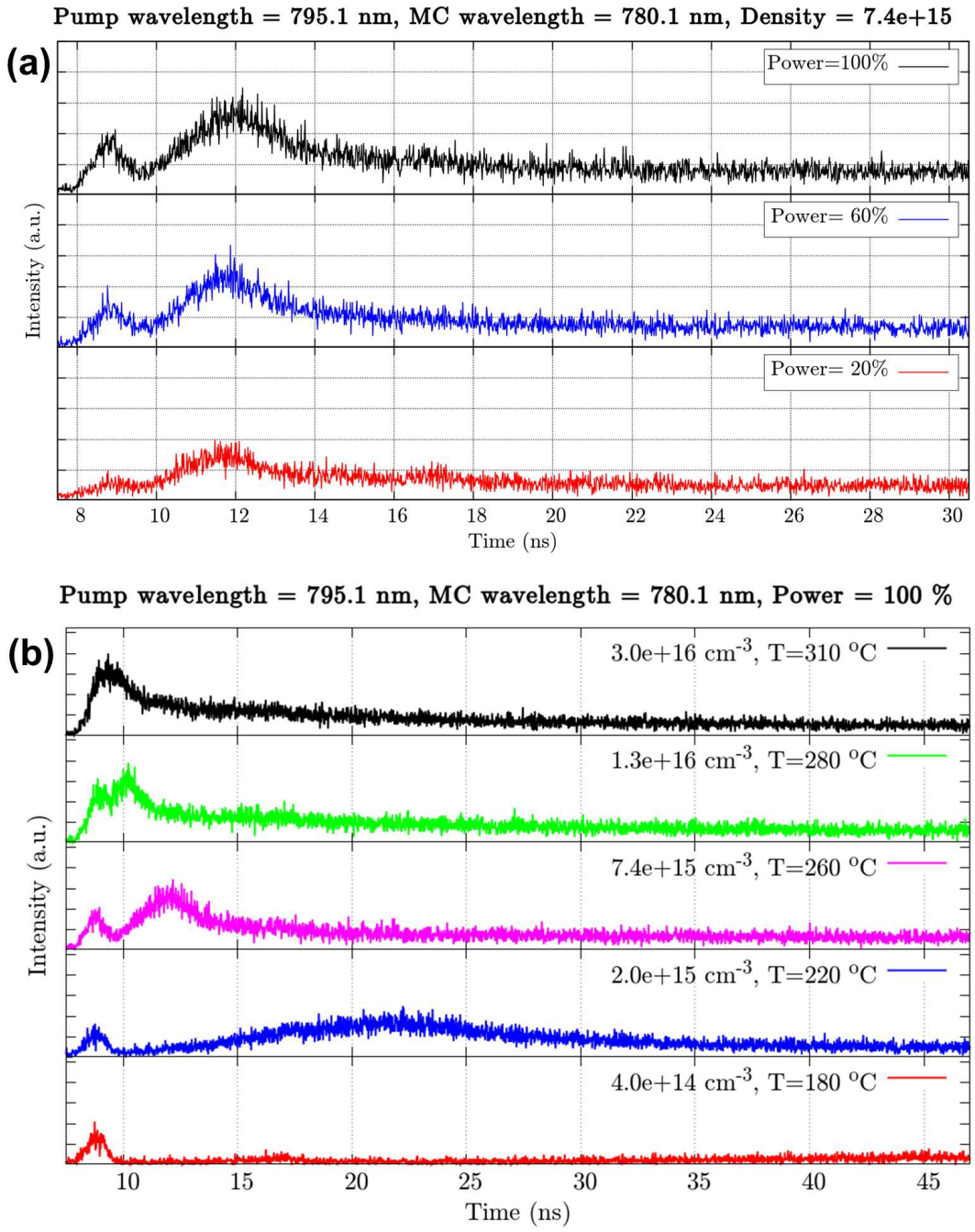

Figure 2.8: **On-Resonance Temporal Dynamics** Temporal measurements of the backward emission from Rb vapor as a function of pump power **(a)** and pump energy **(b)**. The Pump laser was held at 795.1 nm while the emission at 780.1 nm was measured.

at a greater than linear rate. This type of behavior implies that it is likely driven by a superradiant process where the upper state of the D_2 transition is populated either by collisions or four-wave mixing between the two transitions and emits in the timespan of the pulse passing through the medium.

The second emission process definitely changes with density and appears to only grow linearly with increasing pump energy. At low atomic densities (Fig. 2.8b), the emission is extremely weak and substantially delayed by up to ~ 20 ns from the pump pulse. With increasing density, the delay shrink and the overall duration of this emission process also decreases. This process is likely driven solely by population transfer through collisions and is indicative of simple fluorescence. This accounts for the shortened delay with increasing density as the collision rate would increase allowing for a quicker population transfer between the two states. Furthermore, with an increased collision rate, the radiative decay would also increase substantially, accounting for the shortened duration of this emission. While it is interesting that there appears to be a superradiant-like process occurring along with fluorescence, this is generally to be expected. Any time an atomic is resonantly pumped with an intense drive field, some amount of superradiance/superfluorescence is likely to occur.

Lastly, we explored FRISBE's ability to generate coherent XUV light by extending our simulations to other atomic species. There are two potentially viable approaches for XUV FRISBE generation. The first approach utilizes a pump field red-detuned from an XUV transition, whereby an anti-Stokes sideband is produced that is very nearly resonant with the XUV transition ($\nu_d + \Omega_{\text{Eff}} \approx \omega_{ab}$). The key and challenge to this approach is generating the sideband such that it is detuned from the transition thereby avoiding absorption and other near-resonant distortions, which requires the Rabi frequency, Ω_d, to be on the order of the pump detuning, Δ.

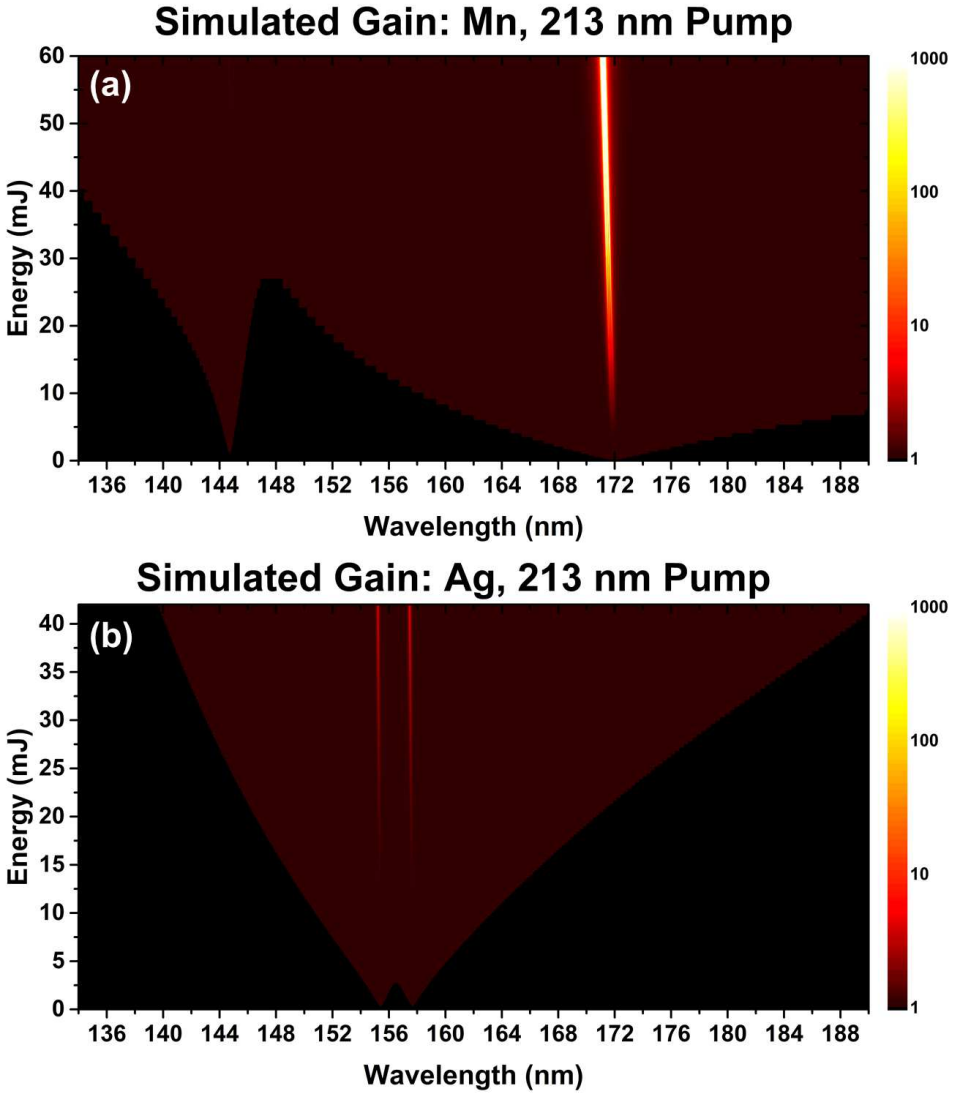

Figure 2.9: **XUV Simulation in Magnanese and Silver(a)** Simulation for a 213 nm pump field in Mn vapor ($1*10^{16}$ cm^{-3}). **(b)** Simulation in Silver vapor using the same atomic density and pump wavelength.

The other method relies on a UV pump source that is blue-detuned from a transition with a large dipole moment. Here in Fig.2.9, we simulated a 213 nm pump source (5th harmonic of Nd:YAG) in manganese (Mn) vapor. Manganese was an attractive choice due to its two sets of strong ground state transitions at 403 and 279 nm, lack of XUV ground state transitions, and high ionization level (approximately 7.4 eV). As depicted in Fig.2.9, the gain produced at approximately 145 nm and 172 nm correspond to sidebands from the 403 and 279 transitions, respectively. The difference in strength between the two sidebands is mainly due to the much larger dipole moments for the 279 transitions. Similar simulations in Mn with pump wavelengths up to 250 nm also depicted FRISBE gain below 200 nm. While these simulations in Mn are promising, there are many other potentially viable atomic species for XUV generation including Silver, Magnesium, Zinc, and Calcium.

We have demonstrated the feasibility of generating coherent tunable light using only a two-level atomic system. This process should be applicable to most atomic and possibly molecular systems as well as scalable to longer gain lengths for higher energies. This could be a tremendous tool for achieving laser wavelengths in the XUV/X-ray range without the need for traditional population inversion as well as a potential source for atmospheric remote sensing. Even in other wavelength regimes where techniques such as parametric oscillators/amplifiers offer suitable options, fast Rabi-induced sidebands could act as a supplementary technology as it essentially does not have a damage threshold unlike most nonlinear crystals. This would allow for generation higher energies per pulse and could significantly lower the cost of such technologies.

A home-built seeded Optical Parametric Amplifier (OPA) was created to provide the 10μJ tunable pump laser. A pulsed 10 ps laser at 1064 nm (18 kHz repetition rate) was frequency doubled in a Lithium Triborate (LBO) crystal to a 100 μJ 6

ps laser at 532 nm. The 532 nm laser pulse was then used to pump a pair of LBO crystals in a seeded OPA configuration with a Littman-Metcalf extended cavity diode laser (ECDL) with a tuning range from 763 to 798 nm (Sacher Lasertechnik Lion Series) acting as the seed. The resulting OPA output was then focused into the Rb cell using a 7.5 cm plano-convex lens. Given that the pump beam has a 2 mm beam width, the 7.5 cm lens focuses it to $\sim$50μm spot inside the cell.

Special care had to be taken in regard to the seeded OPA system. The OPA operates through noncritical phase matching, as such its wavelength selection is tuned via the temperature of the crystal. When unseeded, the parametric emission is extremely broadband and therefore the overlap of the seed with the pump field must be precise to suppress this amplified spontaneous emission(ASE). Furthermore, when the seed laser is tuned across its full wavelength range from 760 to 797 nm, the temperature of the LBO crystal must also be simultaneously adjusted to reduce the ASE wings that would begin to emerge if the center of the spectral gain of the LBO does not match the wavelength of the seed. Lastly, even with proper matching of temperature and alignment, the laser cannot simply be considered just a picosecond tunable source. Some of the CW seed still propagates through the entire experiment to the Rb cell, thus at all times the Rb will be pumped with a few milliwatts of power along with the intense picosecond pulses. This can be avoided with a long path length from the crystals to the Rb cell as there will be a slight walk-off between the picosecond pulses and the CW seed.

Prior to the focusing lens, a CaF_2 window is placed into the beam path at 45° relative to the beam path to pick off the backward emission from the Rb vapor where it couples to a fiber input for a spectrometer (Andor Shamrock 303i with Newton camera). Furthermore, a power meter was positioned to collect the reflection off of the glass slide from the input pump pulse in order to monitor the pump energy.

A second fiber input for the spectrometer is located after the cell to collect the forward emission. The experimental scheme is sketched in Fig. 2.2. While the pump wavelength was scanned simply by tuning the wavelength of the ECDL, precise control of the pump energy was achieved with the aid of a half waveplate and a glan polarizer. Furthermore, the Rubidium vapor density was varied by way of changing the cell's temperature.

For the time resolved spectral measurements, we employed a time-correlated single photon counting module (bh, SPC-150) and Photomultiplier tube (PMT) as the detector on the output of a monochromator (Spectral Products, CM-110). A 750 nm long pass filter was placed in front of the PMT to prevent any stray 532 nm light in the OPA from corrupting our measurements. In general, this sideband emission was a time intensive measurement. For the most accurate time domain results, the voltage on the PMT must be established such that it is measuring single photons for every laser pulse as the only accurate measure of the timing can be on the first observed photon. This required multiple pulses to build up good statistics for a single measurement at a given pump wavelength and monochromator wavelength. For a full scan as seen Fig.2.7c, this required approximately 20 hours even with the process being fully automated. Furthermore, the voltage of the PMT needed to be adjusted midscan as it would rise above the single photon counting statistics when the monochromator wavelength was near pump wavelength or near the sideband emission when compared to the observed emission from fluorescence. Even with all of these adjustments accounted for, the accuracy of this tool was still limited. Despite having a mechanical accuracy of approximately 10 pm for the monochromator, there was was still wavelength bleed-through for anything within .2 nm as we observed in our measurements of the pump pulse. Furthermore, the single photon counting module had a purported accuracy of approximately 100 ps, but when paired with

monochromator, the time domain measurements are likely unable to resolve any features below 200 ps as can be seen of its measurement of our 6 ps pump pulse in Fig.2.7c.

Using the above experimental parameters, the Rabi frequency can be estimated via $\Omega_d = \frac{\wp \cdot E}{\hbar}$. Here E is the electric field amplitude and $\wp$ is the electric dipole moment which depends on the spontaneous decay rate, Γ, according to $\wp = \sqrt{3\pi\varepsilon_0\hbar c^3\Gamma/\omega^3}$, where ω is the transition frequency [93]. The average electric field can be estimated through $I = n\varepsilon_0 c|E|^2/2$ where n is the index of refraction and I is the intensity of the pump laser. Given the similarity of the transition frequencies and strengths for the D_1 and the D_2, we can state roughly that Ω_d is on the order of 1 THz for both transitions at maximum pulse energy.

Furthermore, collective atomic frequency, Ω_A, can also be estimated using $\Omega_A = \sqrt{\frac{3cN\lambda^2\Gamma}{8\pi}}$. Thus, given a Rb vapor density of $N \sim 10^{17}\ cm^{-3}$, Ω_A is approximately $3 \times 10^{13}\ rad/s$. In comparison, the dominant loss channel, the collisional dephasing rate ($\gamma_{coll} = 2\pi N(0.515 \times 10^{-13})$) is $\gamma_{coll} \sim 3 \times 10^9\ rad/s$. Given that Ω_d and Ω_A are both greater than γ_{coll}, we can safely assert that our experiment is within the regime where coherence effects play a large role.

2.2 Numerical Simulations

While quantitative analysis is always a necessary step when evaluating a new process such as FRISBE, we first compared the observed emission to the toy model where our sidebands are simply defined as $\omega_d \pm \Omega_{Eff}$. While this won't provide a deeper understanding of the underlying mechanisms or parameters necessary for emission, it provides a nice road map to ensure we were on the right path. As seen in Fig. 2.10, there is good qualitative agreement between the observed forward emission. The major discrepancy between this toy model and the experiment occurs

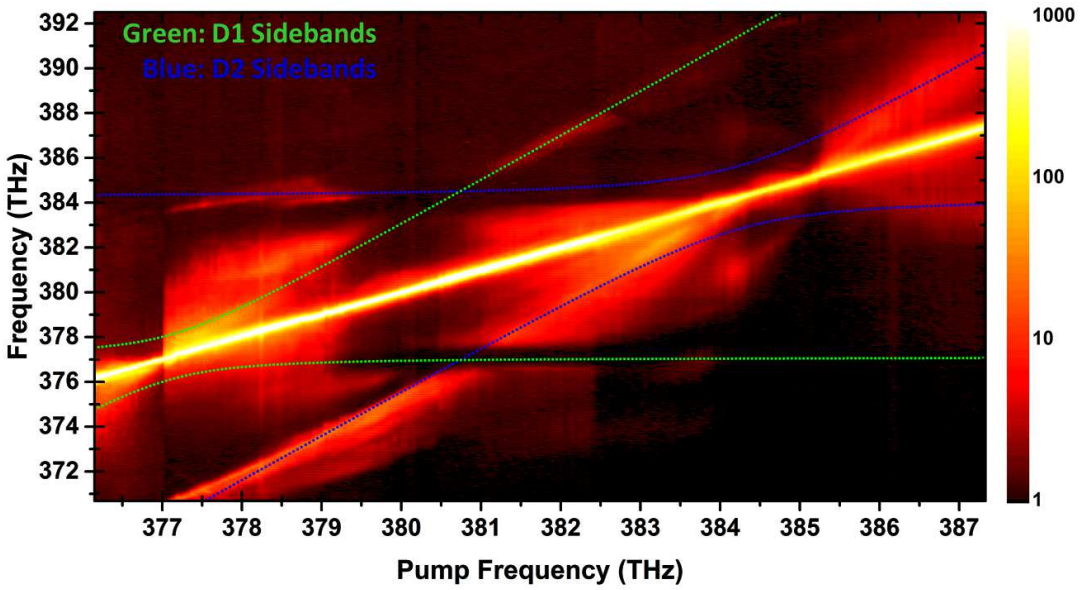

Figure 2.10: **Simple Model of the Sidebands Mapped onto Experimental Data** Overlap of the simple model where the sidebands are given by $\omega_d \pm \Omega_{Eff}$, with the observed forward emission as the wavelength is scanned. The green (blue) dashed lines correspond to the location of the predicted sidebands for the D_1 (D_2) transition. The Rabi frequency, Ω_d, was chosen to be 1 THz. While there is good qualitative agreement, it is insufficient for quantitative analysis.

near resonance. This is likely due to absorption of the pump beam before it reaches the gain region in the experiment. This effectively lowers the effective Rabi frequency in the focal volume to the point that it is potentially too low to drive the process. This also applies to the offresonant case where sidebands created from the D_2 transition will also lower slightly when the pump wavelength is close to the D_1 transition. This is depicted in Fig.2.10 where the dashed blue line diverges from the observed emission.

Furthermore, we need to be a bit careful not to depend too heavily upon this toy model as the sideband emission may not exactly appear at $\omega_d \pm \Omega_{Eff}$ even when the absorption of the pump field is accounted for. In contrast, Mollow gain, which may be considered the underlying spark for this emission process, does not exhibit gain

at the effective Rabi frequency. Instead, the highest gain for Mollow gain is always observed at detunings just under the effective Rabi frequency whereas the probe field is observed at the value of the effective Rabi detuning[72, 113]. In essence, Mollow gain does follow the effective Rabi frequency, but is simply offset from the exact value. Similarly, for the FRISBE process, which stems from Mollow gain, developing a more robust model is necessary, not only to better predict the frequency of emission, to better understand the other dependent parameters.

The analytical expressions used in the simulations are solutions of the density matrix equations for a two level atom of frequency ω_{ab} pumped by a strong laser of frequency ω_1 and Rabi frequency Ω_d also being driven by two probe fields symmetric to the pump at frequencies $\omega_3 = \omega_1 + \nu$ and $\omega_4 = \omega_1 - \nu$. This gives the susceptibility for each applied field, which is then used in an analytic theory of sideband generation through four-wave mixing in the dressed state. Thus the gain for an applied probe field is calculated as a function of the probe frequency as well as the properties of the system. In our case these are the parameters of the D_1 and D_2 levels of Rubidium as well as a pump field with an estimated an estimated Rabi of $\Omega_d \sim 1THz$. We use this to generate a plot of the spectral gain as a function of the pump frequency (Fig. 2.7c). It is important to emphasize that the simulation is not a plot of actual emission, but a gain/absorption map as the pump laser is scanned.

To further understand the behavior of the emission and to scrutinize our model, more simulations were performed using artificial values of both the atomic density and driving Rabi frequency (laser power). The study simulating the extremes of the laser field intensity are depicted in Figs. **??** & 2.12. Here, in Fig. 2.11a, at a Rabi frequency of approximately $10\times$ the experimental value, the sideband emission is much further detuned from the transitions even when the pump detuning is the same (compare to Fig. 2.2). This is due to the Rabi frequency Ω_d being a much more

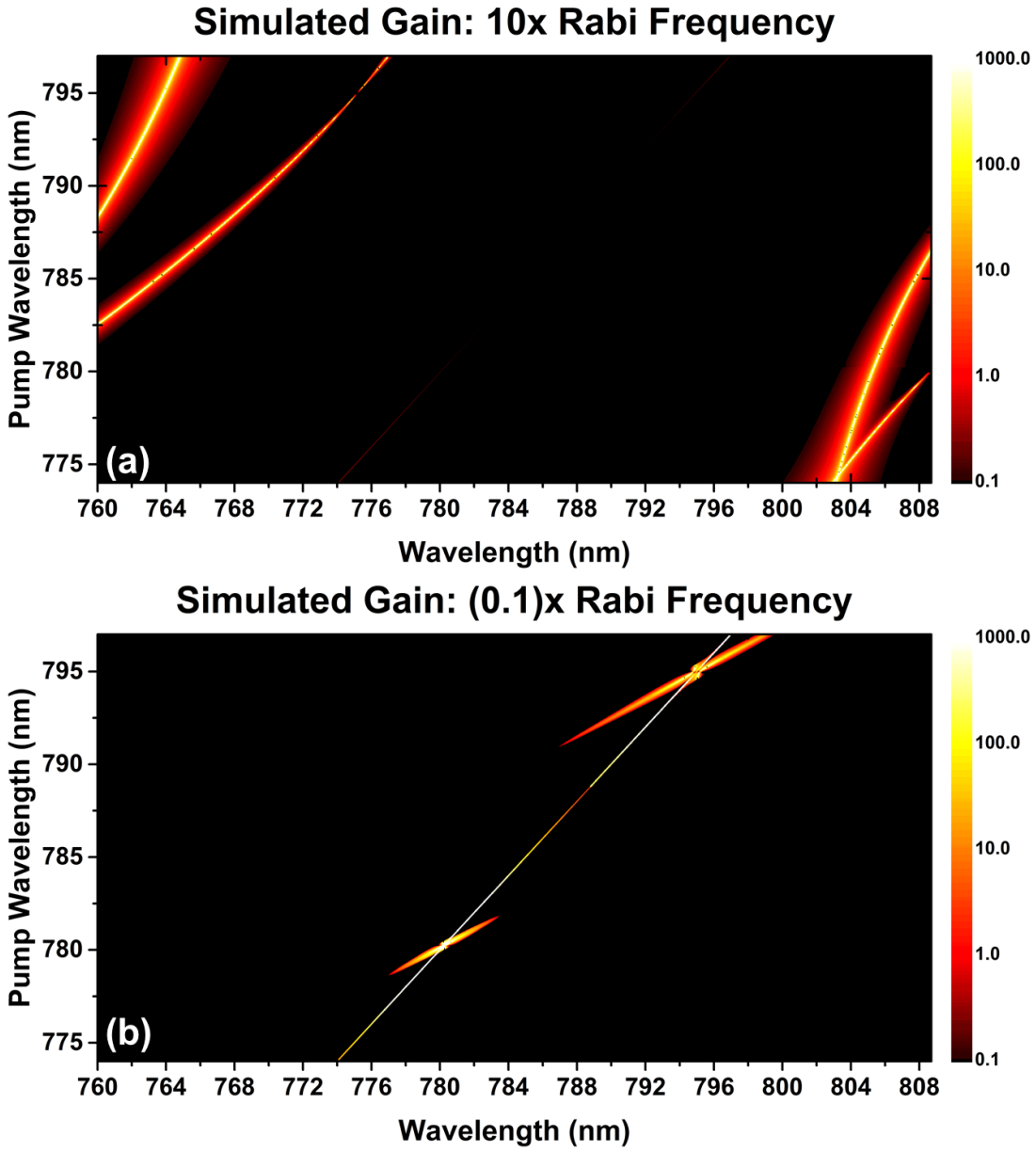

Figure 2.11: **Gain Simulations at High and Low Rabi Frequencies (a)** Simulated wavelength scan using a Rabi frequency 10× the estimated experimental value. The density was kept at the estimated experimental value of 2×10^{16} cm^{-3}. The brighter sidebands are due to the D_2 as has a stronger dipole moment than the D_1 transition. **(b)** Simulation at 0.1× the experimental Rabi frequency.

dominant term relative to the pump detuning, Δ. Not only does the gain appear to be much higher out at these further detunings, but the slight difference in the dipole strengths of the D_1 and D_2 transitions becomes more apparent where the D_2 sidebands exhibit higher gain. In contrast, the simulation at low Rabi frequency ($1/10\times$ the experimental value) depicts sidebands with small detunings relative to the pump wavelength. In this case,the detuning, Δ , is the dominant term in the effective Rabi. Also of note is that the gain drops off fairly quickly as the detuning is increased.

Both simulations for the low and high Rabi frequencies agree with our experimental and simulated pump energy scans presented earlier (Fig. 2.2c&2.2d). Furthermore, these simulations do seem to hint that the Rabi frequency should be within an order of magnitude of the detuning to achieve optimal gain at the sidebands. This can understood conceptually by considering the coupling of the system. Given that the pump laser has a detuning Δ from a transition ω_{ab}, optimal coupling between the drive field and transition will occur if the Rabi frequency matches that difference, $\omega_{ab} = \omega_{laser} + \Omega_d$, hence $\Omega_d \approx \Delta$.

The simulations for the low and high atomic densities also provided some insights into the behavior of the FRISBE process. The high and low densities were simulated at $10\times$ and $1/10\times$ the atomic density used in our experimental wavelength and power scans, so they correspond to approximately 2×10^{17} and 2×10^{15} cm^{-3}. In the high density simulation, Fig.2.12a, the frequency of the sideband emission for a given pump detuning remains unchanged from the scan using the experimental parameters, which is in keeping with theory as the atomic density should not effect the frequency of the emission. The higher density does cause some other changes to emission.

In particular, the overall gain is increased, which logically follows given that the drive field is now interacting with a larger population. Furthermore, the higher

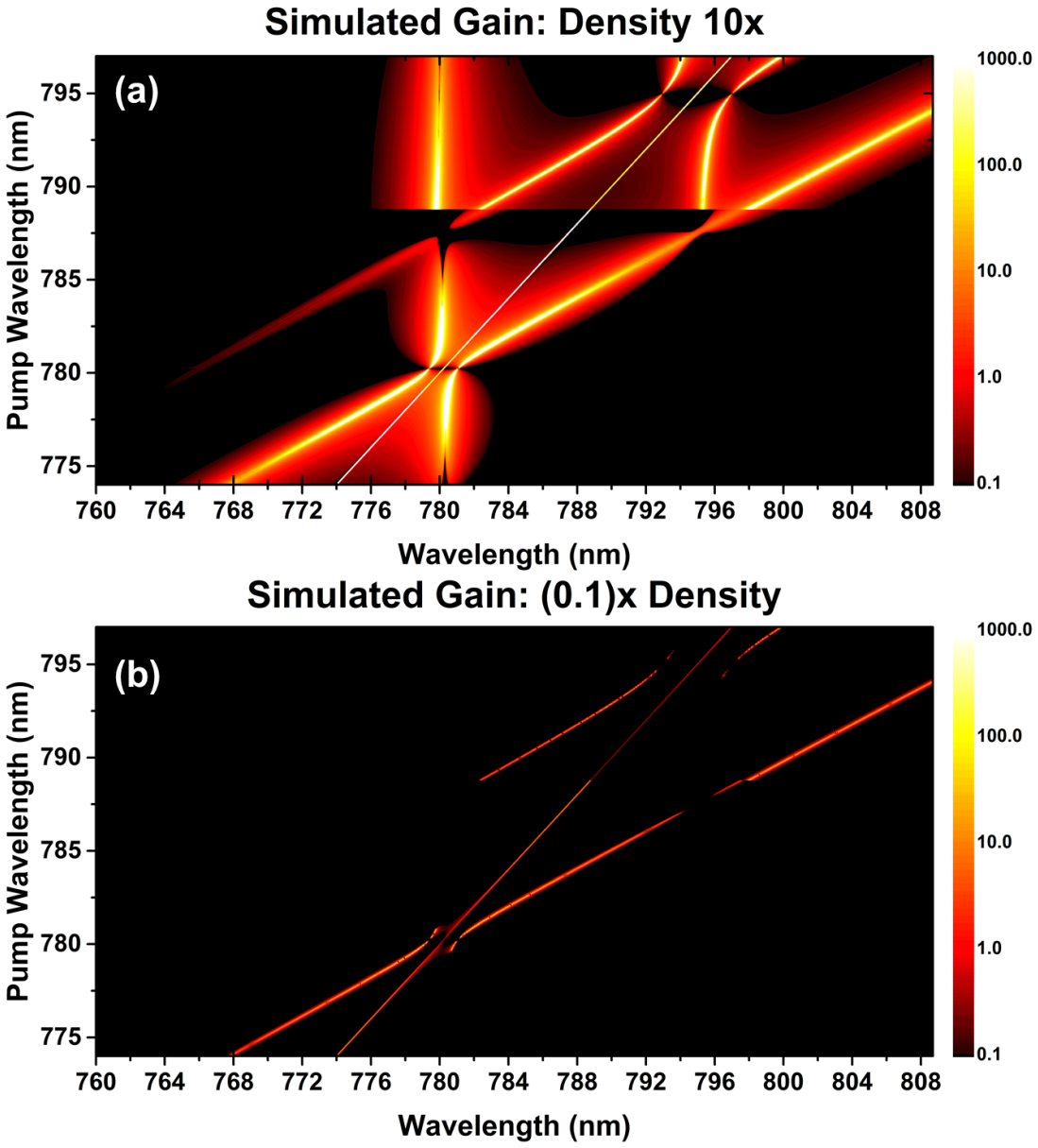

Figure 2.12: **Gain Simulations at High and Low Atomic Densities (a)** Simulated wavelength scan using an Atomic density 10× the estimated experimental value. The Rabi frequency was kept at the estimated experimental value of 2 THz. At high density, the linewidth of the sideband emission is broadened due to collisions and more gain occurs on the actual transitions due to the collisions dephasing the atomic ensemble. **(b)** Simulation at 0.1× the experimental Rabi frequency..

density also increases the collisional dephasing rate which broadens the linewidth of the sideband emission. This increased collisional dephasing rate, as its name implies, dephases a portion of population which essentially provides a larger population for the sideband that is degenerate with the atomic transition, hence the appearance of gain along the atomic transition that was not present at lower atomic densities. The low density simulation, Fig.2.12b, further confirms this behavior as the sideband gain is lower, the linewidth is narrower, and little to no gain occurs along the atomic transition.

Given our extensive use of simulations to verify and characterize the FRISBE emission, it is best to study the underlying model. For the full derivation of the equations used in these numerical simulations, we must consider a two-level atom and then apply 3-fields, in practice the theory is assuming two input fields. One strong field E_1 with frequency ω_1 which provides two photons, and a weak probe field with field E_3 with frequency ω_3, which then generates the 3rd field E_4 with frequency ω_4. We skipped ω_2, because its assumed that the strong field provides two photons, and the four-wave mixing theory initially assumes four fields.

The electric field in the media is taken to be:

$$\vec{E}(\vec{r},t) = \sum_i \hat{\epsilon} A_i e^{i\vec{k}_i\cdot\vec{r}} e^{-i\omega_i t} + \hat{\epsilon}^* A_i^* e^{-i\vec{k}_i\cdot\vec{r}} e^{i\omega_i t}. \tag{2.4}$$

These three frequencies are going to drive the two level atom, which has density matrix equations as:

$$\dot{\rho}_{eg} = -(i\omega_{eg}+\gamma)\rho_{eg} + i(\Omega_1 e^{-i\omega_1 t} + \Omega_3 e^{-i\omega_3 t} + \Omega_4 e^{-i\omega_4 t})(\rho_{ee}-\rho_{gg}) \tag{2.5}$$

$$\dot{\rho}_{ee} - \dot{\rho}_{gg} = -r(\rho_{ee}-\rho_{gg}-(\rho_{ee}-\rho_{gg})^0) + 2i(\Omega_1^* e^{i\omega_1 t} + \Omega_3^* e^{i\omega_3 t} + \Omega_4^* e^{i\omega_4 t})\rho_{eg}$$
$$- 2i(\Omega_1 e^{-i\omega_1 t} + \Omega_3 e^{-i\omega_3 t} + \Omega_4 e^{-i\omega_4 t})\rho_{ge} \tag{2.6}$$

where we assumed that the fields are all copropagating, so that everything has the same spatial dependence. Here $\gamma = 1/T_2$ is the decoherence rate for the transition and $r = 1/T_1$ is the population decay rate, and . We have also assumed that we are in the rotating wave approximation, which should be okay but as well see later we need to be careful because we sometimes for non-linear mixing the counter-rotating terms becomes important.

The plan for solving these equations, E_1 will be treated to all orders because its strong and E_3 and E_4 will be treated only to first order because they are weak. Then we can analyze the system using my normal assumption where we assume that there are only a fixed number of dominant frequencies in the system and solve for the slowly varying amplitudes of the fast oscillations. Here we assume that

$$\rho_{eg} = \rho_{eg}^{\omega_1} e^{-i\omega_1 t} + \rho_{eg}^{\omega_3} e^{-i\omega_3} + \rho_{eg}^{\omega_4} e^{-i\omega_4 t} \tag{2.7}$$

where we are assuming $\omega_4 = 2\omega_1 - \omega_3$. Now one approach is to solve for the steady state amplitudes of these coherences. This is a good approximation if the pulse is very long compared to the coherence time $\gamma \gg t_p$, but for our experimental parameters it is a terrible approximation. For a 6ps pulse there is no time to reach the steady state, it may be actually better to find the peak coherence value, which is not necessarily the same thing. But to get that value we will either have to make a ton more approximations that will not be valid for all regimes, or we would have to solve the coherences numerically.

The equations we get are:

$$\dot{\rho}_{eg}^{\omega_1} = -(i(\omega_{eg} - \omega_1) + \gamma)\rho_{eg}^{\omega_1} + i\Omega_1(\rho_{ee} - \rho_{gg}) \tag{2.8}$$

$$\dot{\rho}_{eg}^{\omega_3} = -(i(\omega_{eg} - \omega_3) + \gamma)\rho_{eg}^{\omega_3} + i\Omega_3(\rho_{ee} - \rho_{gg}) \tag{2.9}$$

$$\dot{\rho}_{eg}^{\omega_4} = -(i(\omega_{eg} - \omega_4) + \gamma)\rho_{eg}^{\omega_4} + i\Omega_4(\rho_{ee} - \rho_{gg}) \tag{2.10}$$

$$\frac{d}{dt}(\rho_{ee} - \rho_{gg}) = -r[\rho_{ee} - \rho_{gg} - (\rho_{ee} - \rho_{gg})^0] + 2i\Omega_1^*\rho_{eg}^{\omega_1} + 2i\Omega_3^*\rho_{eg}^{\omega_3} + 2i\Omega_4^*\rho_{eg}^{\omega_4} - 2i\Omega_1\rho_{ge}^{\omega_1} - 2i\Omega_3\rho_{ge}^{\omega_3} - 2i\Omega_4\rho_{ge}^{\omega_4} \tag{2.11}$$

Where we have dropped the population dynamics from the equations which are all very weak.

$$\rho_{eg}^{\omega_1} = \frac{\Omega_1(\rho_{ee} - \rho_{gg})^{dc}}{\omega_1 - \omega_{eg} + i\gamma}, \tag{2.12}$$

$$\rho_{eg}^{\omega_3} = \frac{\Omega_3(\rho_{ee} - \rho_{gg})^{dc}}{D(\omega_3)}\left[(\omega_3 - \omega_1 + ir)(\omega_3 - 2\omega_1 + \omega_{eg} + i\gamma) - \frac{2|\Omega_1|^2(\omega_3 - \omega_1)}{\omega_1 - \omega_{eg}}\right], \tag{2.13}$$

$$\rho_{eg}^{\omega_4} = \frac{2\Omega_1^2\Omega_3^*(\rho_{ee} - \rho_{gg})^{dc}(\omega_3 - \omega_1 + 2i\gamma)}{D(\omega_3)(\omega_1 - \omega_{ge} - i\gamma)}. \tag{2.14}$$

With the steady state population given as

$$(\rho_{ee} - \rho_{gg})^{dc} = \frac{(\gamma^2 + (\omega_1 - \omega_{eg})^2)(\rho_{ee} - \rho_{gg})^0}{\gamma^2 + (\omega_1 - \omega_{eg})^2 + 4(\gamma/r)|\Omega_1|^2} \tag{2.15}$$

and the denominator is given as

$$D(\omega_i) = (\omega_i - \omega_1 + ir)(\omega_i - \omega_{eg} + i\gamma)(\omega_i - 2\omega_{eg} + i\gamma) - 4|\Omega_1|^2(\omega_i - \omega_1 + i\gamma). \tag{2.16}$$

These equations can give spectral gain in some limits, but this nothing new. It is the same thing as Mollow gain which has been known for a while.

The linear and non-linear susceptibilities for these fields are:

$$\chi_{\omega_3}^{(1)} = -N\mu_{ge}\rho_{eg}^{\omega_3}/E_3 \tag{2.17}$$

$$\chi^{(1)}_{\omega_4} = -N\mu_{ge}\rho^{\omega_4}_{eg}/E_4 \tag{2.18}$$

$$\chi^{(3)}_{\omega_3} = -N\mu_{ge}\rho^{\omega_3}_{eg}/(E_1^2 E_4^*) \tag{2.19}$$

$$\chi^{(3)}_{\omega_4} = -N\mu_{ge}\rho^{\omega_4}_{eg}/(E_1^2 E_3^*) \tag{2.20}$$

Now if we want to consider propagation we have to solve the propagation equations for the fields. The Helmholtz equations for the two probe fields are

$$\nabla^2 E_3 + k_3^2 E_3 = \frac{4\pi\omega_3^2}{c^2}\left[iIm\chi^{(1)}_{\omega_3}E_3 + \chi^{(3)}_{\omega_3}E_1^2E_4^*\right], \tag{2.21}$$

$$\nabla^2 E_4 + k_4^2 E_4 = \frac{4\pi\omega_4^2}{c^2}\left[iIm\chi^{(1)}_{\omega_4}E_4 + \chi^{(3)}_{\omega_4}E_1^2E_3^*\right]. \tag{2.22}$$

Where $k_i = n_i\omega_i/c$ and $n_i = n_0 + 2\pi Re\chi^{(1)}_{\omega_i}$. If we make some significant approximations we can linearize these equations by assuming for $i = 3, 4$ that

$$\left|\frac{\partial^2 A_i}{\partial z^2}\right| \ll k_i \left|\frac{\partial A_i}{\partial z}\right|. \tag{2.23}$$

The key to this approximation is that the amplitudes need to remain weak, so this is helpful for determining the thin media gain, but will not work for large optical depths (which is unfortunately our case). In that case we can write the linearized equations

$$\frac{\partial A_3}{\partial z} = -\alpha_3 A_3 + \kappa_3 A_4^* e^{i\Delta kz} \tag{2.24}$$

$$\frac{\partial A_4^*}{\partial z} = -\alpha_4 A_4^* + \kappa_4^* A_3 e^{-i\Delta kz} \tag{2.25}$$

where the vector mismatch is given by

$$\Delta k = 2k_1 - k_3 - k_4, \tag{2.26}$$

and the coefficients are

$$\alpha_3 = -2\pi\frac{\omega_3}{n_3 c} Im\chi^{(1)}_{\omega_3}, \tag{2.27}$$

$$\alpha_4 = -2\pi\frac{\omega_4}{n_4 c} Im\chi^{(1)}_{\omega_4}, \tag{2.28}$$

$$\kappa_3 = -2\pi i\frac{\omega_3}{n_3 c}\chi^{(3)}_{\omega_3} A_1^2, \tag{2.29}$$

$$\kappa_4 = -2\pi i\frac{\omega_4}{n_4 c}\chi^{(3)}_{\omega_4} A_1^2. \tag{2.30}$$

Eq.(2.24) and Eq.(2.25) can be solved with the initial conditions at the boundary $z = 0$

$$A_3(0) = A_3^0, \tag{2.31}$$

$$A_4^*(0) = A_4^0. \tag{2.32}$$

The solution is

$$\begin{aligned} A_3(z) = (g_+ - g_-)^{-1}\{&[\kappa_3 A_4^0 - (g_- + \alpha_3 + i\Delta k/2)A_3^0]e^{g_+ z} \\ &- [\kappa_3 A_4^0 - (g_+ + \alpha_3 + i\Delta k/2)A_3^0]e^{g_- z}\}e^{i\Delta k z/2}, \end{aligned} \tag{2.33}$$

$$\begin{aligned} A_4^*(z) = (g_+ - g_-)^{-1}\{&[\kappa_4^* A_3^0 - (g_- + \alpha_4 - i\Delta k/2)A_4^0]e^{g_+ z} \\ &- [\kappa_4^* A_3^0 - (g_+ + \alpha_4 - i\Delta k/2)A_4^0]e^{g_- z}\}e^{i\Delta k z/2}. \end{aligned} \tag{2.34}$$

Here the gain coefficients are

$$g_\pm = \pm\frac{1}{2}\sqrt{(\alpha_3 - \alpha_4 + i\Delta k)^2 + 4\kappa_3\kappa_4^*} - \frac{1}{2}(\alpha_3 + \alpha_4). \tag{2.35}$$

This solution can be seen to be correct, by plugging it back in, or you can set $\Delta k = 0$, and have Mathematica solve them.

To generate plots we scan over the pump field frequencies ω_1 and the probe field ω_3, while assuming that $\omega_4 = 2\omega_1 - \omega_3$. Then we can calculate $A_3(L) + A_4^*(L)/(A_3^0 + A_4^0)$ where L is 2mm.

3. COHERENCE BRIGHTENED LASER SOURCE FOR ATMOSPHERIC REMOTE SENSING*

The need for an improved approach and efficient tools for remote optical sensing is apparent as they would facilitate applications ranging from environmental diagnostics and probing to chemical surveillance and biohazard detection. Present-day techniques rely on collecting incoherently scattered laser light and are often hindered by small signal collection efficiency [99, 10, 85, 80]. New emerging coherent techniques such as Raman [55, 118] and Terahertz [56] spectroscopies are promising. Availability of a laser-like light source emitting radiation in a controlled directional fashion, from a point in the sky back toward a detector, should revolutionize remote sensing [37, 48]. Dogariu et al. demonstrated the possibility of remote lasing of atmospheric oxygen by using sub-mJ picosecond UV laser pulses at 226 nm that produce a bright near-infrared (NIR) laser source at 845 nm wavelength using atomic oxygen as the gain medium [21].

It has been proposed that a mirrorless laser can be used as a superradiant source where coherence is large, such as a coherence brightened laser [20, **?**, 96]. This type of superradiance was first demonstrated in optically pumped HF gas [97]. Sweeping the gain, where multiple gain regions are used to stimulate eachother, can enhance the superradiant emission [48]. Gain-swept superradiance in air may be used to realize various nonlinear optical remote sensing schemes such as coherent Raman Umklapp-scattering [118], two-photon absorption [42], stimulated Raman scattering [94, 61], polarization Kerr effect (RIKES) spectroscopy [35], and others. Nonadiabatic coher-

*Part of this chapter is reprinted with permission from "Coherence brightened laser source for atmospheric remote sensing" by Traverso, A.J., et al. (2012). *Proceedings of the National Academic of Science*, 109, 1518515190. & Yuan, L. et al. (2013) "Theoretical analysis of the coherence-brightened laser in air." *Phys. Rev. A* 87, 023826.

ence is a fundamental characteristic in coherence brightened emission processes like superradiance and superfluorescence, and occurs when the macroscopic polarization of the medium changes more quickly than the decoherence rates. In the present paper, we study the temporal features of this NIR laser source from atomic oxygen and analyze the role of atomic coherence.

Stimulated emission (SE) in atomic oxygen - the key physical effect behind laser-like beam generation from UV-pumped atmospheric air - was first observed by Aldén et al. [4]. They used 3 mJ, 5 ns, 226 nm laser pulses to simultaneously photodissociate molecular oxygen and excite the atomic oxygen product along the $2p^3P \rightarrow 3p^3P$ transition causing a population inversion and allowing for stimulated emission via the $3p^3P \rightarrow 3s^3S$ transition at 845 nm [4]. This discovery initiated an in-depth examination of SE as a tool for flame and flow diagnostics in the early 1990s; including the analysis of laser-power and gas-pressure dependence of the SE signal [111], as well as the kinetics of the relevant populations [39].

Nearly two decades after the work on SE performed in the context of flame and flow diagnostics, a renewed interest in laser-like emission from open air is motivated by the need for chemically selective stand-off detection of trace gases in the atmosphere [37]. Laser-like emission provides a promising tool for a broad class of all-optical stand-off detection methods, as it suggests a physical mechanism whereby a high-brightness, highly directional back-propagating light beam can be generated directly in ambient air. As proposed by earlier work on SE via femtosecond filamentation [59], the generation of backward-directed lasing in air, using the most dominant constituents such as nitrogen or oxygen, is very promising for remote atmospheric spectroscopy.

Time-resolved studies of SE pulse shapes on a picosecond time scale revealed an exponential decay of the SE signal in the wake of a picosecond UV pump pulse [3].

In experiments with nanosecond pump pulses, the SE waveform was found to exhibit a spiky structure, which was attributed to a similar structure of the pump [3]. Our own investigations also show a SE waveform with a spiky structure, but these spikes cannot be explained by the mechanisms previously proposed and may have a more profound physical significance. We demonstrate below that the spiky structure of SE pulses in our experiment may point toward nonadiabatic atomic coherence within the light emission process due to a large Rabi frequency and the very short time duration of the individual intensity spikes.

3.1 Experiment

In this work, we investigate the forward and backward directed emission of oxygen when pumped by nanosecond UV laser pulses. The experimental scheme is sketched in Fig. 1. The laser system consists of 532 nm output from an injection-seeded Spectra Physics PRO-290-10 Nd:YAG laser which pumps a Sirah Cobra Stretch pulsed dye laser producing 622 nm output when a mixture of Rhodamine 610 and Rhodamine 640 in methanol is used. This 622 nm output is mixed with the residual 355 nm from the Nd:YAG laser in a Sirah SFM-355 frequency mixing unit to produce $\sim 10\ ns$ pulses of 226 nm light with ∼10 mJ/pulse at 10 Hz [88]. The resulting beam is focused using a convex lens (1 m focal length). The gain region, consisting of oxygen atoms produced by the focused pump, is ~ 1 cm long and has a waist of $\sim 17\ \mu$m. Emission in both the forward and backward direction is then detected and characterized. Particularly, a 300 nJ signal is detected in the backward direction, which is an order of magnitude higher than in the previous experiment using picosecond pump pulses [21].

To determine the dimensions of the gain region, we first calculate the radius at the beam waist and the focal depth of the 226 nm beam assuming a beam radius of

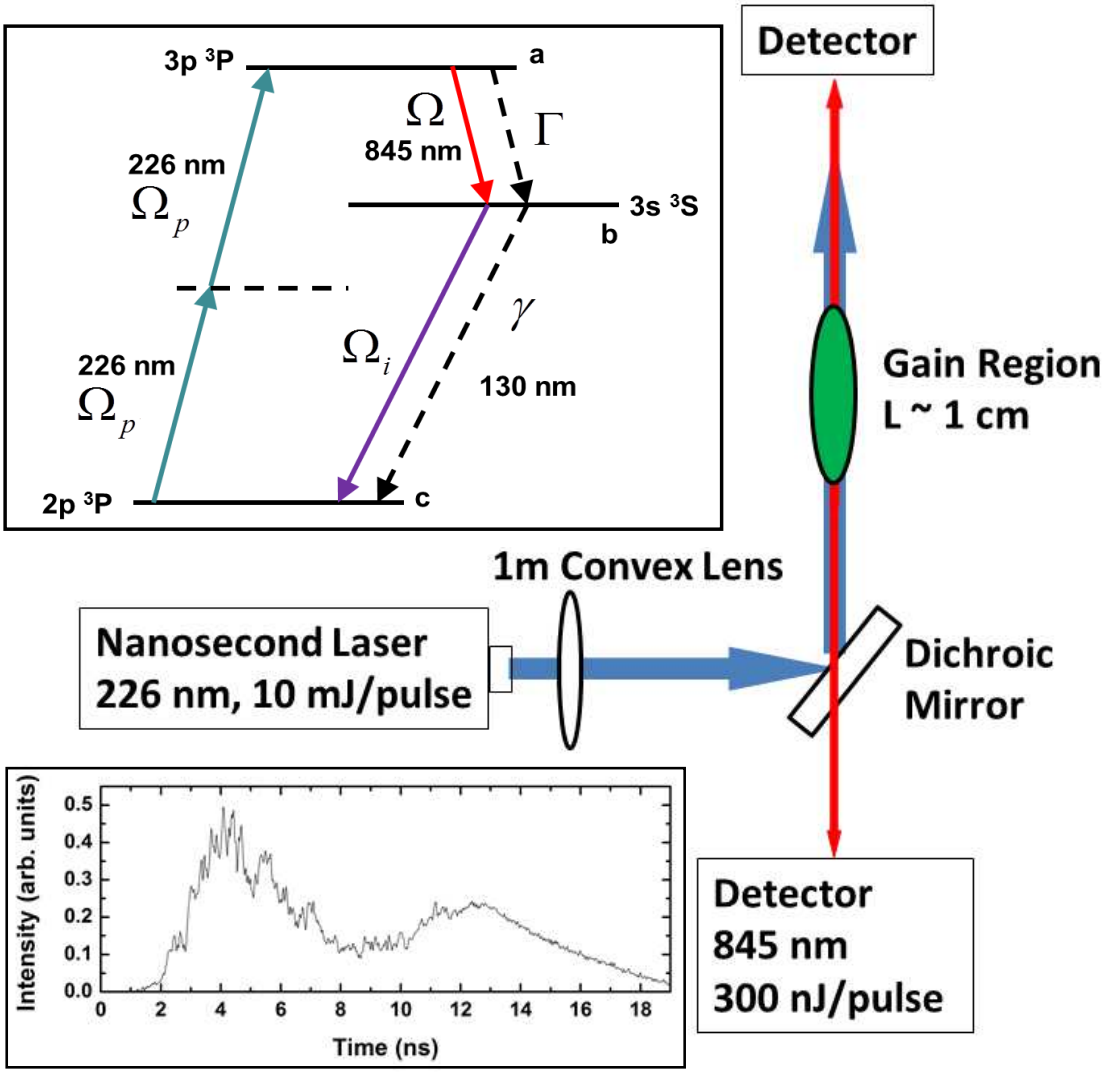

Figure 3.1: **Simplified Experimental Scheme** Nanosecond 226 nm laser pulses were focused with a 1 m lens dissociating the oxygen molecules at the focal point in ambient air. The 226 nm pulse further excited the newly dissociated oxygen atoms via two-photon absorption causing a population inversion. The backward detection was performed through a dichroic mirror. [**Bottom Inset**] An example of the pump pulse's intensity profile. [**Top Inset**] The energy level scheme is depicted for oxygen atoms undergoing two-photon excitation and stimulated emission at 845 nm. $\Gamma = 9.3 \times 10^6 s^{-1}$ and $\gamma = 0.197 \times 10^9 s^{-1}$ are the decay rates from $3p\ ^3P$ to $3s\ ^3S$ and from $3s\ ^3S$ to $2p\ ^3P$ states, respectively.[106]

0.25 cm incident on the 1 m focusing lens and a Gaussian beam profile. This was accomplished by solving

$$r(z) = r_0\sqrt{1 + \left(\frac{z\lambda}{\pi {r_0}^2}\right)^2} \tag{3.1}$$

for r_0, the radius at the beam waist, where $r(z)$ is the beam radius a distance z away from the focal point. This gives a radius of $r_0 = 28.8\ \mu m$. Likewise, the focal depth, b, can be calculated via

$$b = \frac{2\pi {r_0}^2}{\lambda} \tag{3.2}$$

This gives a length of $b = 2.3$ cm. If this was a single photon process it would scale with the intensity, I, but we must account for the fact that this is a four photon process (two photons to dissociate an oxygen molecule and two more to excite atomic oxygen to the $3p\ ^3P$ state). Therefore, the rate of excitation is proportional to I^4, and using the definition for the intensity

$$I(x,z) = I_0\left(\tfrac{r_0}{r(z)}\right)^2 e^{\frac{-2x^2}{r(z)}} \tag{3.3}$$

where x is the radial distance, we can solve for the dimensions at FWHM of the gain region. This gives the values of $r_0 = 17\ \mu m$ and $b = 1.03$ cm. For simplicity in the simulations, we took the focal depth $b \sim 1$ cm and the cros-section of the gain region to be $A = 10^{-5}\ cm^2$.

The power of both signals was measured versus the pump power using a pyro-electric power meter from Ophir (Fig. 3.2b). A characteristic threshold behavior is observed for both forward and backward 845 nm beams indicating a laser-like process instead of simple fluorescence. Also, there was a distinct energy difference between

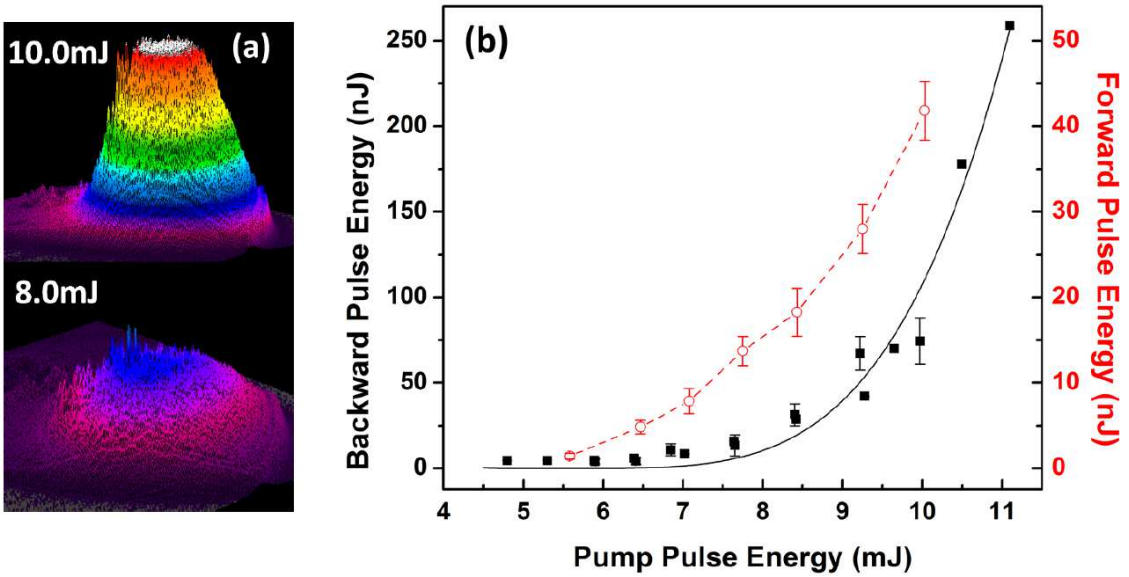

Figure 3.2: **Threshold Characteristics[106] (a)** Spatial beam profiles of the 845 nm emitted backward pulse at pump energies above (10.0 mJ), and at (8.0 mJ) threshold. **(b)** The energy per pulse of both the forward (red circles), and backward (black squares) signals versus the pump power;

the forward and backward emission, which is discussed below.

Furthermore, using the measured pulse energy, the average Rabi frequency can be experimentally estimated via $\Omega = \frac{\wp E}{\hbar}$, where E is the electric field amplitude and $\wp$ is the electric dipole moment which depends on the spontaneous decay rate, Γ, according to $\wp = \sqrt{3\pi\varepsilon_0\hbar c^3\Gamma/\omega^3}$, where ω is the transition frequency [93]. Given that $\Gamma = 9.3 \times 10^6 s^{-1}$ for the $3p\ ^3P$ to $3s\ ^3S$ transition, $\wp = 1.41 \times 10^{-29} C \cdot m$. Similarly, the measured pulse energy (Fig. 3.2b) along with the diameter of the gain region and the pulse duration ($t \sim 10\ ns$, discussed in next section), provide the average intensity $I = 6.11 \times 10^{10}\ W/m^2$, which is then used to calculate the electric field amplitude via $I = n\varepsilon_0 c|E|^2/2$, where n is the index of refraction. This finally leads to an experimental estimate of the average Rabi frequency for the 845 nm transition $\Omega = 1.3 \times 10^{12}\ rad/s$, whose high value provides further evidence of

nonadiabatic atomic coherence when compared with the collisional dephasing rate ($\gamma_{col} \sim 1 \times 10^{10} s^{-1}$) [23]. In this case the average Rabi frequency is much higher than the dephasing rate, and when a system is in this regime, then atomic coherence effects will occur [5].

Further evidence of a laser-like process was discovered by analyzing the spatial beam profiles of the backward pulse when the pump power was varied from approximately 6 to 10 mJ. These measurements were made using a Spiricon beam profiler (SP620U). A distinct threshold was observed at $\sim$ 8 mJ with a Gaussian profile. The width of the beam profile right at the threshold (8 mJ) was significantly wider than the profiles for any of the pump powers above threshold. Fig. 3.2a depicts this. Furthermore, from 6 to 8 mJ, emission was observed by eye, but the profile was too broad and weak for detection. Also, above threshold, all of the beam profiles had approximately the same width. Both of these features are indicative of a laser-like source.

The temporal pulses shapes were measured using a Tektronix MSO72004C fast oscilloscope (20 GHz bandwidth, 50 GigaSamples/sec, and ~ 20 *ps* resolution) and a New Focus high speed photodiode (model: 1437; 25 GHz bandwidth and 14 ps risetime). As can be seen in Fig. 3.3, the temporal profiles varied from shot to shot mainly due to the rapid intensity fluctuations in the individual 226 nm pump pulses (an example is shown in the bottom inset of Fig. 1). Due to instrumental artifacts centered around 20 GHz, near the oscilloscope's bandwidth limit, all frequency components above 15 GHz were removed. Single-shot temporal profiles of forward and backward pulses were measured simultaneously using the same photodiode (New Focus, described above) and are presented in Figs. 3.3a and 3.3b, respectively. The main feature of the temporal profiles is the high frequency oscillation, which is similar to spiking that was previously observed and believed to be caused by intensity

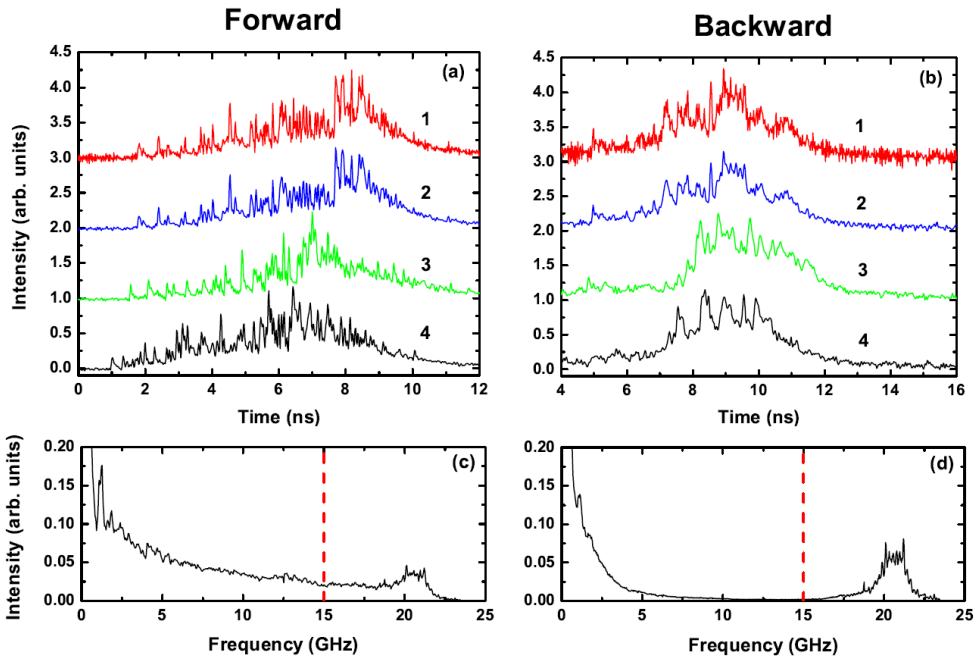

Figure 3.3: **Temporal Dynamics of Emission**[106] Single shot temporal profiles of both forward **(a)** and backward **(b)** pulses at full pump energy (10 mJ). The top pulses, **1**, in both are shown without any frequency filtering while the pulses immediately below, **2**, are the same pulses after Fourier filtering. Pulses **3** and **4** are other examples of filtered pulses, vertically shifted for convenience. Averaged Fourier transforms of the forward **(c)** and backward **(d)** pulses. The Fourier transforms depict and help quantify spectral intensity modulations for both pulses. Filtering was applied by subtracting the Fourier spectrum of the background as well as removing all frequency components beyond the red dashed line as they were artifacts of the electronics.

fluctuations in the pump pulse [3]. In contrast to this previous experiment, our observed spiky structure is higher in both frequency and amplitude. Besides the rapid oscillations, several other features can be discerned from the data. Namely, the forward signal exhibits a higher rate of oscillation with more high frequency components (broadband, $5 - 15$ GHz), as can be seen in the Fourier transforms in Figs. 3.3c and 3.3d. Furthermore, from shot to shot, there are significant variations in the amplitude and number of oscillations.

In Fig. 3.4, we compare the typical narrowest spikes in the emitted pulses with a measured response of a femtosecond test pulse (Ti:Sapphire, 35 fs, 800 nm) which is well below the resolution limit. As can be seen in Fig. 3.4a, the forward spiking is most likely narrower than can be resolved by our detection system. In contrast, the narrowest peaks observed in the backward direction are $\sim 60\ ps$ (FWHM) in duration (Fig. 3.4b). These measurements along with the Fourier transforms depicted in Figs. 3.3c & 3.3d, emphasize the distinction between the forward and backward emission, as well as differentiate these results from previous experiments where no difference between forward and backward spike duration was observed [3]. Also, given how narrow these spikes are, it is clear that the peak Rabi frequency is higher than the average measured Rabi frequency, which extends this experiment further into the regime of strong nonadiabatic atomic coherence [5].

3.2 Theoretical Modeling

On average, the width of the short spiking/ringing is less than 0.1 ns and 0.3 ns for the forward and backward pulses, respectively. These values can be compared to the estimated decay time for the system, which suggests the approximate time scale of intensity oscillations if atomic coherence is present. The characteristic delay, T_D, radiation damping time, T_R, as well as the cooperation number, N_c, of the collective

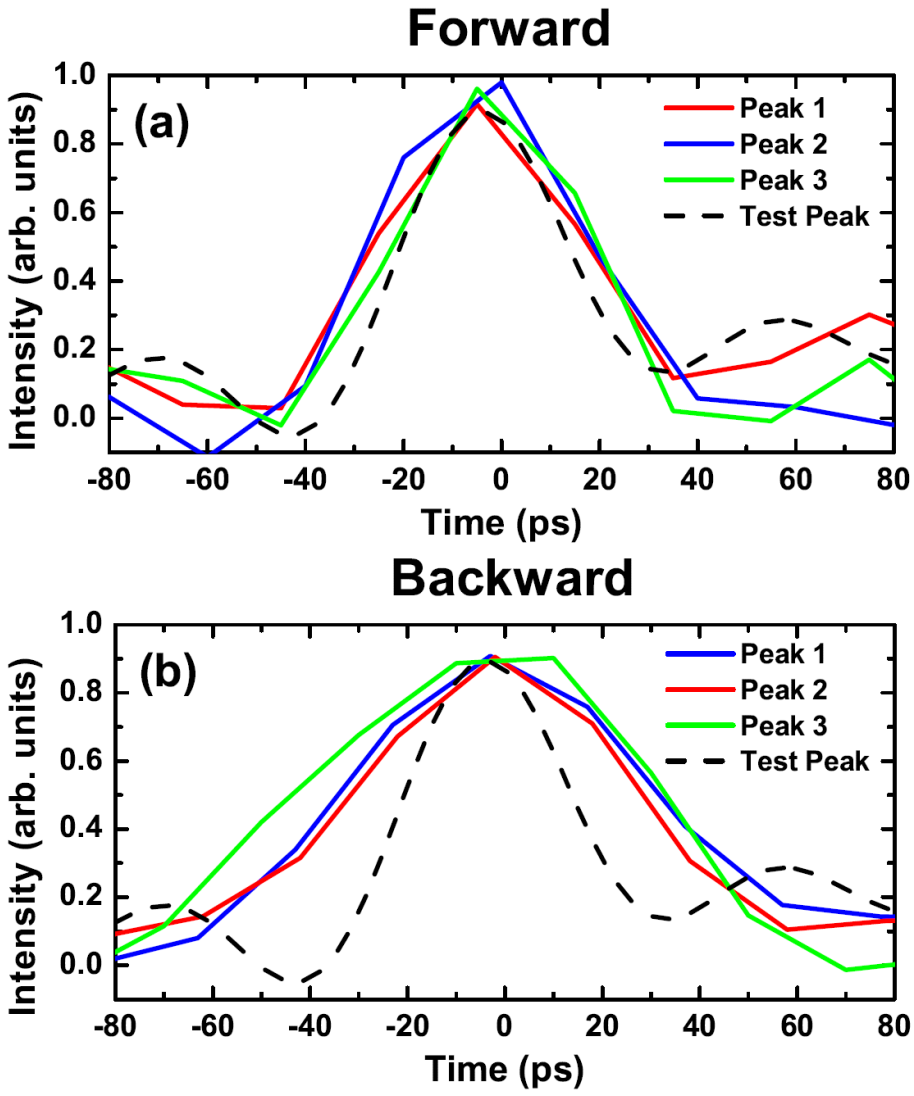

Figure 3.4: **Zoom-in of Spiky Emission Features**[**106**] Typical individual spikes for both the forward (**a**) and backward (**b**) pulses. In both figures, the dashed trace, Test Peak, is the response function of a 35 fs pulse at 800 nm used to test the resolution limit of the detection system. All traces are normalized for ease of comparison.

system are given by [60, 78]

$$T_R = T_{sp}(8\pi/N\lambda^2 L) \tag{3.4}$$

$$T_D = \frac{T_R}{4}\left[\ln\left(\sqrt{2\pi NAL}\right)\right]^2 \tag{3.5}$$

$$N_c = \frac{8\pi c T_1 A}{3\lambda^2 L} = N\frac{\tau_r c}{L}. \tag{3.6}$$

where $T_{sp} \sim 100\ ns$ is the spontaneous emission decay time for the lasing transition, $N \sim 10^{15}$ cm^{-3} is the density of the excited oxygen atoms in the gain region, $\lambda =$ 845 nm is the wavelength of the emitted field, $A \sim 10^{-5}$ cm^2 is the cross-section of the gain region and $L = 1$ cm is the gain length. Given these parameters, T_R is $\sim 0.4\ ps$, which is much less than any other characteristic time scale that enters the problem (such as decoherence or dephasing time). $T_D \sim 15\ ps$ describes the amount of time needed to develop the initial atomic coherence, but does not necessarily describe the time between the spikes. Furthermore, the single pass gain can be estimated using the above parameters as well as an experimentally estimated collisional dephasing rate, $\gamma_{col} \sim 10^{10} s^{-1}$ [23, 64]. This gives a value of $\alpha L \sim 476$ where αL is the single pass gain, which places this experiment in the strong oscillatory superfluorescence regime (α is the gain coefficient, L is the length of the gain region) [64].

In general, various regimes of N-atom cooperative spontaneous emission can defined by the values of the characteristic parameters provided above [**?**]. The physical meaning of each regime is discussed in detail in Ref. [64]. We summarize it briefly here. In the limit that $T_2 \to \infty$, there is no collisional dephasing, so SF is radiated for the duration τ_r with a delay time of τ_D. In the regime that $T_2 > \tau_D$, the coherence

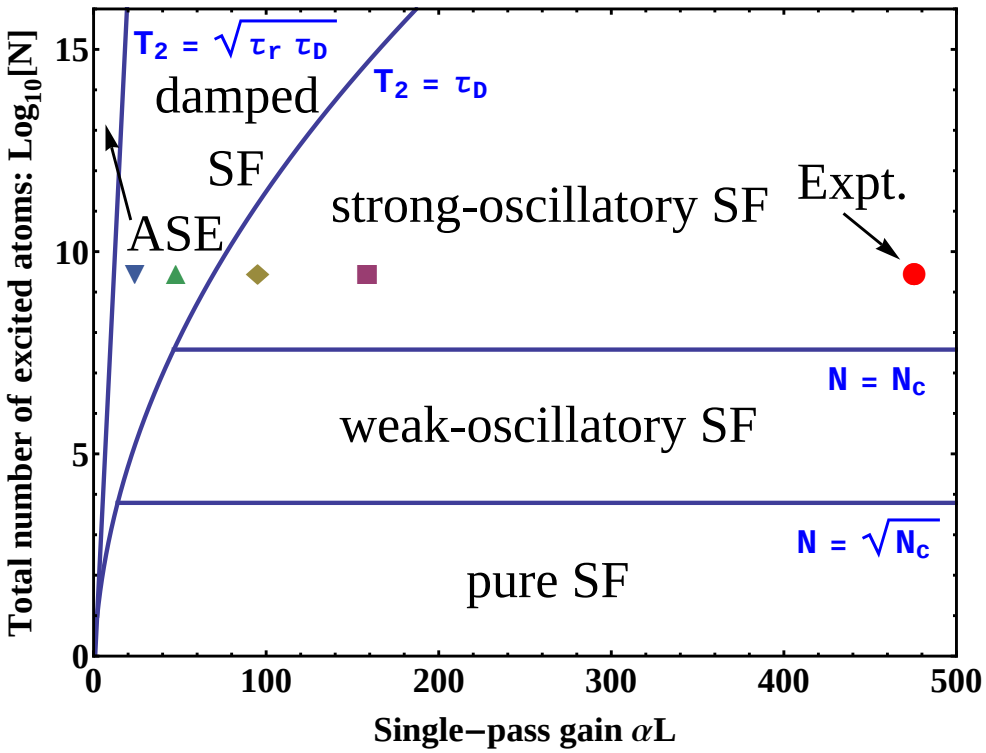

Figure 3.5: **Pictoral Diagram of Superfluorescence Regimes**[117] Regimes of N-atom cooperative spontaneous emission (adapted from Ref. [64]). Our experimental parameters correspond to the strong-oscillatory SF regime (red circle). The four other points (purple square, yellow diamond, green triangle, and blue inverted triangle) correspond to four distinct sets of parameters used in simulations (see below).

can be built up during the time τ_D before it decays by collisions and the cooperative emission process may occur. However, in the opposite regime where $T_2 < \sqrt{\tau_r \tau_D}$, the large collisonal dephasing rate prevents coherence from building up. Thus the system generates ASE (amplified spontaneous emission). In the intermediate regime (damped SF), both coherence and collisions play a role. The cooperation number N_c gives the maximum number of atoms that can emit cooperatively. When the total number of excited atoms, N, is larger than N_c, the propagation effect is present, and atoms undergo reabsorption and reemission processes. The SF emission has

temporal ringing behavior. But when $N < \sqrt{N_c}$, the propagation effect is negligable and pure SF is emitted. Figure 3.5 shows these various regimes determined by these parameters labelled ASE, damped SF, and SF (including strong-oscillatory SF, weak-oscillatory SF and pure SF) [?]. With the parameters from the recent experiment [106] as $T_2 \sim 0.1$ ns, $T_1 = 0.108$ μs, $\lambda = 845$ nm, $L \sim 1$ cm, $A \sim 10^{-5}$ cm^2, and $n \sim 3 \times 10^{14}$ cm^{-3}, we obtain $\tau_r \approx 0.4$ ps, $\tau_D \approx 15$ ps, $\alpha L \approx 476$ and $N_c \approx 4 \times 10^7$. While these values provide insight, a theoretical model is needed to provide a better understanding. This model and subsequent simulations are described below.

For our model, we use a pencil-like active medium, with a length of 1 cm and a cross-sectional area of 10^{-5} cm^2, as in the experiment. We assume the atomic density in this active medium is constant at 10^{15} cm^{-3} (with population initially in the ground state). The two-photon excitation of the $a \leftrightarrow c$ transition by the pump pulse is treated as two excitation processes via two allowed transitions with the smallest detuning between the pump field and the transition from the ground level to an intermediate level. This intermediate level corresponds to the 3s ^{3}S state (level b) in the atomic oxygen energy scheme. The detuning Δ is 6.1×10^{15} rad/s. The Rabi frequencies for the pump pulse coupled to the $a \leftrightarrow b$ and $b \leftrightarrow c$ transitions are $\Omega_{p1} = \wp_{ab}\mathcal{E}_p/\hbar$ and $\Omega_{p2} = \wp_{bc}\mathcal{E}_p/\hbar$, respectively, where $\wp_{ab}$, $\wp_{bc}$ are the matrix elements of the electric dipole moment and $\mathcal{E}_p$ is the slowly varying envelope amplitude with $E_p = \mathcal{E}_p e^{-i(\nu_p t - k_p z)} + c.c.$ Here E_p is the electric field, ν_p is the frequency and k_p is the wave-vector of the pump, and z is taken to be positive for the forward propagation direction. The detailed derivation of the two-photon excitation is shown below. The generated fields from the $a \leftrightarrow b$ and $b \leftrightarrow c$ transitions have both forward and backward contributions, which lead to the Rabi frequencies of $\Omega^+_{ab} e^{-i(\nu_{ab} t - k_{ab} z)} + \Omega^-_{ab} e^{-i(\nu_{ab} t + k_{ab} z)}$ and $\Omega^+_{bc} e^{-i(\nu_{bc} t - k_{bc} z)} + \Omega^-_{bc} e^{-i(\nu_{bc} t + k_{bc} z)}$, respectively. Here "+" and "−" represent forward and backward propagation, respectively. Ω^+_{ab},

Ω_{ab}^{-}, Ω_{bc}^{+}, and Ω_{bc}^{-} are assumed to be slowly varying functions. These fields are coupled with the active atomic medium. The semiclassical Maxwell-Bloch (MB) equations are used to describe the physics of this 3-level system. The phase-matching conditions are considered. The rotating wave approximation (RWA) is used, so the terms coupling the fields and the polarization in the medium which are not phase-matched are neglected.

In order to model the problem, we write the semiclassical Hamiltonian of the atomic oxygen system in the interaction picture as

$$\begin{aligned} H = &-\hbar\Omega_p e^{-i\Delta t} |a\rangle \langle b| - \hbar\Omega_p e^{i\Delta t} |b\rangle \langle c| \\ &-\hbar\Omega |a\rangle \langle b| - \hbar\Omega_i |b\rangle \langle c| + H.c., \end{aligned} \tag{3.7}$$

where a, b, and c represent the levels $3p\ ^3P$, $3s\ ^3S$, and $2p\ ^3P$, respectively, in the oxygen atom in Fig. 1; whereas Ω_p, Ω, and Ω_i are the Rabi-frequencies of the 226 nm 2-photon pump pulse, the 845 nm signal, and the 130 nm field between the middle $3s\ ^3S$ state and the ground $2p\ ^3P$ state, respectively; Δ is the detuning from the $3s\ ^3S$ state for the two photon excitation from the $2p\ ^3P$ to the $3p\ ^3P$ state. With this Hamiltonian, we can derive the density matrix equations, which, in conjunction with the field propagation equations, are used to describe the evolution of the population, electric fields, and the atomic coherence. The density matrix approach is necessary because nonadiabatic coherence cannot be described by laser rate equations due to the macroscopic polarization evolving faster than all the decoherence rates in the system [5, 109].

Here, we discuss the derivation of the two-photon excitation in detail and list the full set of density matrix equations. Using the slowly varying approximation and RWA and the assumption that the pump Rabi frequencies $\Omega_{p1}(t,z)$ and $\Omega_{p2}(t,z)$

are positive real functions. The coherences for the forward (+) and backward (-) propagating fields were treated as independent matrix elements. The Hamiltonian in the interaction picture reads

$$H_I = -\hbar\Omega_{p1}e^{-i\Delta t+ik_pz}|a\rangle\langle b| - \hbar\Omega_{p2}e^{i\Delta t+ik_pz}|b\rangle\langle c|$$

$$-\hbar(\Omega^+_{ab}e^{ik_{ab}z} + \Omega^-_{ab}e^{-ik_{ab}z})|a\rangle\langle b| - \hbar(\Omega^+_{bc}e^{ik_{bc}z} + \Omega^-_{bc}e^{-ik_{bc}z})|b\rangle\langle c| + H.c., \tag{3.8}$$

The density matrix equations for the coherence are

$$\dot{\rho}_{ab} = -\Gamma_{ab}\rho_{ab} - i(\Omega^+_{ab}e^{ik_{ab}z} + \Omega^-_{ab}e^{-ik_{ab}z})(\rho_{aa} - \rho_{bb}) - i\Omega_{p1}e^{-i\Delta t+ik_pz}(\rho_{aa} - \rho_{bb})$$

$$-i(\Omega^{+*}_{bc}e^{-ik_{bc}z} + \Omega^{-*}_{bc}e^{ik_{bc}z})\rho_{ac} - i\Omega^*_{p2}e^{-i\Delta t-ik_pz}\rho_{ac}, \tag{3.9}$$

$$\dot{\rho}_{bc} = -\Gamma_{bc}\rho_{bc} - i(\Omega^+_{bc}e^{ik_{bc}z} + \Omega^-_{bc}e^{-ik_{bc}z})(\rho_{bb} - \rho_{cc}) - i\Omega_{p2}e^{i\Delta t+ik_pz}(\rho_{bb} - \rho_{cc})$$

$$+i(\Omega^{+*}_{ab}e^{-ik_{ab}z} + \Omega^{-*}_{ab}e^{ik_{ab}z})\rho_{ac} + i\Omega^*_{p1}e^{i\Delta t-ik_pz}\rho_{ac}, \tag{3.10}$$

$$\dot{\rho}_{ac} = -\Gamma_{ac}\rho_{ac} + i(\Omega^+_{ab}e^{ik_{ab}z} + \Omega^-_{ab}e^{-ik_{ab}z})\rho_{bc} + i\Omega_{p1}e^{-i\Delta t+ik_pz}\rho_{bc}$$

$$-i(\Omega^+_{bc}e^{ik_{bc}z} + \Omega^-_{bc}e^{-ik_{bc}z})\rho_{ab} - i\Omega_{p2}e^{i\Delta t+ik_pz}\rho_{ab}, \tag{3.11}$$

where the dephasing rates are $\Gamma_{ab} = \frac{1}{2}(\gamma_{ab} + \gamma_{bc}) + \gamma_{col}$, $\Gamma_{bc} = \frac{1}{2}\gamma_{bc} + \gamma_{col}$, and $\Gamma_{ac} = \frac{1}{2}\gamma_{ab} + \gamma_{col}$, with γ_{col} being the collisional dephasing rate, and γ_{ab} and γ_{bc} are spontaneous decay rates at the $a \leftrightarrow b$ and $b \leftrightarrow c$ transitions, respectively. Expressing the coherence as a sum of the slow and fast varying terms (the latter oscillating at a frequency as the detuning Δ)

$$\rho_{ab} = \sigma_{ab} + u_{ab}e^{-i\Delta t}, \tag{3.12}$$

$$\rho_{bc} = \sigma_{bc} + u_{bc}e^{i\Delta t}, \tag{3.13}$$

plugging those two definitions into Eqs. (3.9)-(3.11) and using RWA to neglect the fast oscillating terms we obtain

$$\dot{\sigma}_{ab} = -\Gamma_{ab}\sigma_{ab} - i(\Omega_{ab}^{+}e^{ik_{ab}z} + \Omega_{ab}^{-}e^{-ik_{ab}z})(\rho_{aa} - \rho_{bb}) - i(\Omega_{bc}^{+*}e^{-ik_{bc}z} + \Omega_{bc}^{-*}e^{ik_{bc}z})\rho_{ac}, \tag{3.14}$$

$$\dot{u}_{ab} = -(\Gamma_{ab} - i\Delta)u_{ab} - i\Omega_{p1}e^{ik_{p}z}(\rho_{aa} - \rho_{bb}) - i\Omega_{p2}^{*}e^{-ik_{p}z}\rho_{ac}, \tag{3.15}$$

$$\dot{\sigma}_{bc} = -\Gamma_{bc}\sigma_{bc} - i(\Omega_{bc}^{+}e^{ik_{bc}z} + \Omega_{bc}^{-}e^{-ik_{bc}z})(\rho_{bb} - \rho_{cc}) + i(\Omega_{ab}^{+*}e^{-ik_{ab}z} + \Omega_{ab}^{-*}e^{ik_{ab}z})\rho_{ac}, \tag{3.16}$$

$$\dot{u}_{bc} = -(\Gamma_{bc} + i\Delta)u_{bc} - i\Omega_{p2}e^{ik_{p}z}(\rho_{bb} - \rho_{cc}) + i\Omega_{p1}^{*}e^{-ik_{p}z}\rho_{ac}, \tag{3.17}$$

$$\begin{aligned}\dot{\rho}_{ac} = &-\Gamma_{ac}\rho_{ac} + i(\Omega_{ab}^{+}e^{ik_{ab}z} + \Omega_{ab}^{-}e^{-ik_{ab}z})\sigma_{bc} + i\Omega_{p1}e^{ik_{p}z}u_{bc} \\ &-i(\Omega_{bc}^{+}e^{ik_{bc}z} + \Omega_{bc}^{-}e^{-ik_{bc}z})\sigma_{ab} - i\Omega_{p2}e^{ik_{p}z}u_{ab}.\end{aligned} \tag{3.18}$$

Because the detuning Δ in Eqs. (3.15) & (3.17) is much larger than any relaxation process, we assume that the terms u_{ab} and u_{bc} reach steady state quickly. Therefore, we write them as

$$u_{bc} = \frac{-\Omega_{p2}e^{ik_{p}z}(\rho_{bb} - \rho_{cc}) + \Omega_{p1}^{*}e^{-ik_{p}z}\rho_{ac}}{\Delta - i\Gamma_{bc}}, \tag{3.19}$$

$$u_{ab} = \frac{\Omega_{p1}e^{ik_{p}z}(\rho_{aa} - \rho_{bb}) + \Omega_{p2}^{*}e^{-ik_{p}z}\rho_{ac}}{\Delta + i\Gamma_{ab}}. \tag{3.20}$$

Plugging these two solutions into Eq. (3.18) with the assumption that $\Delta \gg \Gamma_{ij}$, we find

$$\begin{aligned}\dot{\rho}_{ac} = &-\Gamma_{ac}\rho_{ac} + i\frac{|\Omega_{p1}|^2 - |\Omega_{p2}|^2}{\Delta}\rho_{ac} - i\frac{\Omega_{p1}\Omega_{p2}}{\Delta}e^{i2k_{p}z}(\rho_{aa} - \rho_{cc}) \\ &+(\Omega_{ab}^{+}e^{ik_{ab}z} + \Omega_{ab}^{-}e^{-ik_{ab}z})\sigma_{bc} - (\Omega_{bc}^{+}e^{ik_{bc}z} + \Omega_{bc}^{-}e^{-ik_{bc}z})\sigma_{ab}.\end{aligned} \tag{3.21}$$

Next, we express the coherence as slowly varying terms with position z

$$\sigma_{ab} = \rho_{ab}^{+} e^{ik_{ab}z} + \rho_{ab}^{-} e^{-ik_{ab}z}, \tag{3.22}$$

$$\sigma_{bc} = \rho_{bc}^{+} e^{ik_{bc}z} + \rho_{bc}^{-} e^{-ik_{bc}z}, \tag{3.23}$$

and

$$\rho_{ac} \rightarrow \rho_{ac} e^{i2k_p z}. \tag{3.24}$$

Keeping in mind that the phase-matching condition gives $2k_p - k_{ab} - k_{bc} = 0$, we plug Eqs. (3.22)-(3.24) back into Eq. (3.14), Eq. (3.16), and Eq. (3.21) and use RWA to remove the terms with fast oscillation with z. (The treatment of the density matrix equations for the population is the same as for ρ_{ac}). Then we derive the full set of the density matrix equations, which is summarized in the following

$$\dot{\rho}_{ab}^{+} = -\Gamma_{ab}\rho_{ab}^{+} - i\Omega_{ab}^{+}(\rho_{aa} - \rho_{bb}) - i\Omega_{bc}^{+*}\rho_{ac}, \tag{3.25}$$

$$\dot{\rho}_{ab}^{-} = -\Gamma_{ab}\rho_{ab}^{-} - i\Omega_{ab}^{-}(\rho_{aa} - \rho_{bb}), \tag{3.26}$$

$$\dot{\rho}_{bc}^{+} = -\Gamma_{bc}\rho_{bc}^{+} - i\Omega_{bc}^{+}(\rho_{bb} - \rho_{cc}) + i\Omega_{ab}^{+*}\rho_{ac}, \tag{3.27}$$

$$\dot{\rho}_{bc}^{-} = -\Gamma_{bc}\rho_{bc}^{-} - i\Omega_{bc}^{-}(\rho_{bb} - \rho_{cc}), \tag{3.28}$$

$$\dot{\rho}_{ac} = -\left[\Gamma_{ac} - i\frac{|\Omega_{p1}|^2 - |\Omega_{p2}|^2}{\Delta}\right]\rho_{ac} - i\frac{\Omega_{p1}\Omega_{p2}}{\Delta}(\rho_{aa} - \rho_{cc}) + i\Omega_{ab}^{+}\rho_{bc}^{+} - i\Omega_{bc}^{+}\rho_{ab}^{+}, \tag{3.29}$$

$$\dot{\rho}_{aa} = -\gamma_{ab}\rho_{aa} + \left(i\Omega_{ab}^{+}\rho_{ba}^{+} + i\Omega_{ab}^{-}\rho_{ba}^{-} + i\frac{\Omega_{p1}\Omega_{p2}}{\Delta}\rho_{ca} + c.c.\right), \tag{3.30}$$

$$\dot{\rho}_{bb} = \gamma_{ab}\rho_{aa} - \gamma_{bc}\rho_{bb} + \left(-i\Omega_{ab}^{+}\rho_{ba}^{+} - i\Omega_{ab}^{-}\rho_{ba}^{-} + i\Omega_{bc}^{+}\rho_{cb}^{+} + i\Omega_{bc}^{-}\rho_{cb}^{-} + c.c.\right), \tag{3.31}$$

$$\rho_{aa} + \rho_{bb} + \rho_{cc} = 1, \tag{3.32}$$

We neglect Doppler broadening in the simulation because the collisional dephasing rate is the dominating relaxation process in the experiment. The Maxwell-Bloch equations read

$$\pm\frac{\partial\Omega_{ab}^{\pm}}{\partial z}+\frac{1}{c}\frac{\partial\Omega_{ab}^{\pm}}{\partial t}+\kappa\Omega_{ab}^{\pm}=i\eta_{ab}\rho_{ab}^{\pm}, \tag{3.33}$$

$$\pm\frac{\partial\Omega_{bc}^{\pm}}{\partial z}+\frac{1}{c}\frac{\partial\Omega_{bc}^{\pm}}{\partial t}=i\eta_{bc}\rho_{bc}^{\pm}, \tag{3.34}$$

where $\eta_{ij}=\frac{3}{8\pi}n_a\lambda_{ij}^2\gamma_{ij}$ is the field-atom coupling constant, where n_a is the atomic density and $\kappa=1.5\ cm^{-1}$ is the decay rate of the 845-nm field due to the Rayleigh diffraction limit. The simulation numerically solves this full set of equations using weak 845 nm fields at the boundaries to seed the forward and backward emission.

The dephasing of the atomic dipoles plays an important role, as it depletes the coherence but not the state populations; we take $\gamma_{col}=1\times10^{10}s^{-1}$ as above. It should be noted that the 130 nm UV field is coupled to the coherence between the excited state $3p\ ^3P$ and the intermediate state $3s\ ^3S$ for the forward 845 nm pulse, but not for the backward pulse. This is due to the fact that the 130 nm spontaneous emission gets absorbed by the surrounding atmosphere too quickly to start any such amplification, but the forward 845 nm field, Ω_{ab}^{+}, has phase $ik_{ab}z$ and the coherence, ρ_{ac}, has phase $2ik_{pump}z$. With these fields, a phase-matching condition is satisfied for 130 nm emission in the forward direction, $2k_{pump}=k_{ab}+k_{bc}$. This is similar to yoked superfluorescence [13, 119]. This coupling affects the coherence while the 130 nm field depletes the population in the intermediate state.

We first considered a shorter picosecond pump pulse to better understand the physics of the system and validate our simulations. We choose a 20 ps pump pulse with the same order of the peak power as in the experiment (~ 0.5 MW). Thus we can take the peak Rabi frequencies $\Omega_{p1}\sim3.2\times10^{13}$ rad/s and $\Omega_{p2}\sim8.4\times10^{12}$ rad/s and an effective Rabi frequency $\Omega_{eff}\equiv\Omega_{p1}\Omega_{p2}/\Delta\sim4.4\times10^{10}$ rad/s. Doppler

broadening is not included in this simulation because we assume that the collisional dephasing is the dominant relaxation process.

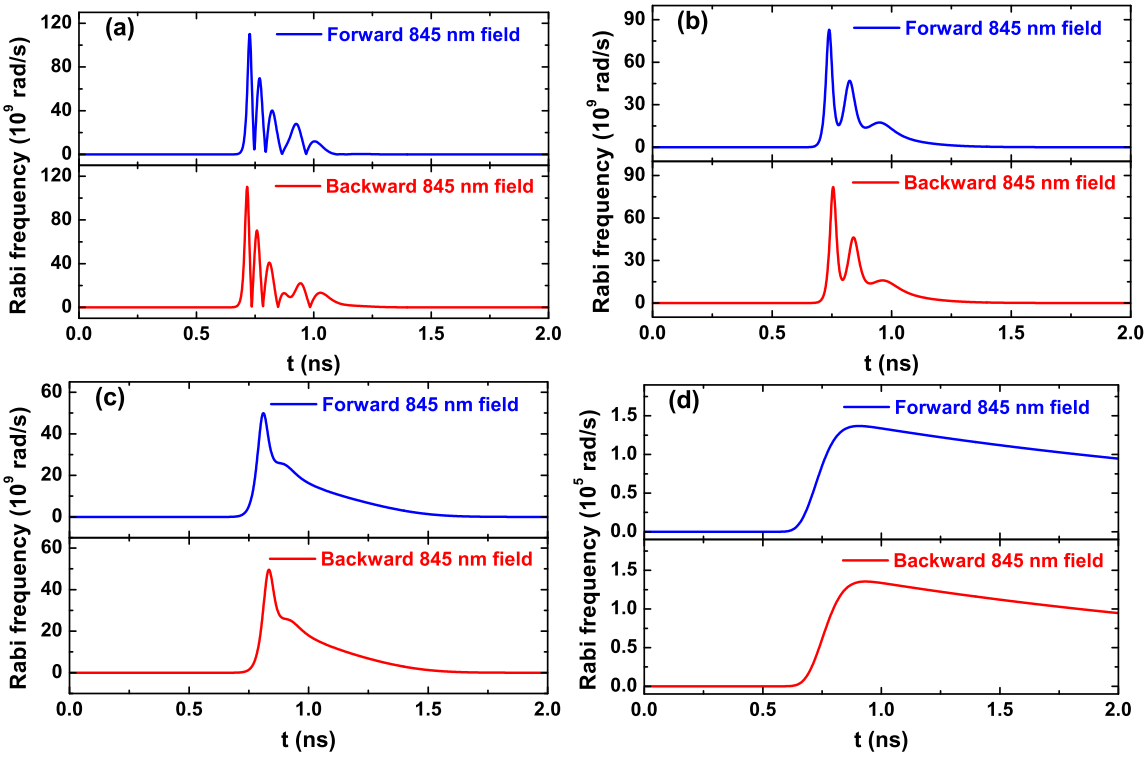

Figure 3.6: **Simulated Temporal Behavior**[117] Temporal behavior of the 845-nm forward and backward fields generated by a 20-ps 226-nm pump pulse with different collisional dephasing rates: (a) $\gamma_{col} = 10$ ns^{-1} (leading to the regime labelled by the red circle in Figure 3.5), (b) 30 ns^{-1} (labelled by purple square), (c) 50 ns^{-1} (labelled by yellow diamond), and (d) 100 ns^{-1} (labelled by green triangle).

The pump pulse enters the medium at time 0.5 ns. The emission fields at 845 nm are generated in both forward and backward directions. We fixed the boundary conditions for the 845-nm fields to be a small constant to play the role of a spontaneous emission source, but assume that there is no spontaneous emission source for the 130-nm field (the UV field is strongly absorbed in air). The decay rate for the

845-nm fields is $\kappa \sim 1.5$ cm^{-1} due to the Rayleigh diffraction length. The simulation results of the temporal behavior of the 845-nm fields ($|\Omega_{ab}^{\pm}|$) for different collisional dephasing rates (γ_{col}) are shown in Figure 3.6. Strong-oscillatory SF with large peak Rabi frequencies is seen in both the forward and backward directions when $\gamma_{col} = 10$ ns^{-1} (Figure 3.6a). The SF oscillations are damped and the intensity decreases for larger γ_{col}. The simulation results are consistent with the various regimes described in Figure 3.5. The physics is clear with this short picosecond pump pulse excitation. The upper transition of the oxygen atom is inverted after this pump pulse. In the small dephasing rate limit, the inverted system radiates SF and generates a large quantum coherence via cooperation between ensemble atoms. After the population is transferred from the upper level to the middle level, the coherence plays an important role by producing a weaker radiation, which in turn transfers a portion of population back to the upper level. The small portion of the population in the upper level then continues to radiate cooperatively. This process repeats and results in the ringing (*i.e.* Burnham-Chiao ringing [14]) in Figure 3.6a. In the large dephasing rate limit (see Figure 3.6c), the radiation generated by the inverted system produces a small amount of coherence because of the larger decoherece terms (Γ_{ab} and Γ_{bc}). The amount of coherence is not large enough to re-emit the field after the population moves to the middle level. However, there is a burst in the emission field because the process is still in the SF regime and the atoms radiate collectively. Nevertheless, with a significantly large dephasing rate (e.g. $\gamma_{col} = 100$ ns^{-1}) (Figure 3.6d), the inverted system cannot produce enough coherence so the radiation is closer to ASE than to SF. The difference between the forward and backward fields is not prominent in this regime. Phase-matching condition and the asymmetric scheme (*i.e.* forward and backward fields at the $a \leftrightarrow b$ and $b \leftrightarrow c$ transitions but only forward propagating pump pulse) are the main reasons for the difference, which is discussed in detail in

the next section. We find in this simulation with a simple short pump pulse that the atomic coherence is responsible for the spiky features.

Using this theoretical framework, a one-dimensional simulation was performed using parameters closely matching those of experiment and assuming a fixed population of atoms that is uniformly distributed throughout the gain region. A smooth pump pulse resembling those found in the experiment (Fig. 1) was used as the initial input for the simulations; i.e. it was fit to the averaged pump pulse to mimic the overall pulse shape, but lacked any rapid intensity oscillations. The results of the theoretical simulations are shown as curves **1** in Figs. 3.7a & 3.7b. Despite the absence of rapid intensity oscillations in the pump, the simulations reveal rapid intensity oscillations with spike widths on the same order as those found experimentally. Essentially, the generated field becomes so strong that the corresponding time scale for the evolution of the atomic system becomes faster than dephasing.

To substantiate that nonadiabatic atomic coherence phenomena are present, another simulation using the same theoretical model was constructed with an artificially large dephasing rate of $\gamma_{col} = 1 \times 10^{11}\ s^{-1}$ (curves **1** in Figs. 3.7c & 3.7d). The large dephasing depletes the coherence in the 845 nm infrared transition, but has no effect on the population. As such, the model predicts a simple pulse, akin to an ordinary laser pulse, with no high frequency modulations for both the forward and backward directions. Fig. 3.7 shows that the lack of coherence mitigates rapid oscillations which are characteristic of nonadiabatic coherence [**?**]. The pulses seen in curves **1** of Figs. 3.7c & 3.7d are due to laser spiking/relaxation oscillations [**?**]. In fact, under the condition of large collisional dephasing, the density matrix equations reduce to the laser rate equations. Hence the observation of high frequency oscillations in both the theoretical results in curve **1** of Figs. 3.7a & 3.7b and the experimental measurements in Fig. 3.3a & 3.3b show the coherent dynamics associated with the

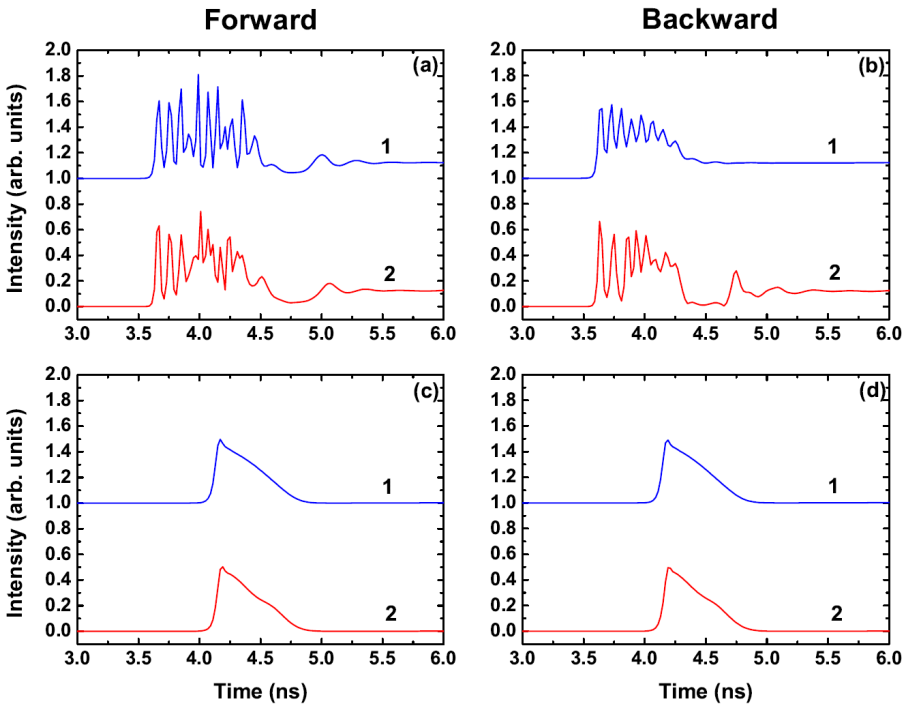

Figure 3.7: **Simulated Temporal Behavior using Experimental Parameters[106]** Simulated forward **(a)** and backward **(b)** signals with a dephasing rate of $\gamma_{col} = 1 \times 10^{10} s^{-1}$; forward **(c)** and backward **(d)** signals with artificially large collisional dephasing ($\gamma_{col} = 1 \times 10^{11} s^{-1}$). Curves **1** (blue) are obtained using a smooth pump pulse as the initial input, while **2** (red) used a pump pulse with random intensity fluctuations to mimic the experiment. The curves are vertically shifted for convenience.

reabsorption and reemission of the 845 nm light as the pulses propagate through the gain region. Experimentally, an order of magnitude increase in the collisional dephasing rate to $\gamma_{col} = 1 \times 10^{11}\ s^{-1}$ could be achieved by increasing the pressure of the gain medium. Further experiments with a gas cell under variable pressure could be used to explore this effect.

Further theoretical simulations were performed to verify the presence of nonadiabatic coherence. In particular, rapid intensity fluctuations were added to the pump pulse to resemble the experimental pump pulse shape. This was done to test whether

pump fluctuations could cause the observed rapid spiking seen in our emitted pulses as had been seen previously [3]. These simulations were again performed in both the small and artificially large collisional dephasing limits. For small collisional dephasing, rapid intensity spiking is still observed (curves **2** in Figs. 3.7a & 3.7b), but it is quite apparent that the pump fluctuations do effect the rapid oscillations found in the emitted pulses. However it does not rule out atomic coherence. Rapid intensity oscillations must also appear in the emitted pulses at large dephasing for pump pulse fluctuations to be the main explanation of the phenomenon. In this regime (curve **2** of Figs. 3.7c & 3.7d), all rapid oscillations disappear and the pulse shapes are similar to the large dephasing regime for the smooth pump pulse. This is consistent with attribution of the large amplitude rapid oscillations to a large atomic coherence.

In Fig. 3.8, simulation results are presented studying the effects of the collisional decay rate. In that study, the loss rate for the 845 nm field, ($\kappa = 1.5\ cm^{-1}$), remained constant. Here, we artificially increase the loss coefficient, $\kappa = 10\ cm^{-1}$, and examine its effects on the 845 nm output signals in the same two collisional regimes studied in the paper. All other parameters match those used to produce curve **1** in Fig. 3.8.

In Figs. 3.8a & 3.8b, the large loss coefficient has three major effects on the 845 nm emission when compared to the results in Figs. 5a & 5b of the paper: it decreases the overall power, increases the time delay of the emission, and produces a less spiky temporal profile. Nevertheless, the characteristic spiky features are still present in this regime. In the artificially large dephasing rate regime, Figs. 3.8c & 3.8d, the signals are also delayed and the overall power is decreased when compared to Figs. 5c & 5d. However, the spiky intensity features disappear. From this study, it is clear that while the loss coefficient changes the results quantitatively, a large loss coefficient can not produce the observed intensity spiking feature, which one might expect to see in the laser relaxation oscillations. Therefore, we conclude that

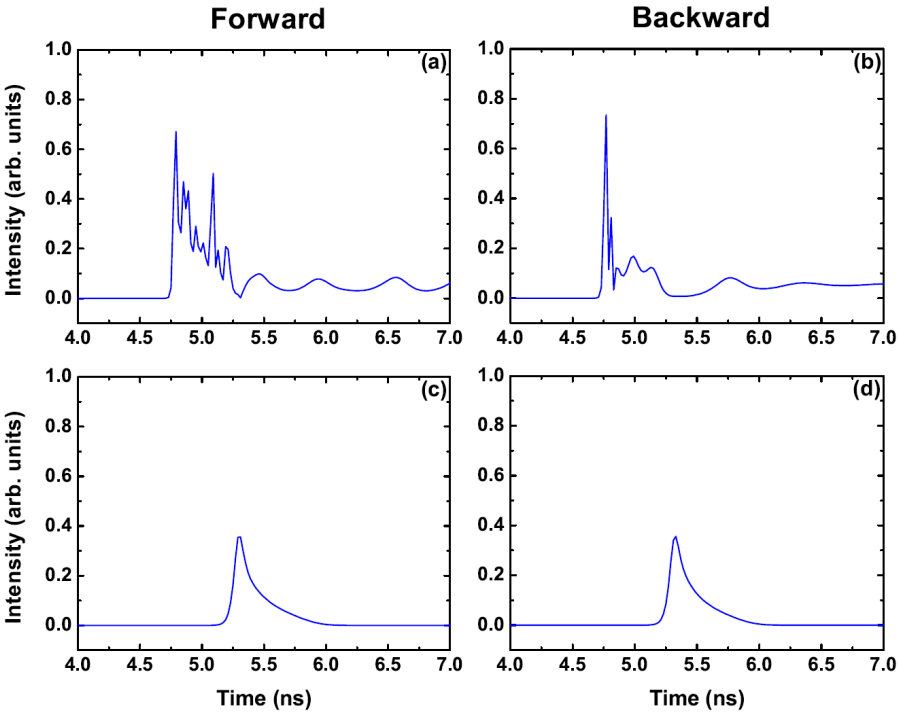

Figure 3.8: **Simulated Temporal Behavior with Large Dephasing[106]** Simulated forward **(a)** and backward **(b)** signals with a dephasing rate of $\gamma_{col} = 1 \times 10^{10} s^{-1}$; forward **(c)** and backward **(d)** signals with artificially large collisional dephasing ($\gamma_{col} = 1 \times 10^{11} s^{-1}$). Here, the loss coefficient for the signal is $\kappa = 10\ cm^{-1}$. A smooth pump pulse was used as the initial input.

the spiky temporal profile is due to the nonadiabatic coherence, which can only be described by the Maxwell-Bloch treatment.

3.3 Discussion

Again, the observed average Rabi frequency, $\Omega \sim 10^{12}\ rad/s$, is more than an order of magnitude larger than the estimated dephasing rate $\gamma_{col} = 1 \times 10^{10} s^{-1}$. Furthermore, the peak Rabi frequency is higher than the average as evidenced by the very short timescale of the intensity spiking (Fig. 3.4). These two results are strong evidence that places the emission process into the regime of nonadiabatic atomic coherence [5, 64].

The simulations performed above are intended to provide a qualitative insight into the physics of the emission process in ambient air. The model assumes the gain region to be one dimensional and populated uniformly by a fixed number of oxygen atoms, and because of these assumptions does not reproduce the exact experimental findings (for example the pulse duration and the pulse energy difference). These discrepancies are likely caused by asymmetries in the gain region, which may occur in the experiment due to the molecular oxygen dissociation process and the non-Gaussian beam profile of the pump pulse. However, even with the above simplifications, the simulations do explain qualitatively the coherent nature of the observed intensity spikes on the temporal pulses. From the simulations, it is clear that the spiking only occurs when atomic coherence is present. In the case of small atomic coherence, i.e. when collisional dephasing is large, these rapid spikes are suppressed.

These results provide another step towards the implementation of stand-off spectroscopy of gases in the atmosphere. The high beam quality, stability and power will allow detection of impurities in air with high sensitivity. In fact, this coherent emitted beam with a nanosecond pulse duration will be advantageous in nonlin-

ear optical processes. It should provide higher peak intensity which is crucial for techniques such as counter-propagating two-photon absorption, stimulated Raman scattering or Raman-induced Kerr effect spectroscopies. The 845 nm wavelength is in a suitable range of most common realizations of these techniques for detecting vibrational fingerprints of relevant molecules.

4. MID-IR ENHANCED COHERENT RAMAN

Third order nonlinear processes were first discovered in the late 1870s with the demonstration of the Kerr Effect[45, 46]. It wasn't until almost a century later with the advent of the laser that they were shown to generate optical fields through a variety of mechanisms. Namely, utilizing an intense coherent drive of a laser field led to the discovery of many new techniques including stimulated Raman scattering[24, 112, 36] (SRS), stimulated Brillouin scattering[17, 49] (SBS), Coherent anti-Stokes Raman[63, 54, 53] (CARS), degenerate four wave mixing[15] (DFWM), third harmonic generation in a isotropic media[73, 110, 103, 33], and third order parametric amplification[100]. Among these techniques, the development of better laser sources in the picosecond and femtosecond regime has facilitated a strong interest in CARS and SRS. These techniques are particularly attractive due their uses for molecular identification and selective excitation. In fact, they have been implemented in a diverse array of fields for such applications as biomedical imaging, plasma diagnostics, time-resolved chemistry, fiber lasers, remote sensing of bombs, and temperature measurements[121, 44, 115]. Through coherent generation, they offer unprecedented levels of control, directionality, and signals orders of magnitude greater than their spontaneous counterpart.

Despite these inherent advantages, there are some drawbacks with CARS and SRS. In particular, one major issue is the non-resonant background from DFWM that is ever-present in strongly driven SRS systems and CARS, especially when using a broadband pump[92]. Furthermore, given strong enough drives in SRS and CARS, competition between the Stokes and anti-Stokes signals can lead to signal suppression and limit the overall effective enhancement of using a coherent process.

Here, we demonstrate a unique four wave mixing approach that minimizes these issues by employing a mid infrared (IR) picosecond pump. The frequency of this field is chosen to be in 2-photon resonance with a given Raman transition. This IR field efficiently couples the ground and excited vibrational state moreso than the conventional far detuned pump and stokes fields of CARS. Furthermore, we observe an asymmetric enhancement in the anti-Stokes signal relative to the Stokes due to a third harmonic-like process.

Whenever an electric field, E, passes through a dielectric medium, it induces a polarization, P. If this electric field is of high enough intensity, i.e. a laser pulse, it induces higher order terms (nonlinear) such that the polarization can be expressed as Taylor series:

$$P(t) = \varepsilon_0 \chi^{(1)} E(t) + \varepsilon_0 \chi^{(2)} E^2(t) + \varepsilon_0 \chi^{(3)} E^3(t) + \ldots \tag{4.1}$$

Where $\chi^{(n)}$ is the $n-th$ order susceptibility. The linear susceptibility, $\chi^{(1)}$, is related to the index of refraction of the material, and thus correlates to the material's dispersion and absorption. Unlike $\chi^{(1)}$, the nonlinear susceptibilities, $\chi^{(2)}$ and $\chi^{(3)}$, depend on the intensity of the external field and can be utilized to generate new frequencies within the material. The second order susceptibility governs such processes as second harmonic generation (SHG), sum frequency generation (SFG) and differency frequency generation (DFG). Given a linear susceptibility to be $\chi^{(1)} \sim 1$ we would expect second order term of $P(t)$ to be comparable the linear component when the amplitude of the electric field E to be on the order of the characteristic atomic field strength,$E_{at} = e/a_0^2$, where e is the electron charge and a_0 is the Bohr radius. Therefore, $\chi^{(2)}$ is expected to be on the order of $\chi^{(1)}/E_{at} \sim 1.7 \times 10^{-10}$ m/V. By extension, the third order susceptibility, $\chi^{(3)}$, would be be comparable to

$\chi^{(1)}/E_{at}^2 \sim 2.8 \times 10^{-20}$ m/V. Furthermore, to fully describe these nonlinear effects, we must use an inhomogeneous form of the wave equation:

$$\nabla^2 E - \frac{n^2}{c^2}\frac{\partial^2}{\partial t^2}E = \frac{1}{\varepsilon_0 c^2}\frac{\partial^2}{\partial t^2}P^{NL} \tag{4.2}$$

where P^{NL} is the nonlinear component of the polarization, c is the speed of light, and n is the index of refraction due to the linear susceptibility $\chi^{(1)}$. Implicit to this equation is that electrons are being accelerated in the media due to the external electric field, E, which in turn generates new frequencies of light. These new frequencies can be determined by taking the Fourier transform the the time dependent solution of the nonlinear wave equation.

In regards to second order nonlinear effects, these processes only occur in media that possesses a non-centrosymmetric structure, i.e. an anisotropic material. This is because $\chi^{(2)} = 0$ in centrosymmetric and isotropic media, which includes most gases, liquids, and condensed matter. In contrast, $\chi^{(3)}$ does not have this limitation. It is possible to generate third order processes in most materials, though it generally has a higher intensity threshold for significant generation. In this study, we chose to focus on third order processes, given how much more adaptable and universally applicable these are mechanisms are for most materials.

Fig. 4.1 depicts many of the conventional third order nonlinear processes used today throughout science and engineering. The simplest third order nonlinear optically generating process is SRS shown schematically in Fig. 4.1a. This was first discovered in 1962 when a cell of nitrobenzene was placed in a Q-switched laser cavity[24, 112, 36, 115]. SRS is often used in the configuration where a strong pump field excites the medium and a weak probe (Stokes) field is frequency scanned searching for amplification of the probe. This configuration has been used to great effect

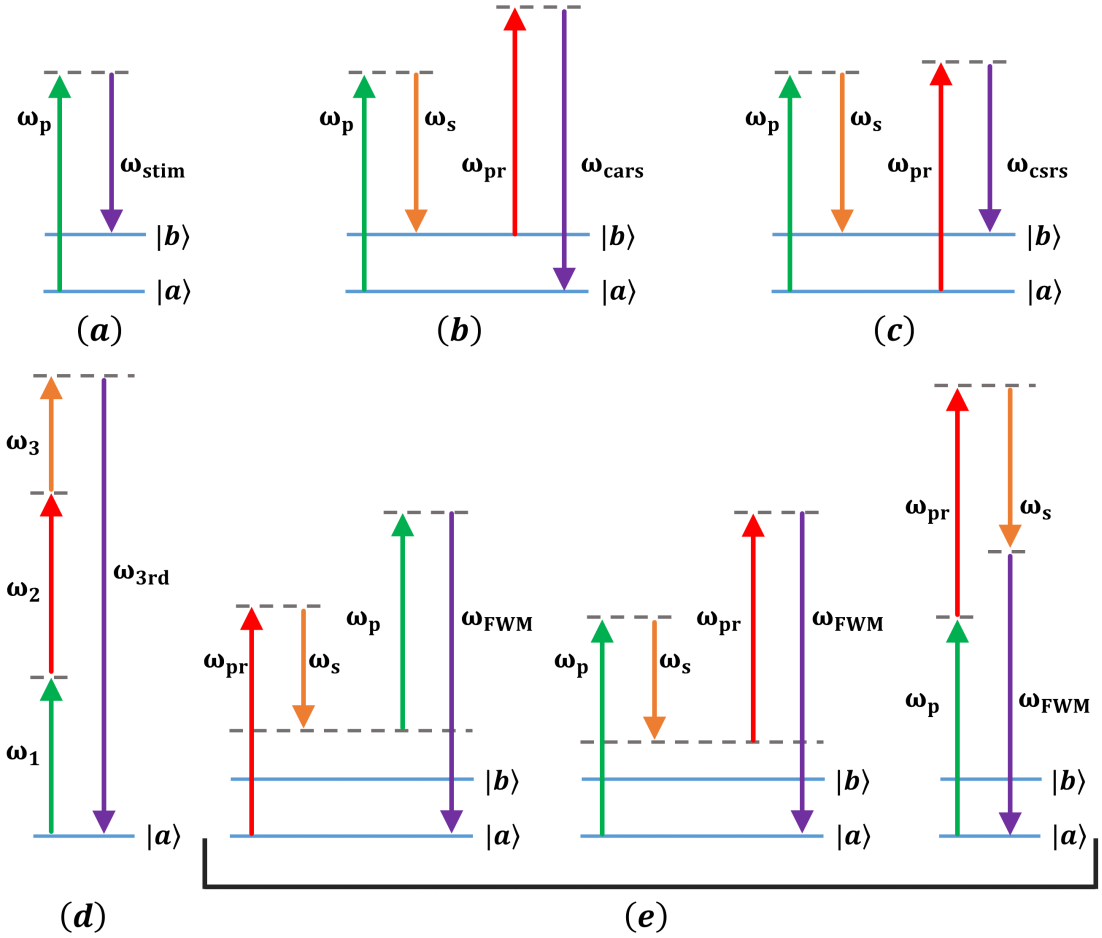

Figure 4.1: **Various Third Order Nonlinear Processes (a)** Stimulated Raman Scattering. It can be achieved either through a very intense Pump field or with a strong pump field and weak probe field. **(b)** Coherent anti-Stokes Raman Scattering. **(c)** Coherent Stokes Raman Scattering. **(d)** Third Harmonic Generation. **(e)** Degenerate four wave mixing. The first two versions tend to occur when a spectrally broad pump is used. When all fields are narrowband, the first two processes do not occur, but the last one remains.

for selective excitation. While ostensibly only two frequencies are used with the pump and Stokes fields, this is still a third order process where the "third" field is a second pump photon. In that case, a pump and the Stokes fields drive the coherence between the vibrational ground and excited state and the second pump photon induces emission at the Stokes frequency. Similarly, if we were to replace the second pump field in the process with a different probe field, the resulting processes would be CSRS or CARS as seen in Fig. 4.1b & 4.1c. CARS is the more frequently used process for molecular identification and microscopy as the output signal is higher in frequency than the pump field, which spectrally separates it from other common fluorescence processes that often occur in samples. Oftentimes CARS and CSRS processes will be actually simultaneously within a sample as the Stokes and anti-Stokes fields reinforce each other. Extending this idea further, this is also true for stimulated Raman, where with an intense enough pump source, a stokes field is not necessary. The pump source alone will generate enough spontaneous Stokes Raman that will seed the stimulated Raman field. Furthermore, if the Stokes field is intense enough, it will also begin generating the anti-Stokes field. Essentially, with a strong enough pump source, one can drive a CARS/CSRS process where the pump and probe fields would be degenerate.

Two other third order nonlinear processes of particular importance are depicted in Fig. 4.1d & 4.1e. Third harmonic generation (Fig. 4.1d) is commonly seen in filamentation processes in air using femtosecond pulses as well as in fiber lasers[25, 104, 57]. Typically, "third harmonic generation" in most conventional lasers is actually achieved through second harmonic generation and subsequent sum frequency generation using the residual fundamental and second harmonic frequency. While this requires two steps to achieve the third harmonic, both SFG and SHG are $\chi^{(2)}$ processes which are much more efficient than just performing a single $\chi^{(3)}$ process. It

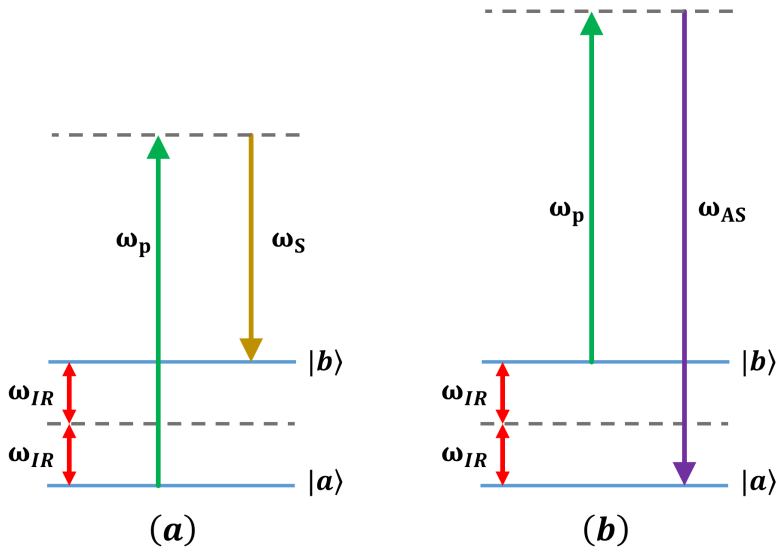

Figure 4.2: **Two Photon Enhanced Raman Schemes (a)** Proposed scheme for double-photon enhanced Stokes Raman emission **(b)** Proposed scheme for double-photon enhanced anti-Stokes Raman emission

is important to note that this scheme shown in Fig. 4.1d can be achieved with three distinct frequencies as well. The last three schemes shown in Fig. 4.1e are different forms of four wave mixing. The first two will occur when the Stokes (anti-Stokes) field in CARS (CSRS) is off resonance, or if a broadband pulse is used in as one of fields, which is often the case in CARS microscopy. If all fields are narrow-band these two four wave mixing processes, tend to be minimized. The last form shown in Fig. 4.1e is the classical depiction of degenerate four wave mixing. Unlike the other two channels, it will always be present, hence the ever-present background in most CARS spectra.

For our purposes, we are interested in a novel third order process utilizing a two photon resonance between the ground state and dipole forbidden excited state. The schemes are depicted in Fig. 4.2. The potential advantage of this approach is that

it should be more efficient in achieving initial coherence for the system as detunings for the two photon resonance are much smaller than the coherence driving fields in CARS and CSRS. If coherence generation is more efficient, then less intensity is needed and lowers the likelihood of burning or damaging the sample. Furthermore, there is essentially no degenerate four wave mixing background. No matter how the scheme is drawn DFWM will only occur at the pump frequency. This is a significant advantage over current CARS techniques as sloping backgrounds for CARS spectra make it difficult to analyze. Lastly, we expect an asymmetric enhancement of the anti-Stokes emission compared to the Stokes emission. The anti-Stokes scheme shown Fig. 4.2b is essentially comparable to the third harmonic generation scheme shown in Fig. 4.1d except now there is a real intermediate level. As such, we expect the typical anti-Stokes generation from the coherent Raman process to be reinforced with this three photon generation. The Stokes field does not enjoy this same enhancement. This effect can be useful not only for microscopy, but also as a potential method for generating new coherent light sources in a gaseous medium.

4.1 Experiment

To experimentally demonstrate this technique, we chose methane (CH_4) as our medium. Methane offers some very attractive qualities. First and foremost, it is extremely well studied and understood. Most of methane's physical parameters have been measured with high accuracy which allows us to have a very clear picture of what we should expect when applying our technique to this system. Furthermore, it is easy to obtain, relatively inert, and extremely relevant as it is used throughout engineering and often part of biological processes. Lastly, as seen in Fig. 4.3, its chemical structure and more importantly its vibrational levels are fairly simple and very distinctly spectrally separated. As it is gaseous, high vapor density is easily

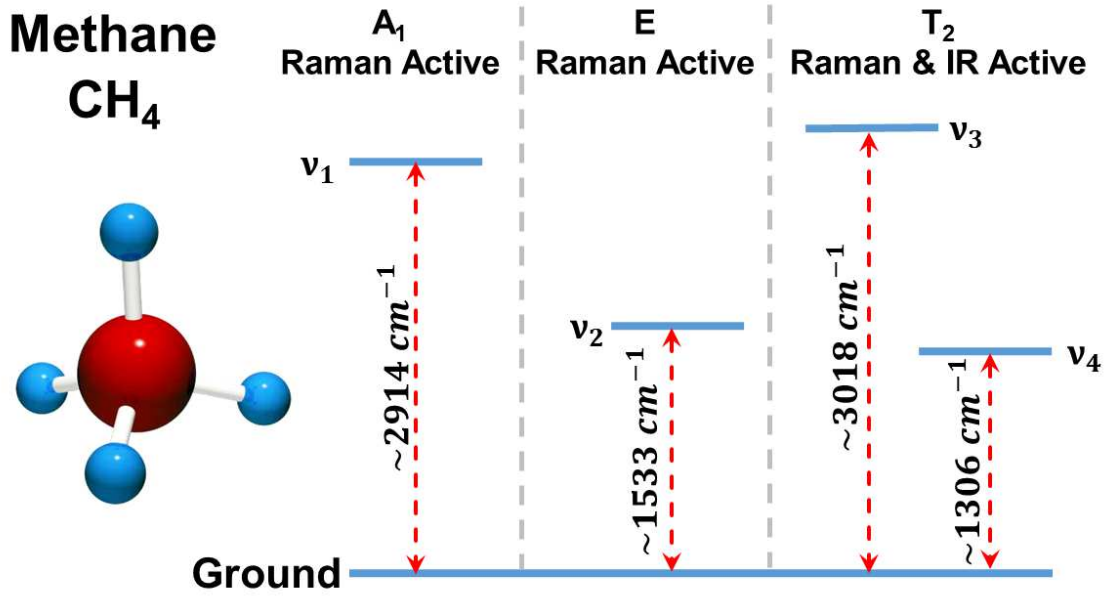

Figure 4.3: **Vibrational Levels of Methane** Methane is an ideal choice for our proof of principle study as it is relatively simple with extremely distinct vibrational levels.

achievable as we use 1-4 atm of pressure throughout our studies.

Fig. 4.4 shows the diagram of our experimental setup. The light source is a Nd:YAG laser (Ekspla, PL2231-50) which outputs 1064 nm light at reposition rate of 50 Hz and pulse width of 28 ps. A portion of this light is frequency-doubled to 532 nm via a second harmonic generation unit (Ekspla, SFGH500-2H). Some of the 532 nm output is then used to pump an optical parametric amplifier (Ekspla, PG501-DFG1) where the idler portion of the beam in combination with a portion of the fundamental 1064 nm source is used to create a tunable IR pulse (wavelength: 2.310 μm) via difference frequency generation. The remaining portion of the 532 nm output and the IR pulse are used as the pump and two-photon coupling, respectively. The maximum energy in the 532 nm and IR pulses were $\sim$330 μJ and $\sim$6 μJ (at 1457 cm^{-1}), respectively. Unfortunately, the energy of both frequencies could not

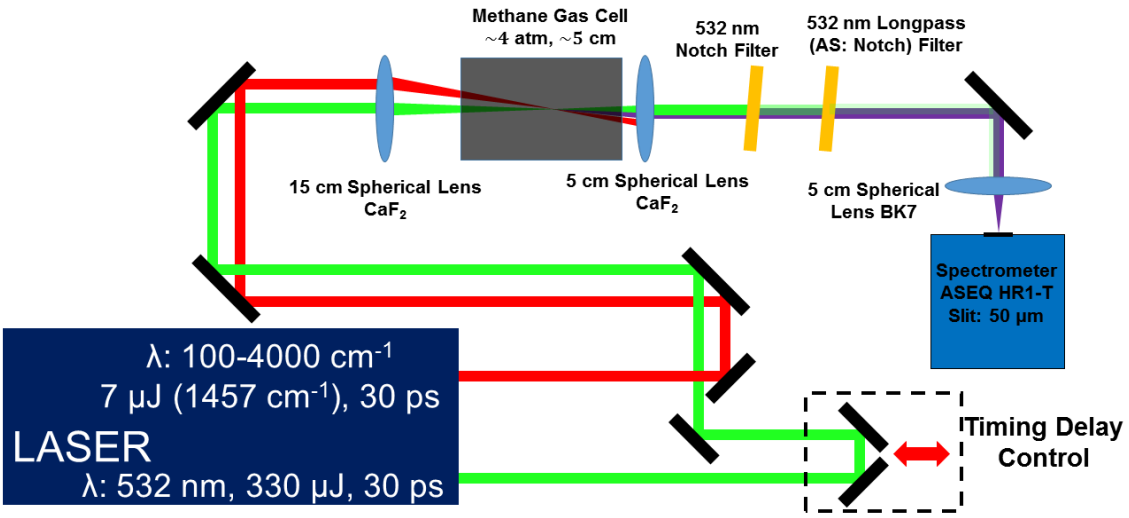

Figure 4.4: **Experimental Setup** The IR and 532 nm beam travelled parallel throughout the beam path with ~1 cm severation between the two beams. This translates to around 2-3° angle between the beams when focused into the cell. The setup between the anti-Stokes and Stokes setup remained exactly the same except for the replacing of a given filter as note in the diagram and the changing out of the actual spectrometer.

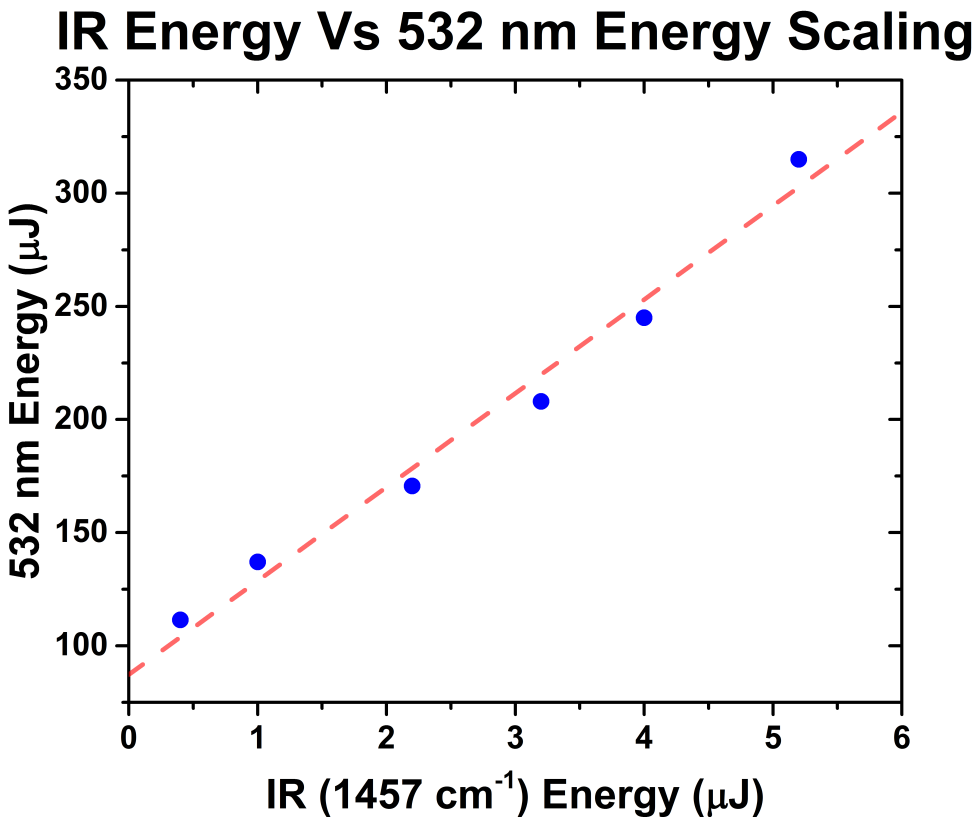

Figure 4.5: **IR Energy vs. 532 nm Energy** The power of both lasers was controlled by changing the electrical current of the Nd:YAG pump sources. Here, we see that output energy for both beams scales linearly as the current of the fundamental pump is varied.

be varied independently as both were controlled by changing the electric current supplied to the fundamental 1064 nm source (see Fig. 4.5 for the energy relation).

Both beams propagated collinearly with with a small ∼1 cm offset between them. Time delay between the 532 nm and IR pulses is controlled by an automatic translation stage by changing the optical path length for the 532 nm laser (Fig. 4.4). The beams are then focused into a 5 cm long methane cell using a 15 cm CaF_2 convex lens. A 5 cm CaF_2 convex lens was placed on the other side of the cell to collect the light from the focal region inside the methane cell. Two filters were then placed in

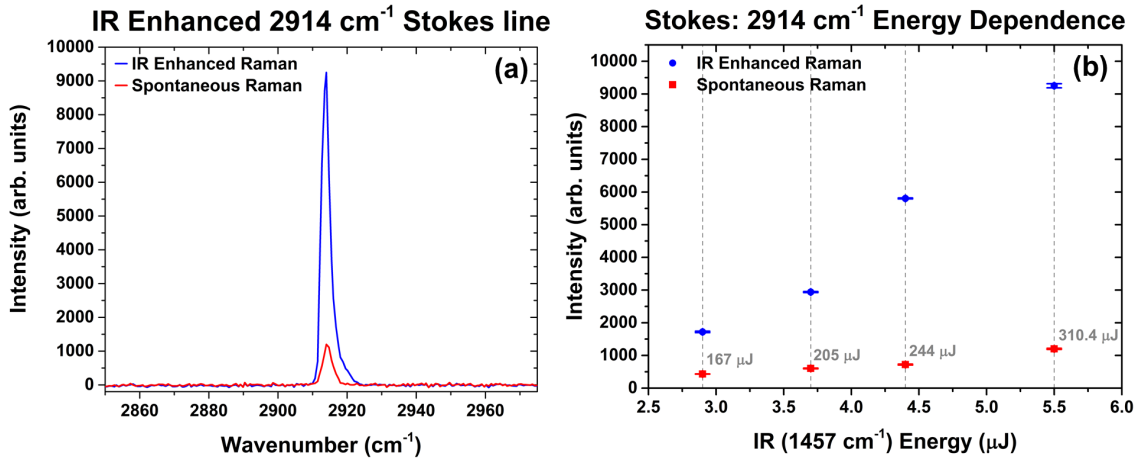

Figure 4.6: **Observed Two Photon Enhanced Stokes (a)** Comparison of Spontaneous Raman spectra to the Two photon enhanced Raman signal. The exposure time for both spectra was 30 s. **(b)** Energy dependence of the spontaneous Raman and the two-photon enhanced Raman signals. The slope for the enhanced Raman energy dependence is significantly steeper and possibly nonlinear, indicating a coherence/stimulated process. The values in grey by the data points correspond to the 532 nm pump energy at those values of IR energy.

the output beam path to remove the excess 532 nm pump. For the Stokes study the two filters were a 532 nm notch filter as well as a long-pass filter with a wavelength cutoff at 532 nm. For the anti-Stokes study the longpass filter was replaced with a second 532 nm notch filter. After the filters the output was focused onto the 50 μm slit of a spectrometer (ASEQ HR1-T), which for the Stokes study had a fixed wavelength range of 550-650 nm and a resolution of .12 nm. For the anti-Stokes study, the other ASEQ spectrometer possessed a the wavelength range was from 445-525 nm, and a resolution of .07 nm.

Initial results using the 532 nm pump with the IR laser blocked, showed spontaneous Raman (Fig. 4.6). Unfortunately, given the less than ideal conditions for our data acquisition as well as the limitations of the spectrometer, the only visible Raman line of methane was the ν_1 (A_1) transition at 2914 cm^{-1} which also happens

to be the strongest vibration due to the $C-H$ bond stretch. The fact that this was in fact spontaneous Raman was confirmed by checking its directionality as seen in Fig. 4.8a where and iris was placed in the beam path into the spectrometer. The iris was closed such that only a 2 mm aperture was left open. This was the diameter such that the 532 nm beam was just starting to clip on the iris with $\sim 10\%$ loss of energy. When the iris was closed the Raman signal decreased, which implies that the Raman signal was much wider than the 532 nm beam. This supports the claim that this was simply spontaneous Raman, as spontaneous Raman scatters uniformly in 4π and therefore the Raman signal collected by the 5 cm lens would have a much wider diameter than that of the 532 nm pump beam. This was not the case for the two-photon enhanced Raman as we'll discuss later. Furthermore, the Raman signal also scaled linearly with increasing 532 nm pump energy (see Fig. 4.6b), which also supports that the observed Raman signal without the IR field was in fact spontaneous Raman.

Next, we unblocked the IR beam and scanned it across its full range from 2 to 10 μm (5000 to 1000 cm^{-1}). Little to no changes were observed in the Raman spectrum except when the IR beam was at 1457 cm^{-1} ($\sim$6864 nm). At this frequency, an approximately 10$\times$ enhancement was observed for the 2914 cm^{-1} Raman line (Fig. 4.6a). Conceptually, this is due to the IR field being in two-photon resonance with the ν_1 transition of methane at 2914 cm^{-1}. The IR field drives the coherence between the ground and excited vibrational state allowing coherent emission at the Stokes wavelength when probed with the intense 532 nm field (see Fig. 4.7). Further evidence that this process is occurring is depicted in Fig. 4.6b where the energy dependence of this emission is studied. Here, we see that the enhanced Raman signal grows with increasing energy at a rate much faster than the spontaneous Raman signal, thus increasing the enhancement factor with increased energy. The

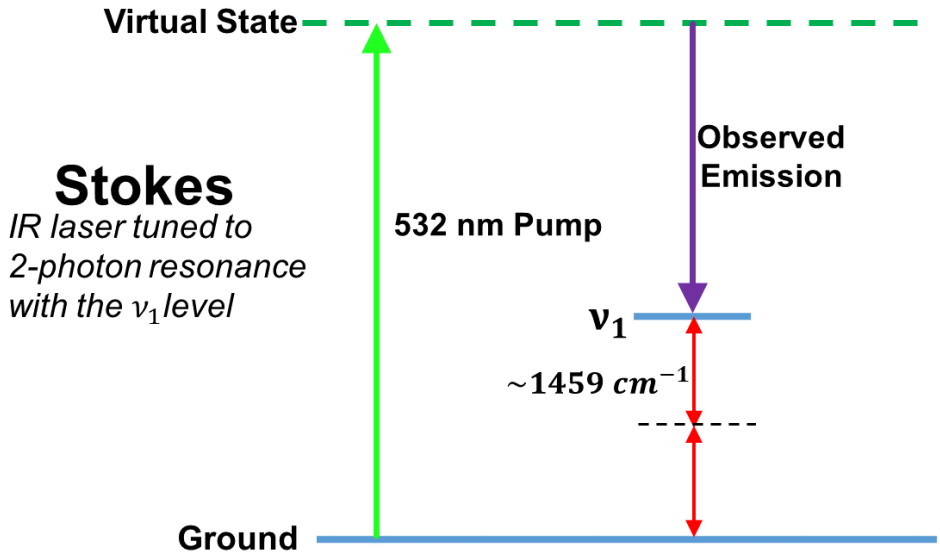

Figure 4.7: **Stokes Scheme** The IR laser was scanned across its full spectral range, but enhancement of the Raman signal was only observed when the IR was near 1457 cm^{-1}, the two photon resonance of the ν_1 Raman-active transition.

growth of the enhancement factor points very strongly to a nonlinear process. Lastly, we confirmed that the directionality of the two-photon enhanced emission as we'd expect a very distinct directionality of the emission along the pump beam path since similar coherence processes like CARS and SRS require phase-matching. When the iris was closed to 2 mm for the enhanced Raman signal, we actually saw an increase to the Raman signal via the spectrometer (Fig. 4.8b). This may seem counterintuitive, but this is indicative that the two-photon enhanced beam is in fact highly directional. When the enhanced Raman signal is clipped by the iris, it causes it to diffract and fill more of the collection optic allowing more light to enter the spectrometer slit. This process would not occur unless the emission is highly spatially localized and coherent.

While we have definitely demonstrated coherent Raman emission of the Stokes

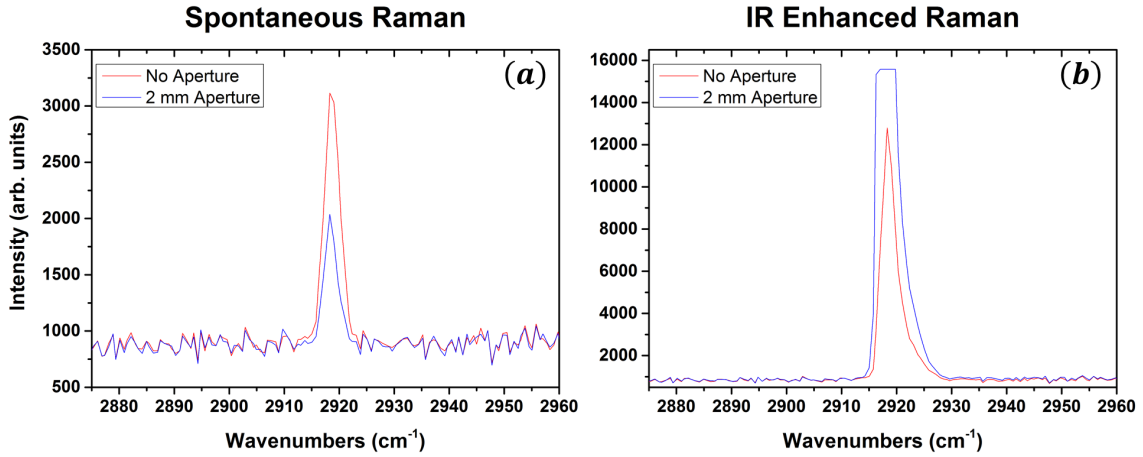

Figure 4.8: **Stokes Directionality Study** An iris was placed along the output beam path to verify the directionality of the emission. The iris was then closed such that it was just clipping the 532 nm pump on the output of the methane cell. Spectra were then taken for both the spontaneous Raman **(a)** and the two-photon enhanced emission **(b)** with when th

lines by two photon resonance of an IR field, there was still an open question as to why the enhancement was only a factor of 10× when CARS and SRS typically achieve several orders of magnitude enhancement. Furthermore, we were not able to observe the ν_3 vibrational mode at 3018 cm^{-1} of methane despite this enhancement, though its Raman cross-section is much smaller than the ν_1 mode. The ν_2 & ν_4 vibrational modes were inaccessible for 2-photon enhancement as the IR laser could not be tuned those wavenumbers. Fortunately, by studying the anti-Stokes emission, we were able to shed some light on the underlying mechanisms driving this process as the anti-Stokes emission exhibited slightly different behavior.

For the anti-Stokes study, we essentially examined the same parameters as in the Stokes study. First, we verified that there was in fact no spontaneous Raman when the 532 nm pump field was allowed to propagate through the methane cell and the IR field was blocked. This matches with all prior experiments and theory as

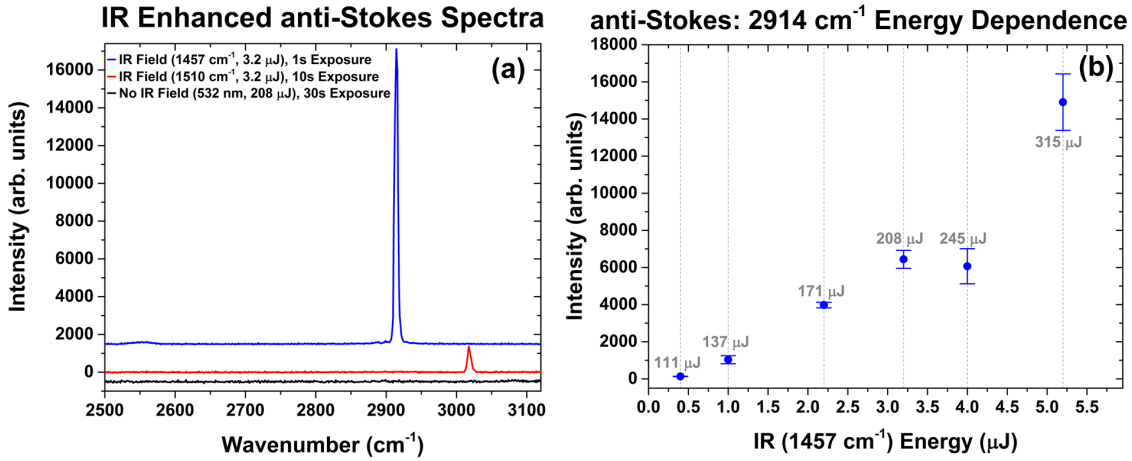

Figure 4.9: **Observed Two-photon Enhanced anti-Stokes (a)** Comparison of anti-Stokes Raman spectra under various conditions. Note the significant difference in exposure times. **(b)** Energy dependence of the two-photon enhanced Raman signals. The values in grey by the data points correspond to the 532 nm pump energy at those values of IR energy.

a good portion of the methane population would need to already be in the excited vibrational state for anti-Stokes emission to occur. Without a coherent drive, the only way for population to be in the excited state is for it to be thermally populated. This ratio of population can easily be found through the Boltzmann factor:

$$\frac{F_2}{F_1} = e^{\frac{E_1 - E_2}{k_b T}} \tag{4.3}$$

where F_i is the population and E_i is the energy in a given state, T is the temperature and k_b is Boltzmann's constant. Therefore at room temperature, 20° C, the population of the ν_1 vibrational mode relative to the ground state is 6×10^{-7} smaller. As spontaneous Raman emission scales linearly with population, the spontaneous anti-Stokes emission would be 7 orders of magnitude weaker and likely unobservable with our setup.

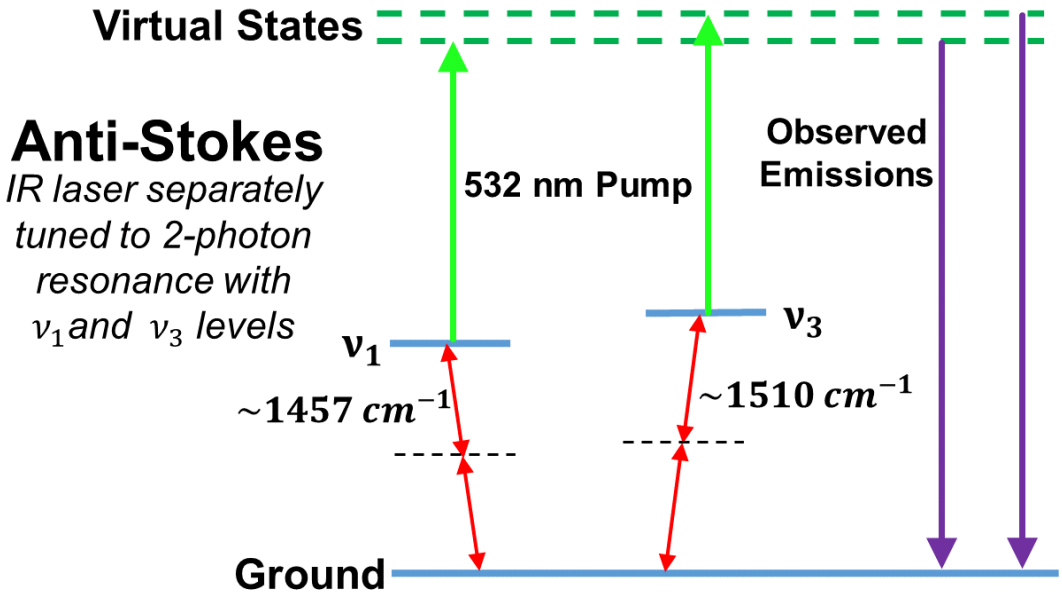

Figure 4.10: **anti-Stokes Scheme** The IR laser was scanned across its full spectral range, with strong emission observed from the ν_1 and ν_3 when the IR field was near the two photon resonance for each respective vibrational mode.

When the IR laser was allowed to propagate through the cell, we again observed strong emission at the ν_1 mode, 2914 cm^{-1}, when the IR field was tuned to 1457 cm^{-1}. Furthermore, we also observed emission from the ν_3 vibrational mode at 3018 cm^{-1} when the IR field was at 1509 cm^{-1}, the two-photon resonance. While the ν_3 is still a strong emission process, it is significantly weaker than the ν_1 emission, but this is to be expected as the ν_3 has a much smaller Raman cross-section. Example spectra for both of these are shown in Fig. 4.9 and the energy scheme is depicted in Fig. 4.10. Both of these processes must be coherent emission as neither peak is present without the IR field.

The anti-Stokes emission is approximately 50× more intense than the Stokes emission at full pump energy (see Fig. 4.11). This asymmetry between the Stokes and anti-Stokes fields is extremely significant as there are very few situations in

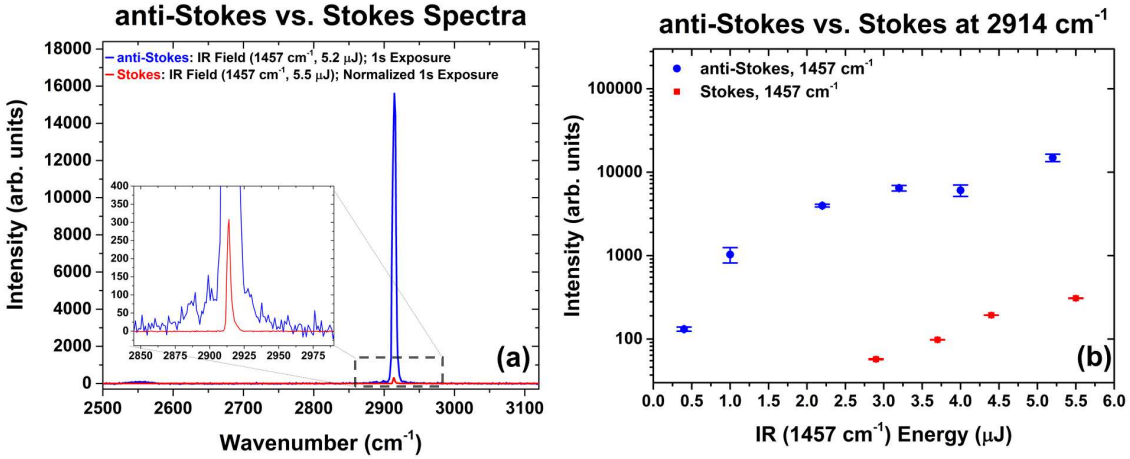

Figure 4.11: **Comparison of anti-Stokes and Stokes Emission (a)** Spectra for both the anti-Stokes and Stokes two-photon Raman emission. The spectra have been scaled to the same exposure time. **(b)** Energy dependence comparison.

the CARS, CSRS, and SRS processes where the anti-Stokes is orders of magnitude stronger than the Stokes. In most situations for conventional coherent Raman the best that can be done for anti-Stokes emission is equivalent energy to the Stokes field. This is due to the fact that these four wave mixing processes are self-reinforcing: if an intense Stokes field is generated, it will act as a strong coupling field for the anti-Stokes emission and so the anti-Stokes will increase, which in turn will strengthen the Stokes emission until saturation of both fields occur. Varying the angles between the driving fields allows the researcher to manipulate the phase-matching conditions and thus shift the balance of the field strengths, but never to this degree in favor of the anti-Stokes field.

To fully explain this asymmetry between the anti-Stokes and Stokes emission, it is best to go back and reexamine the pumping schemes (Fig. 4.2). Upon close examination, one realizes that there is an extra process occurring in the anti-Stokes pumping scheme that is not present in the Stokes: a third harmonic-like generation.

This process is not self-reinforcing, ie once the three photons from the drive fields sum, there isn't really a viable method for any of these fields to generate a Stokes. The Stokes field comes primarily from the coherence generated in the Raman scheme and would likely not be present at all if there wasn't a resonant two-photon transition. While this seems like a very reasonable explanation, is there any actual evidence to support that this three wave summation is occurring in conjunction with the coherent Raman mechanisms? The answer is "yes".

During our spectral scan of the IR laser, we also observed emission not on resonance with any of the vibrational modes of methane (Fig. 4.12a) Furthermore, this emission occurred when the IR pump was detuned from the 2-photon resonance (Fig. 4.12b). This emission corresponds to the three wave summation of a 532 nm pump photon and two IR photons, $\omega_{obs} = \omega_p + 2\omega_{IR}$. The emission grows in intensity exponentially as the detuning of the IR field goes to zero as well as the emission itself moves to zero detuning. The three-wave summation and the anti-Stokes Raman seed each other increasing the overall amplification of the emission. Despite essentially two processes occurring simultaneously, the overall emission intensity when on resonance is still limited by the Raman cross-section, as illustrated by the peak intensity at the ν_1 and ν_3 vibrational modes.

One interesting aspect is the distinct difference in spectral "width" around resonance between Fig. 4.12a & 4.12b. In Fig. 4.13 we've plotted the emission wavenumber versus the IR driving field using the data in Fig. 4.12 to better understand how the emission behaves near resonance. What is apparent, is that when the IR laser is just slightly detuned from the two-photon resonance of a vibrational mode, the emission still occurs at the vibrational resonance. This is likely due to the coherent Raman frequency mode being intense enough to spectrally pull the three photon summation to frequency of the Raman emission, though the intensity of the overall

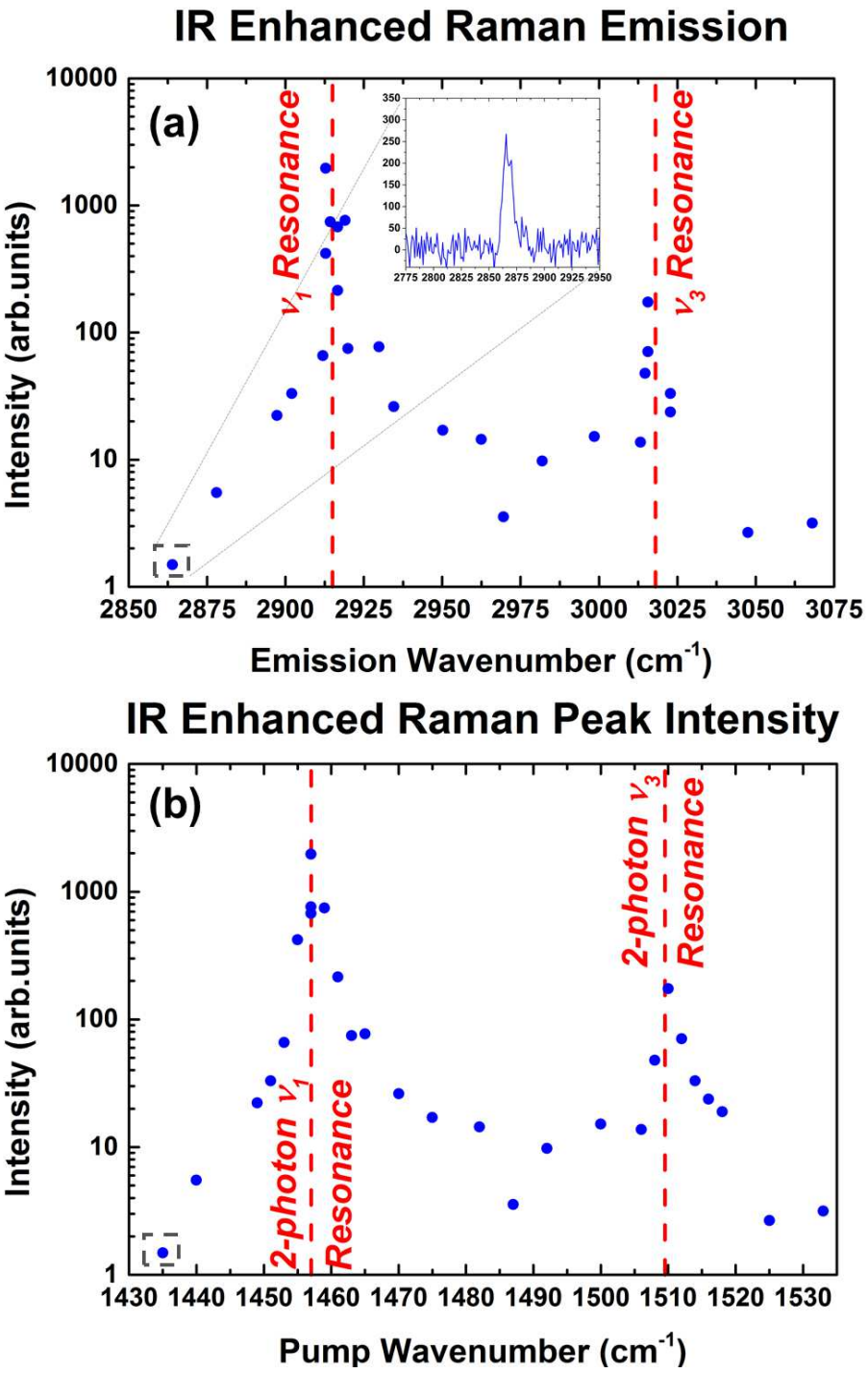

Figure 4.12: **Emission Intensity Dependence on IR Pump and Emission Wavenumber (a)** Intensity of emission at different emission wavelengths. **(b)** Intensity of emission at different IR pump wavelengths. All intensity values were normalized to a 1 second exposure time.

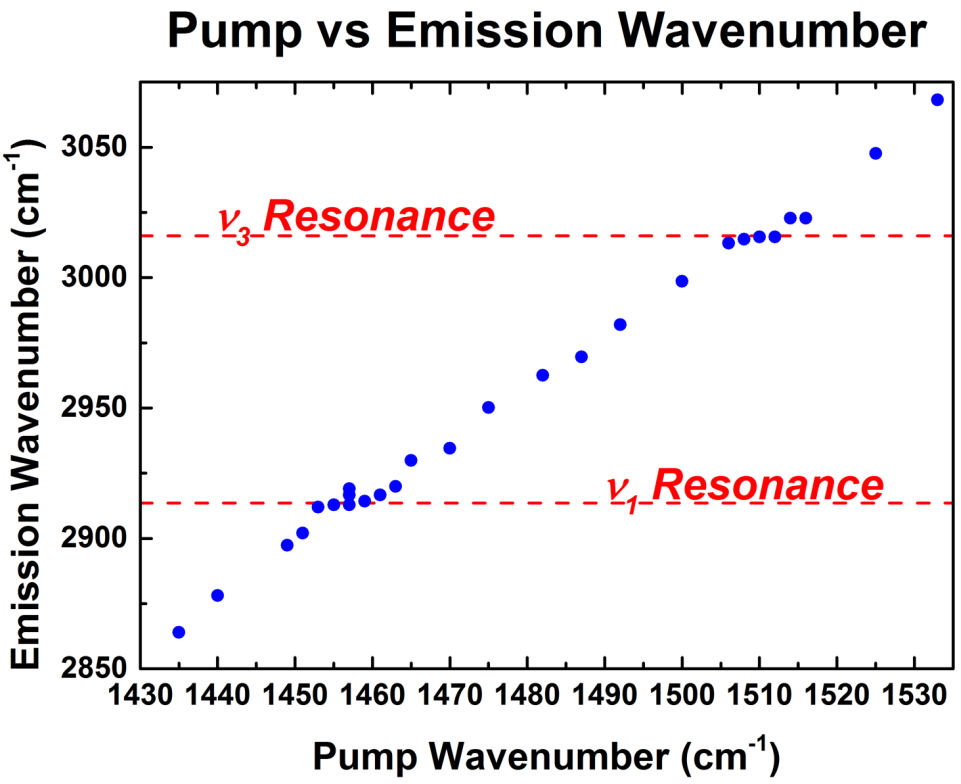

Figure 4.13: **anti-Stokes Emission Wavenumber vs IR Wavenumber** When the IR laser is slightly detuned from the 2-photon resonance of the vibrational modes, the emission still occurs at the resonance of the Raman mode.

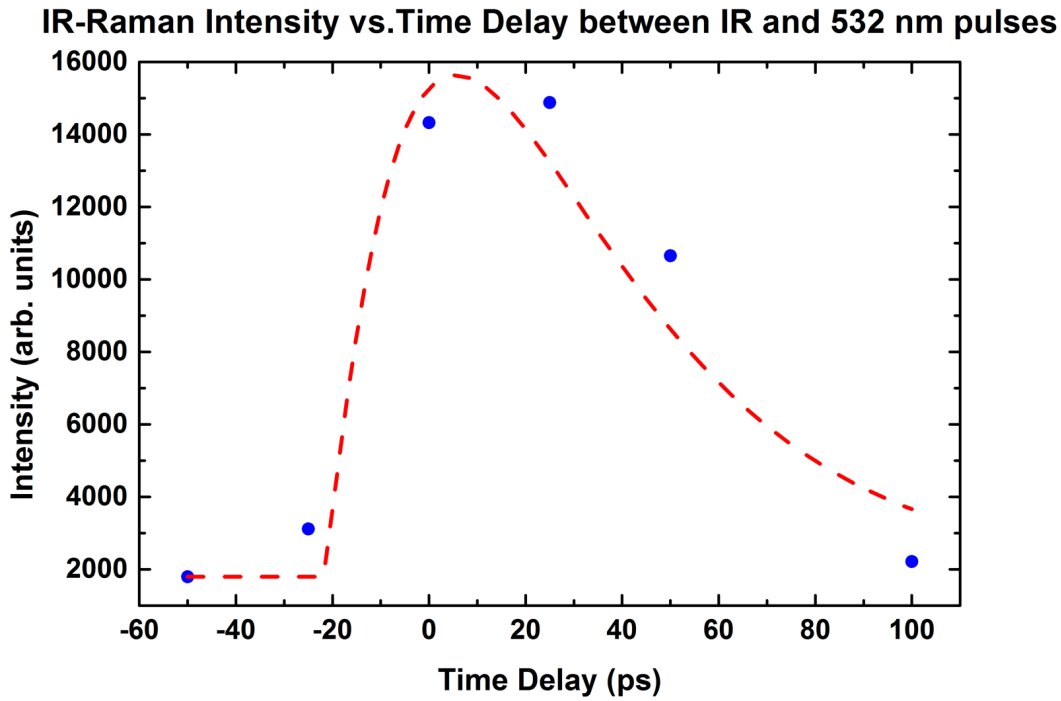

Figure 4.14: **Emission as a function of Delay Time** Time $t = 0$ corresponds to complete pulse overlap. Both pulses are approximately 28 ps in duration. The enhance emission present at 50 ps, well past pulse overlap, is highly indicative of vibrational coherence playing a signigicant role. Decay times for vibrational states of molecular gases at room temperature are the order of 10s of ps.

emission is still weaker when the IR laser is slightly off resonance as evidenced by Fig. 4.12. At a far enough IR detuning, the emission reverts to three-photon summation.

Lastly, we examined the anti-Stokes emission in the time domain to see the role of the vibrational coherence on the emission intensity. For nonresonant processes like four wave mixing, the emission essentially turns off once the fields are not overlapped. In contrast, CARS does not need direct temporal overlap of the driving fields. Once coherence has been established by the pump and Stokes fields, coherent emission can be achieved with a delayed probe pulse so long as the coherence has not decayed. Here, in Fig. 4.14 with our IR field on 2-photon resonance with the ν_1 vibrational mode, we see that the enhanced emission is still achievable after the IR pulses have

left the gain region. If the process was like non-resonant four wave mixing, we'd expect the intensity to be symmetric around time $t = 0$ instead of having an abrupt turn on time and subsequent tale before the coherence decays.

4.2 Theory

To model the mechanism behind this two-photon enhanced Raman emission, we can extend Boyd's intuitive derivation of simulated Raman scattering[11]. We start by assuming our Raman transition is a damped driven oscillator:

$$\frac{d^2q}{dt^2} + 2\gamma\frac{dq}{dt} + \omega_\nu^2 q = \frac{F(t)}{m} \tag{4.4}$$

where q is the oscillator's deviation from equilibrium, ω_ν is the molecular resonance, γ is the damping constant, and $F(t)$ is the driving force. In this case this driving force is caused by the oscillating dipole moment. Therefore, we want to express the driving force $F(t)$ as a function of the electric field. To accomplish this we use the definition of the work needed to establish a dipole:

$$W = \tfrac{1}{2}\left\langle p(z,t)\cdot E(z,t)\right\rangle = \tfrac{\varepsilon_0\alpha(t)}{2}\left\langle E^2(z,t)\right\rangle. \tag{4.5}$$

Where $p(z,t)$ is the dipole moment defined as $p(z,t) = \varepsilon_0\alpha(t)E(z,t)$, and $\alpha(t) = \alpha_0 + \left(\frac{\partial\alpha}{\partial q_0}\right)q$ is the polarizability. Using these definitions we can define the force as:

$$F(t) = \frac{\partial W}{\partial q} = \tfrac{\varepsilon_0}{2}\left(\tfrac{\partial\alpha}{\partial q_0}\right)\left\langle E^2(z,t)\right\rangle \tag{4.6}$$

Where we can define the electric field as the summation of propagating fields for each of our frequencies:

$$E(z,t) = A_L e^{i(k_L z - \omega_L t)} + A_s e^{i(k_S z - \omega_S t)} + A_a e^{i(k_a z - \omega_a t)} + A_1 e^{i(k_1 z - \omega_1 t)} + A_2 e^{i(k_2 z - \omega_2 t)} + c.c. \tag{4.7}$$

Here, A_i are the the amplitudes of the fields, k_i are their wave-vectors, and ω_i are their frequenices, with L corresponding to the pump wavelength (the 532 nm laser in our case), S the Stokes field, a the anti-Stokes field, and 1 & 2 corresponding to the "two" fields of the IR laser pulse. Now we have full expression for $F(t)$ in terms of the components of the electric field. Assuming a solution of the form:

$$q = q(\Omega) e^{i(Kz - \Omega t)} + c.c. \tag{4.8}$$

with Ω and K corresponding to the Raman transition frequency and wave-vector, $\Omega = \omega_L - \omega_S$ & $K = k_L - k_S$. Now subsituting this solution in to the damped driven harmonic oscillator equation as well as the time varying parts of $F(t)$ that have a frequency and wave vector equivalent to Ω and K, we have:

$$-\Omega^2 q(\Omega) - 2i\Omega\gamma q(\Omega) + \omega_\nu^2 q(\Omega) = \frac{\varepsilon_0}{2}\left(\frac{\partial\alpha}{\partial q_0}\right)\left[2A_L A_S^* + 2A_a A_L^* + (A_1 + A_2)^2\right] \tag{4.9}$$

Now we can solve and have expressions for $q(\Omega)$ & $q^*(\Omega)$ which we will need moving forward. Our goal is to find an expression for the nonlinear polarization to be used in the nonlinear wave equation which we introduced earlier in this chapter. Thus, we make use of this expression for the polarization:

$$P(z,t) = N \cdot p(z,t) = N\left[\alpha_0 + \left(\frac{\partial\alpha}{\partial q_0}\right) q\right] E(z,t) \tag{4.10}$$

From here if we take the nonlinear portion of the polarization and divide it into

frequency components, we have:

$$P^{NL}(z,t) = N\left(\frac{\partial\alpha}{\partial q_0}\right)\left[q(\Omega)\,e^{i(Kz-\Omega t)} + c.c.\right]E(z,t) = P_S^{NL}(z,t) + P_a^{NL}(z,t) + ... \tag{4.11}$$

where $P^{NL}(z,t)$ is the total nonlinear polarization and $P_a^{NL}(z,t)$ & $P_S^{NL}(z,t)$ are the nonlinear polarizations for the anti-Stokes and Stokes field respectively, such that we can write both of them in the form

$$P_S^{NL}(z,t) = P(\omega_S)\,e^{i\omega_S t} + c.c. P_a^{NL}(z,t) = P(\omega_a)\,e^{i\omega_a t} + c.c. \tag{4.12}$$

Both $P(\omega_S)$ & $P(\omega_a)$ are completely known coefficients, each being the collection of terms from the expression for $P^{NL}(z,t)$ for their respective frequency components ($e^{ik_S z}$). At this point, most of the literature defines the susceptibility $\chi^{(3)}(\omega_i)$ based on these coefficients comprising $P(\omega_i)$ terms (excluding the z oscillating exponential and the field amplitudes A_i), as it is extremely convenient and the susceptibility itself for each term provides good insight. Due to complicated nature of our terms, we'll refrain from doing so here as it is an ancillary step, especially once we have the solutions for the propagation of the fields $A_S(z)$ & $A_a^*(z)$.

Now that we have expressions for the nonlinear polarization, we can now insert them into the nonlinear wave equation, which we we've rewritten down below for convenience and then solve the system of differential equations to find the field propagations for the Stokes and anti-Stokes fields, $A_S(z)$ & $A_a^*(z)$, respectively.

$$\nabla^2 E - \frac{n^2}{c^2}\frac{\partial^2}{\partial t^2}E = \frac{1}{\varepsilon_0 c^2}\frac{\partial^2}{\partial t^2}P^{NL} \tag{4.13}$$

Once the differential equations are solved with a few approximations, what we

find is a mismatch in the gain terms for the Stokes and anti-Stokes $A_S(z)$ & $A_a^*(z)$.

$$A_S(z) \propto e^{\left[R-\frac{1}{2}(\alpha_a^*+\alpha_s)\right]z} e^{i\Delta k_1 z/2} A_a(z) \propto e^{\left[R+\frac{1}{2}(\alpha_a^*+\alpha_s)\right]z} e^{i\Delta k_1 z/2} \tag{4.14}$$

Where the coefficient $R = \sqrt{4\kappa_a^*\kappa_S + (\alpha_a^* - \alpha_s - i\Delta k_1)^2}$. This imbalance in the gain term allows for the increased amplification of the anti-Stokes field relative to the Stokes.

An alternative method for modeling the problem can be found in a text by Reintjes[83]. The approach described there treats each third order scheme separately and determines a susceptibility for each. Then a full actualized system can be represented as the combination of these susceptibilities, $\chi^{(3)}(\omega_i)$.

4.3 Discussion

Here, we have demonstrated a unique third order process where coherent Raman emission is achieved via two photon resonance. This technique is extremely efficient due to the small detuning of the coupling for the two photon resonance, and background free as any degenerate four wave mixing simply produces more of the pump beam. This technique also offers asymmetric gain along the anti-Stokes. This technique shows great promise for microscopy applications particularly for surface imaging in biomedical applications as overall intensity of the pump fields is lower so less chance of damaging or altering the sample. Alternatively, it could also be implemented for molecular gas detection given its high gain. Furthermore, due to the strong anti-Stokes field, it could be scaled up for longer gain lengths to create a viable a VUV/UV coherent source. On the whole, this an unreported mechanism with endless possibilities for future applications.

5. DUAL RAMAN BRILLOUIN MICROSCOPE*

Since its inception, Raman microscopy has become a staple technique with a diverse range of applications in an equally diverse number of fields spanning industrial product inspection, scientific research, and medical diagnostic sensing [82, 47, 79, 22, 7, 68, 9]. Even now, novel adaptations of Raman spectroscopic imaging have been realized for tomography and noninvasive deep tissue diagnosis[66]. In contrast, Brillouin scattering is only now beginning to enjoy widespread adoption[90, 76]. Brillouin scattering is an emerging biomedical tool that has already been used to study bone, collagen fibers, cornea, and crystalline lens tissue[89, 52, 32, 108]. Unlike Raman spectroscopy, which offers information about the chemical makeup of the sample, Brillouin spectroscopy provides information about the viscoelastic properties of a material, and consequently, can characterize larger bulk changes. Each of these imaging tools offers useful diagnostic information, therefore a single apparatus that could provide simultaneous measurement of both spectra from the same point would be extremely powerful for sample characterization and analysis.

So far, complementary use of Raman and Brillouin microscopy has only been reported once, and the spectra were acquired using separate instruments[76]. Long acquisition times ($\sim$10 minutes) for each Brillouin spectra are clearly impractical, and a lack of same-point detection for both spectra makes the analysis complicated. To overcome these issues, we use a single pump laser to generate both Raman and Brillouin spectra and provide simultaneous imaging from the selected confocal volume. More importantly, we take advantage of recent advancements in Brillouin

*Part of this chapter is reprinted with permission from "Dual Raman-Brillouin Microscope for Chemical and Mechanical Characterization and Imaging." by Traverso, A. J. et al. , (2015). *Analytical Chemistry*, 87 (15), 7519-7523 .

spectroscopy to decrease the acquisition time, as any practical implementation of simultaneous detection requires that the times for both to be comparable. Unlike other approaches that use scanning Fabry Perot cavities, we utilized a virtually imaged phase array (VIPA), which offers a higher throughput efficiency, ¿80%, and does not require scanning to extract a complete spectrum [90, 76, 95, 91, 71, 86]. Subsequently, a VIPA-based system drastically cuts down the acquisition time, which was traditionally a limiting factor in Brillouin spectroscopy. The major challenge in Brillouin spectroscopy of biological systems is eliminating the large amount of elastic scattering, which makes it difficult to identify a weak Brillouin peak. We recently reported that this limitation can be overcome by using a molecular/atomic gas cell as a notch filter[69]. Utilizing these advancements, we demonstrate simultaneous Raman-Brillouin microscopy, a potent new tool for imaging and analytical characterization.

Both Raman and Brillouin phenomena arise from the inelastic scattering of light, where the scattering causes the frequency of light to shift in accordance with some resonant property. In the case of Raman, the incident light interacts with molecular vibrations causing the light to shift according to $\omega_s = \omega_0 \pm \Omega$ where ω_0 is the pump laser frequency and $\hbar\Omega$ is the energy difference between the excited vibrational level and the ground state (Fig.5.2 Inset). Consequently, given the unique vibrational levels of each molecule, this process provides a method to identify molecular constituents of a material.

Similarly, Brillouin scattering is caused by the inelastic interaction of light with periodic fluctuations in a materials index of refraction. These fluctuations are caused by acoustic phonons, and carry information about a materials bulk compressibility and viscoelasticity [108]. Whereas Raman scattering can have frequency shifts on the order of 100 THz, Brillouin shifts are only on the order of 10 GHz due to the

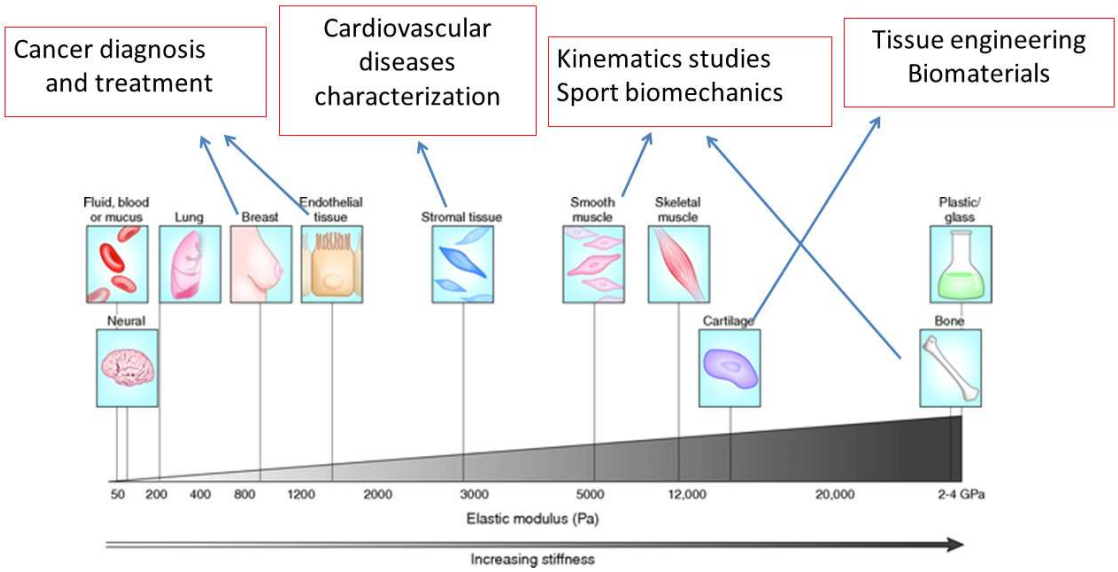

Figure 5.1: **Elasticity Measurements as a Biological Probe** Elasticity varies significantly across biological materials, which would allow Brillouin microscopy to be implemented as a great imaging device as the wide variance would provide high contrast.

relatively low energy of the acoustic phonons[77]. The magnitude of the Brillouin shift is dependent upon the collection geometry, following $\Omega = \pm 2\,(nV_L/\lambda_0)\sin(\theta/2)$, where n is the index of refraction of the material, V_L is the speed of sound in the material, $_0$ is the wavelength of the incident light and θ is the angle between the incident and scattered light. Through the measured Brillouin shift we are able to extract mechanical properties of the material, including the speed of sound, adiabatic compressibility, and the longitudinal modulus. In particular, the longitudinal modulus, M, can be determined through the speed of sound, as $V_L = \sqrt{M/\rho}$, where ρ is the density of the material[98].

Brillouin microscopy has the potential to fills a very important niche where essentially no competing technologies exist. Currently, elasticity is measured through one of two major techniques: atomic force miscoscopy or ultrasound. These two

techniques cover very different regimes. Commercial ultrasound measures elasticity on a millimeter and centimeter scale, while atomic force microscopy probes elasticity on the nanoscale. No present commercially available technique is available that can study elastic properties on a microscopic scale (0.1 100 microns) on a time scale of milliseconds to minutes. Elasticity measurements on this scale are very important in biology as the elastic properties of cellular and sub-cellular structures provide a better understanding of cellular and tissue biomechanics. Biomechanics is important for understanding many diseases and for exploring the way those diseases can be treated. Fig. 5.1 depicts the wide variance of elasticity for various biologically relevant materials as well as potential applications.

In linear elasticity theory, the longitudinal modulus of isotropic materials is defined as $M = K + (4/3)\,\mu$ where K is the bulk modulus of the material and μ is Lamés second parameter, defined as the shear modulus in solids and the dynamic viscosity in fluids. Because μ is often small in the case of fluids, the longitudinal modulus measured in Brillouin spectroscopy is frequently taken to be equivalent to the bulk modulus. This is acceptable in our case, as the materials we are characterizing are isotropic and either fluid or fluid-like. However, complications arise when anisotropies are introduced, and special care must be taken to ensure that the intended parameters are in fact the ones being measured[120]. While Brillouin scattering is most often used to measure elastic properties of materials, the linewidth of the Brillouin shift also provides information about the viscoelasticity.

Beyond the actual Brillouin shift, the linewidth of a Brillouin peak also provides valuable information about a material. The Brillouin linewidth fully describes the viscous properties of the material. The full-width half max (FWHM) of the Brillouin peak is defined as $\Delta = \frac{1}{\tau_p} = \alpha\frac{V_L}{\pi}$, where τ_p is the phonon lifetime and is the acoustic attenuation coefficient[S2]. The imaginary part of the longitudinal modulus

is defined as $\mathrm{Im}\,(M) = 2\rho {V_L}^3 \alpha/\omega$, where ω is the angular frequency of the shift. Since the imaginary component of the modulus describes the viscous properties of a material, and the real part is determined, it is possible to fully reconstruct the complex longitudinal modulus of any given material.

5.1 Experimental Setup

Our experimental setup, sketched in Figure 5.2, is based on an extended cavity diode laser (ECDL) centered at 780.24 nm, with an output power of ∼100 mW (Sacher Lasertechnik; Lion Series). The above wavelength was chosen as it corresponds to the strong D_2 $\left(5^2S_{1/2} \rightarrow 5^2P_{1/2}\right)$ transition in rubidium (Rb), which acts as an ultra-narrow notch filter for the Brillouin spectrometer. Furthermore, 780 nm lies within the tissue transparency window, allowing for biological material characterization. Low absorbance at this wavelength makes it unlikely to alter or damage biological samples.

In general, Brillouin microscopy imposes more stringent standards for the laser system when compared to Raman microscopy. Brillouin shifts are inherently low energy effects, with typical shifts of a few GHz and narrow (∼1GHz) linewidths. Any laser instability is more detrimental than in Raman spectroscopy, since small amounts of laser drift can cause the system to lose resonance with the gas cell, broaden the Brillouin peaks, and distort the spectrum. Because of this, the pump laser must be narrowband and possess long-term frequency stability. This is especially true for long imaging scans. Ideally, the laser should be locked with feedback electronics to the notch filter transition of the gas cell.

The use of the Rb cell as a notch filter is necessary, as the elastically scattered light from a sample is usually intense enough to obscure the Brillouin signal[69]. In Raman spectroscopy, conventional long-pass and dielectric notch filters are sufficient as the

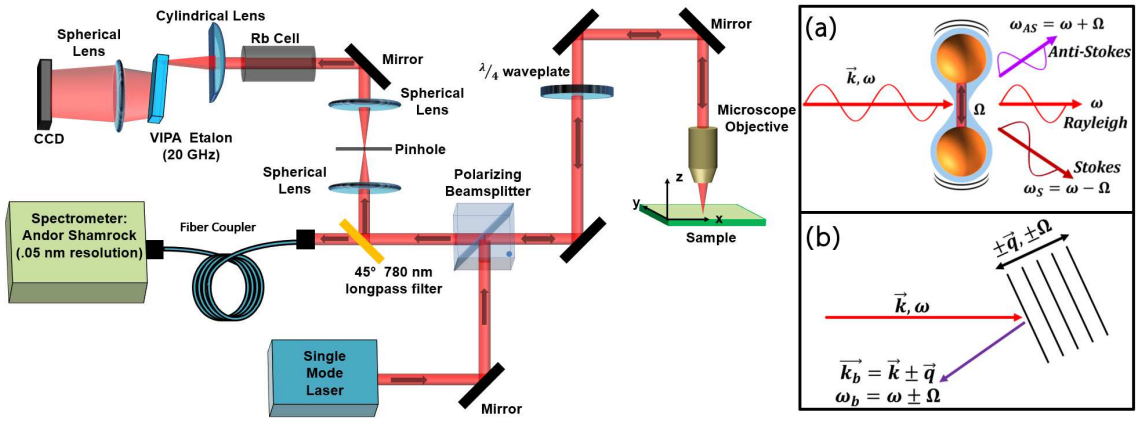

Figure 5.2: **Experimental Setup**[**107**] Light is passed through a polarizing beam cube into a microscope objective for imaging. Collected signal is split into two channels for Brillouin and Raman signal collection using a 45° long-pass filter. Raman spectra are collected using a conventional dispersive spec-trometer, while the Brillouin spectrometer consists of a home-built VIPA etalon system. **(Inset)(a)** Schematic Diagram of the Raman scattering process. A photon transfers a portion of its momentum to a vibrational state of a molecule. Typically, spontaneous Raman anti-Stokes radiation is not observed. **(b)** Schematic Diagram of Brillouin scattering. The incident light interacts with the acoustic field of the material. The magnitude of the frequency shift is dependent upon the direction of light scattered by the acoustic wave.

Raman frequency shifts are extremely large in comparison. While the application of molecular and atomic gas cells as notch filters is not new and has been used to great effect, they do present their own unique challenges [116, 38, 40, 74].

Just as with Brillouin spectroscopy in general, the specifications of the pump laser are of the utmost importance when using atomic vapor cells like Rubidium (Rb). At 80° C the Rb cell provides an absorption bandwidth of only around 500 MHz at best. Since it is fairly easy to saturate the transition of the vapor, long cells are needed to provide sufficient absorption of the pump laser when probing highly reflective or scattering materials. Given a total path length of 30 cm, we estimate the optical depth to be approximately 600 which provides it an extinction ratio of approximately -260 dB. The windows of the cell are anti-reflective coated for 780 nm to minimize optical losses. The laser itself is tuned to be resonant with the F=3 sublevel of the $5^2S_{1/2}$ ground state to the $5^2P_{1/2}$ excited state transition of ^{85}Rb. By choosing this particular transition, it places a 3 GHz blue detuned absorption band from the F=2 ground state of ^{85}Rb as well as a 1.3 GHz red detuned and 5.4 GHz blue detuned absorption from the hyperfine structure of ^{87}Rb.

The Rb absorption lines for the D_2 transition are depicted in Fig. 5.3 from a natural abundance sample of Rb (72.17% ^{85}Rb, 27.83% ^{87}Rb). In this case, the linewidth of the absorption peaks is broadened by the overall power of the laser as the actual linewidths are on the order of 10 MHz. As illustrated in the figure, the overall absorption of the ^{87}Rb peaks is lower than the ^{85}Rb peaks, but that has more to do with the larger population of ^{85}Rb in the sample rather than strength of the absorption. We can however, compare the relative absorption strength for the peaks of a given isotope. In both cases, there is stronger absorption along the upper hyperfine ground state level ($F = 3$ and $F = 2$ for ^{85}Rb and ^{87}Rb, respectively) to the $5^2P_{3/2}$ excited state. The overall absorption (optical depth) can be controlled for a

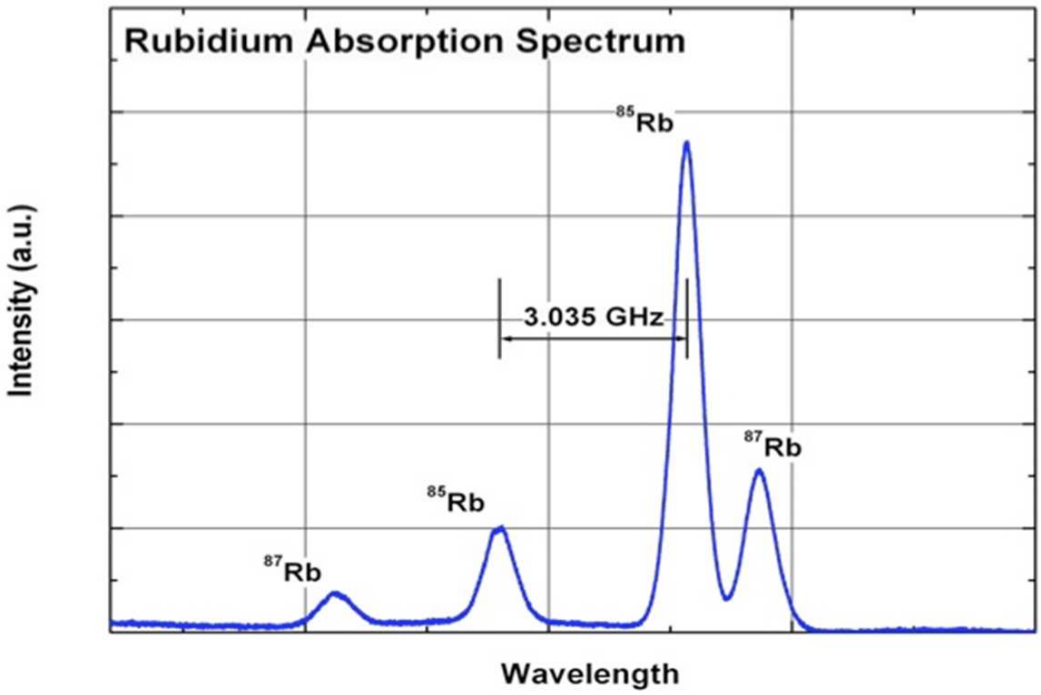

Figure 5.3: **Absorption Lines of Natural Abundance Rb** The spectrum was acquired by sweeping a the frequency of a laser across the transitions and measuring its relative absorption.

Figure 5.4: **Cell & Housing for Rb Filtering Cell** Design and image of actual Rb filtering cell. The middle section of the cell was kept unheated so that the Rb would condense on that region instead of the optical windows.

given sample of Rb simply by changing the temperature. The temperature increases the overall Rb vapor pressure, i.e. the atomic density, which basically means the overall population of atoms increased and can therefore absorb more light before saturating.

Fig.5.4 shows the The actual design of the Rb cell. Instead of going with a natural abundance Rb cell, we chose a quartz cell 30 cm long with a diamter of 2.54 cm filled with the single isotope ^{85}Rb. This removed the two extra sborption bands from ^{87}Rb which could potentially absorb an anti-Stoke or Stokes shifted Brillouin peak. The housing was constructed using aluminum chosen not only for its sturdiness but also its high thermal conductivity. Thus, the cell offers serves both as a robust shell to protect the cell from breaking and an oven to heat the cell evenly. The actual heating mechanism is heat tape wrapped around the outside of the aluminum housing powered by a VARIAC with alumnum foil further wrapped around the heat tape to help insulate and spread the heat. The temperature of the cell can be monitored via thermocouples attached at either end of the housing. During operation, the cell is kept at $\sim 80^\circ$ C giving a density of approximately 1.5×10^{12} cm^{-3}.

When compared to molecular vapors, some, like molecular iodine, may offer higher rates of absorption due to the band structures of the molecules, but these

also typically have a larger number of transitions that are detuned by a few GHz and therefore can absorb a portion of the Brillouin shifted signal[69]. If possible, it is best to use a single atomic isotope with a strong transition to reduce the number of detuned absorption bands, though this does limit the options for wavelengths available.

The microscope is designed to collect the backscattered emission along the beam-path, and uses a polarizing beam cube and a $\lambda/4$ waveplate to separate the backscattered emission from the pump laser. The laser light is emitted with a vertical polarization and passed through a 4-pass Bragg grating filtering system to remove the amplified spontaneous emission (ASE) as the ASE adds noise to measurements. The beam is then incident on a polarizing beam cube which reflects and couples it into a $\lambda/4$ waveplate. The now circularly polarized light is focused by a microscope objective onto the sample. The same microscope objective then collects the backscattered light which should now have the opposite circular polarization.

Next, the backscattered light passes back through the $\lambda/4$ waveplate, changing the polarization to horizontal which allows the light to pass through the polarizing beam-splitter and couple out to the spectrometers. The backscattered light is then split spectrally by a 45° long-pass filter (Semrock RazorEdge, Part No. LPD02-785RU-25), decoupling the Raman signal and passing it into a fiber coupled spectrometer (Shamrock 303i with attached iDus 401 CCD, Andor Inc.) while the elastic and Brillouin components of the spectra are reflected, focused into a 25 micron confocal pinhole, and are then sent into a 30 cm long Rb cell acting as a notch filter. The cell is heated to 80° C giving a vapor density of $\sim 2 \times 10^{12}$ cm^{-3} and optical depth of $\sim$600. With the elastic scattering suppressed by the Rb cell, the light is passed into a VIPA with a free spectral range (FSR) of 20.4 GHz, which images the Brillouin spectrum onto a CCD.

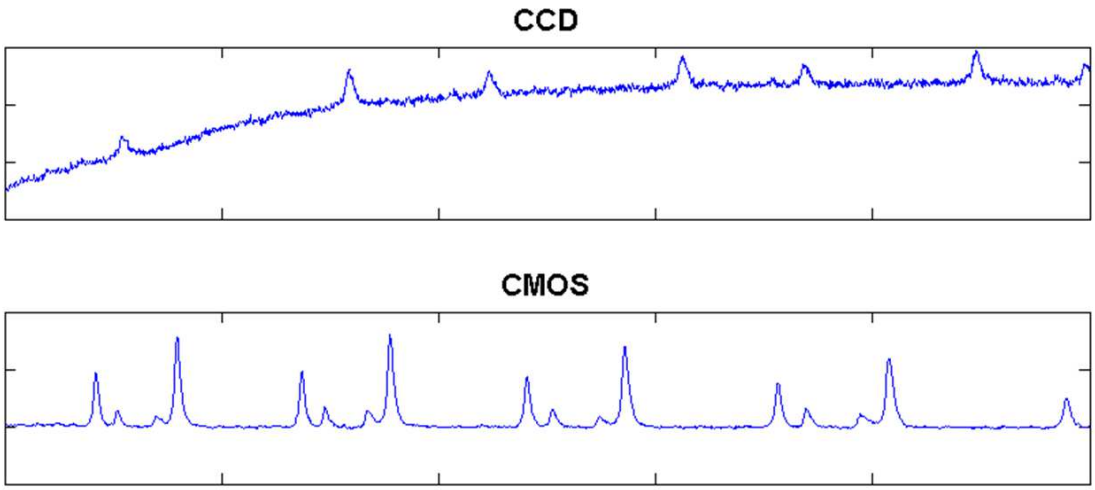

Figure 5.5: **Camera Comparison** Comparison of the Brillouin spectrum of acetone acquired with the CCD and the CMOS. Near the end of its lifetime, the CCD developed a rising dark current across its display which limited the achievable contrast.

For initial experiments the Brillouin spectra were acquired using a G2-8300 CCD from Moravian Instruments. While this camera possessed the sensitivity to resolve the weak Brillouin signals, it was originally designed for use in observational astronomy where short exposures and quick image retrieval times are not necessary. These shortcomings in conjunction with an inopportune camera failure where the CCD readout noise became greatly enhanced, spurred us to seek a more ideal alternative. We replaced the CCD with a CMOS camera (Neo Andor). This camera allows faster and more sensitive imaging with exposure times as low as 1 μs and extremely low dark current (0.007 e^- per pixel). This dark current is achievable mainly due to the fact that the camera can be cooled to -40° C. Given its fast acquistion speed/download speed in conjunction with its high sensitivity makes this camera ideal for raster scan microscopic imaging.

One major concern for the microscope is the frequency stability of the laser. Not

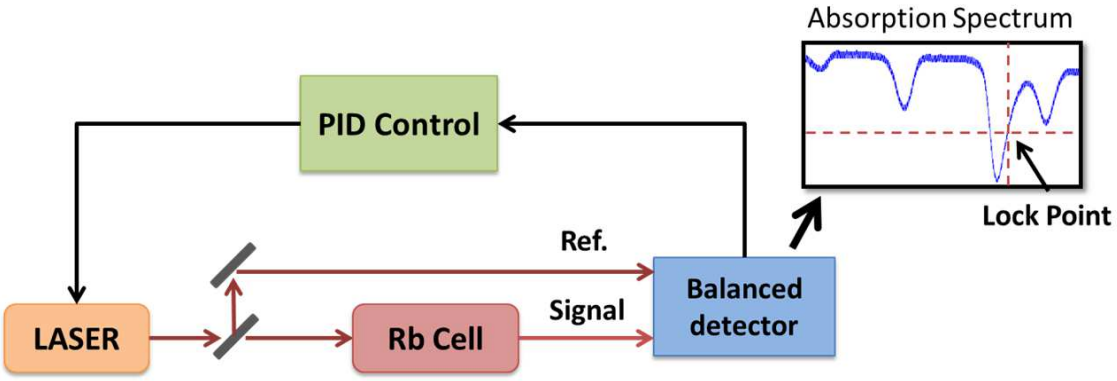

Figure 5.6: **Block Diagram of Feedback Loop for Laser Stabilization** A reference cell of Rb was used to monitor the frequency of the light relative to a Rb absorption line so that a control circuit could automatically compensate for any laser drift.

only is it necessary for the laser to maintain resonance with the Rb cell to filter out the elastically scattered light, but any shifts in the light during the course of a scan, can ruin the fidelity of the data. To avoid such issues, a simple electronic feedback loop and circuit were devised to lock the laser to one of the Rb sublevels. A block diagram depicting the feedback loop is shown in Fig. 5.6. To lock the laser to the Rb absorption line, the frequency of the laser is modulated using a function generator. A sawtooth waveform is input into the piezoelectric transducer (PZT) input of the laser causing the laser frequency to oscillate with an amplitude of several GHz. Then, a small portion of the overall laser power is used to measure the Rb absorption of the laser. This is accomplished by splitting several microwatts of the beam into two beams: one is passed through a Rb cell at room temperature to measure the Rb absorption while the other is kept as a reference. Both beams are then coupled into a balanced detector (Nirvana 2007, Newport Corp.) where the reference beam is subtracted from the Rb absorption beam thereby effectively removing laser power fluctuation. The Rb absorption spectra shown in both Fig. 5.5 and the inset of Fig.

5.6 were both acquired via this method. The laser frequency is then shifted such that it sits on resonance with one of the absorption lines when the PZT modulation is turned off. While the laser should be put on resonance, for our locking scheme, it should not be placed at the trough of the absorption line, the point of maximum absorption. Instead, it should be slightly detuned from the trough such that laser frequency is sitting on the downslope of the absorption line(inset of Fig. 5.6), which creates a nice voltage gradient that locking circuit use to provide feedback.

The locking circuit itself was designed and built as a proportionalintegralderivative (PID) controller (see Figs.5.7 for the schematic). Essentially, the circuit works by sending a voltage in to the laser's PZT if it senses the laser drifting from its set point. So, if we consider the setpoint (the desired laser frequency) to be zero volts, then any drift off of that setpoint is going to be some positive or negative nonzero voltage value. We chose the setpoint to be on one of the slopes of the Rb absorption line so that if the value becomes positive or negative, we know in which direction the laser frequency is drifting (see inset Fig. 5.6). For instance, if the PID circuit sees a positive (negative) voltage from the detector, it will send a negative (positive) voltage to the PZT to compensate for the drift. The proportional is the main portion of the circuit that accomplishes this and responds essentially cutaneously to the drift with a mirrored response. The integrator exists to compensate for very slow longterm drifts or offsets as its gain slowly builds up over time. The differentiator essentially acts as dampening component, ensuring the proportional does not react too quickly an over-correct. In general, the gain for each section of the controller needs to be set so that the net gain for the whole feedback circuit is one. If the gain is above one, it will lead to oscillation and eventual run off where the circuit comes out of lock. Furthermore, if total gain of the feedback loop is below one, the laser will not lock to a given frequency and will still be prone to drifting. An image of the

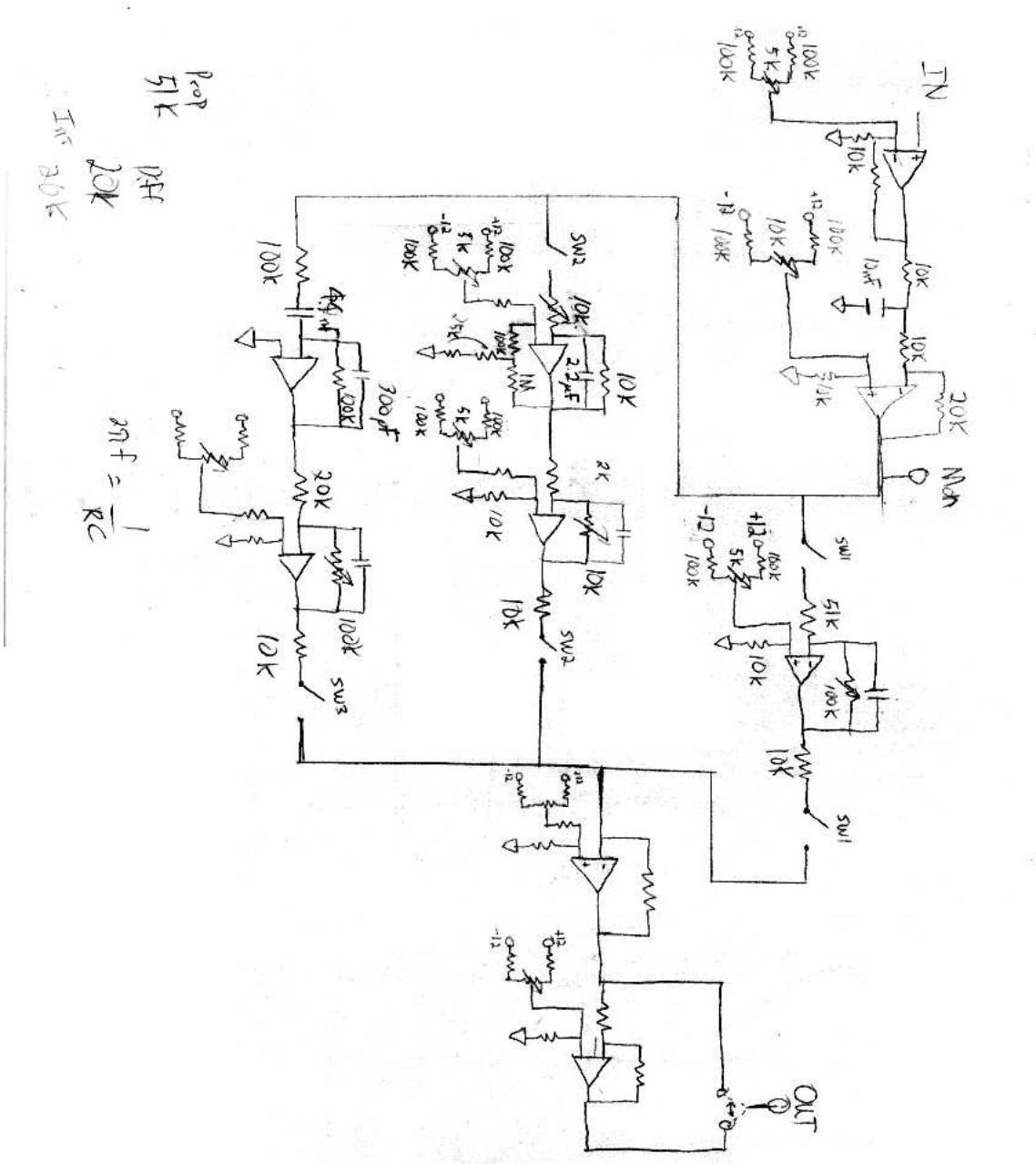

Figure 5.7: **Schematic of Locking Circuit** The circuit follows a typical proportional-integral-derivative design, though special care needed to be taken with the frequency response of the circuit as any frequencies above 10 KHz would cause issues in the feedback loop due to the laser's PZT frequency resonance at 10 KHz.

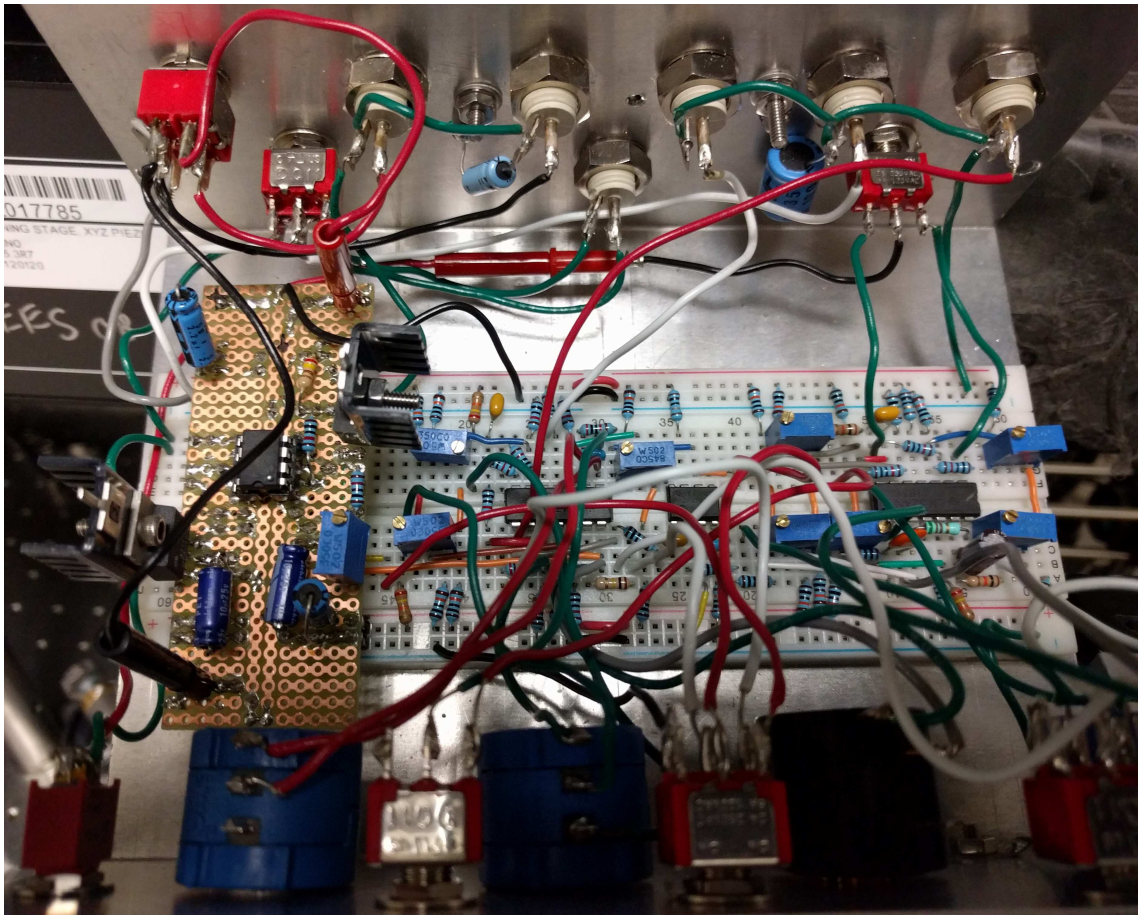

Figure 5.8: **Actual Image of Completed Locking Circuit** Special care had to be taken with the power supply for the circuit as fluctuations in the supply voltage will effect the quality of the lock. A voltage regulating was built and included in the circuit (left part of the image) to address this need.

finished circuit is shown in Fig. 5.8.

Given all the components necessary for a Dual Raman-Brillouin microscope capable of performing raster scan imaging, time-delayed scans, and temperature sweeps, control software needed to be created. To accomplish this we developed a labVIEW program that integrates every device in the microscope. This software provides complete control for each device from acquisition and wavelength range of the Raman spectometer, to positions of the translation stages and control of the laser as well as

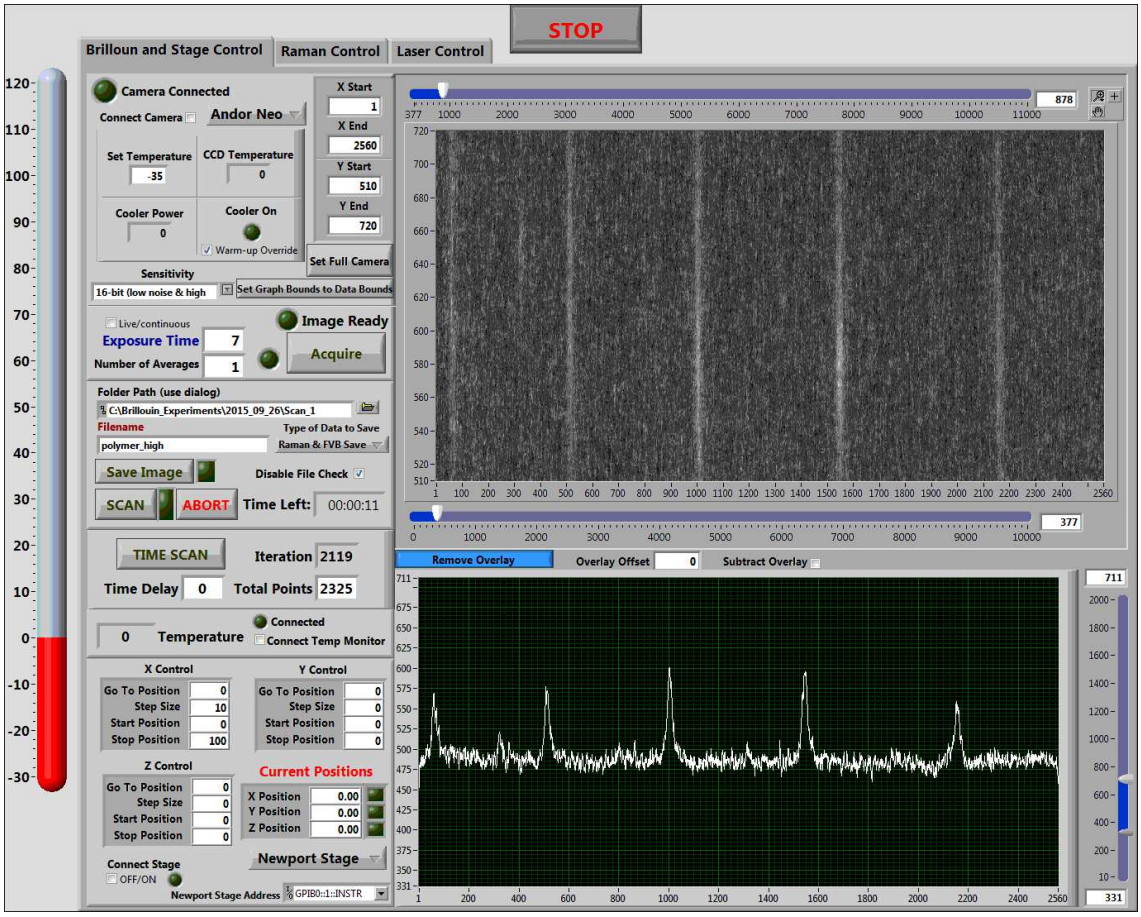

Figure 5.9: **Image of the LabVIEW Interface for the Microscope**. The displayed tab of the program is for the Brillouin spectrometer as well as the stage and file-saving controls.

the ability to manipulate and batch-save data. Beyond control capabilities, it is fully automated such that a full set of scans can be taken while raster scanning the stages by just inputting the initial parameters using the Raman and Brilluin spectrometers simultaneously. The front panel view of the Brillouin miscroscope portion of the software is shown in Fig. 5.9.

The program itself was designed to be as modular as possible (as can be seen in Fig. 5.10. Each device consists of a single subVI while the overall logic and decision-

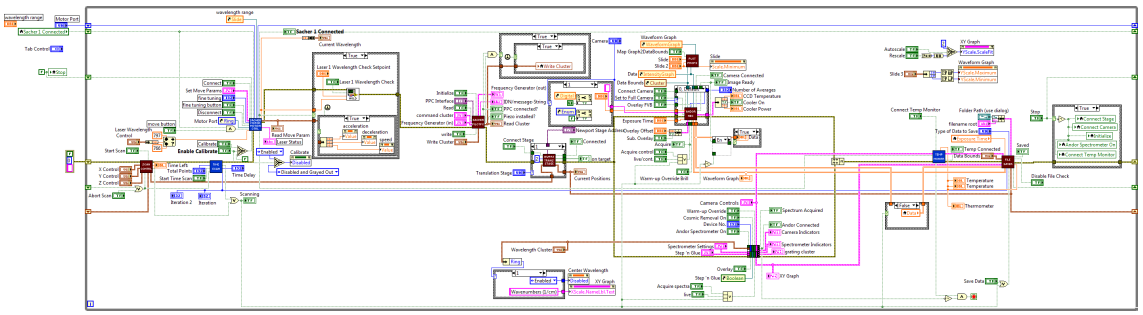

Figure 5.10: **Block Diagram of the LabVIEW Program for the Micrsoscope**. Each subVI represents a particular device controlled by the software or the logic controls for the scans and file-saving. Each subVI is developed such that it can quickly and easily be integrated into the system.

making of the program is contained in a segregate subVI. The subVI of each device simply allows access to the device's settings and extraction of the necessary data. In this way, a given component can be replaced easily with little to no changes necessary for the rest of the program. Furthermore, additional equipment is added fairly simply without effecting the functionality of the rest of the software. This has become a very useful feature as various studies from temperature scans to pressure studies have been of interest.

The sample itself is placed upon a piezo scanning microscopy stage (PI GmbH; P-545.xC7 PInano) driven by two motorized actuators (TRB Newport; Model No. TRB12PP). Again, both of these are controlled by the LabVIEW program and both stages can be used in conjunction with eachother to achieve high resolution scans through the piezo stage and large area scans via the motorized actuators.

To validate the imaging capability of the microscope, a sample was constructed using two materials with different mechanical and chemical properties. Cyclohexane and poly(ethylene glycol) diacrylate (PEGDA) hydrogel were selected as a model case, and the hydrogel was cured in a "T"-shaped mold to provide spatial contrast.

The body of the T-shaped structure was created using PEGDA of molecular weight = 35 kDa. The T-shaped structure was then placed into a solution of cyclohexane, which provided contrast for the image. The cyclohexane and hydrogel were held in place by sandwiching two glass slides around an aluminum reservoir, creating a closed system sealed from the external environment. The cyclohexane and aqueous components of the hydrogel were kept separate due to strong hydrophobic/hydrophilic interactions.

Cyclohexane is a simple nonpolar molecule with at least one axis of symmetry in each conformation. PEGDA hydrogel, on the other hand, has a complex molecular structure composed of long cross-linked polymer chains which absorb large amounts of water. Because of their vastly differing structures, cyclohexane and PEGDA exhibit very different Raman spectra. Due to its inherent symmetry, cyclohexane is also quite Raman active, whereas PEGDA typically generates a much weaker Raman signal.

Cyclohexane and PEGDA were also chosen because of their very distinct mechanical properties. The velocity of sound in cyclohexane is approximately 1371 m/s, compared to about 1482 m/s in water [27]. Since water is the primary component of PEGDA by volume, it is expected that acoustic propagation velocities will be similar, and the measured Brillouin shift of the hydrogel will be larger. As a final consideration, cyclohexane was chosen for its immiscibility with water from the hydrogel construct, as well as its low reactivity to maintain the integrity of the gel.

The PEGDA hydrogel was created by dissolving single polymer chains in a photoinitiator solution at 0.25 mg/mL, and cross-linking until solid. The photoinitiator solution consisted of approximately 1% 2-hydroxy-1-[4-(2-hydroxyethoxy) phenyl]-2-methyl-1-propanone (I2959), a common photopolymerization agent, in purified water4. The PEGDA was cured under a UV lamp for several minutes, and then removed

from the mold before final immersion in cyclohexane.

After preparation, the sample was placed on the translation stage and raster scanned to create two dimensional Raman and Brillouin images. Scanning was performed in 500 micron increments using a 10×/0.25NA Olympus objective lens, creating an image of 34×34 pixels with dimensions of 17×17 mm. The scan was performed using exposures of 48s and 30s for each Raman and Brillouin spectrum, respectively. These exposure times were chosen to provide ample contrast (several orders of magnitude) without incurring a large time cost. The total scan time, limited by the Raman spectral acquisition, was 15 hours. The spot size of the beam was calculated to be 25 microns; however, sub-micron spatial resolution is possible by simply using a higher numerical aperture objective lens[6].

5.2 Analysis & Experimental Results

Acquisition and analysis of Raman spectra has been extensively discussed in the literature, borrowing from decades of innovation [18]. Brillouin spectroscopy has not yet enjoyed as widespread of an adoption, and therefore, there is a lack of spectrometers developed for this purpose. Because of this, a custom spectrometer is a necessity, and it is paramount to develop a robust method of analysis to obtain highly accurate measurements of the Brillouin shift[91, 70]. Due to the dispersive nature of the VIPA, Brillouin peak spacing on the camera is not linear with the shift frequency. To ensure precise measurements, we applied a nonlinear scaling algorithm to the Brillouin spectra in order to normalize the Brillouin shift across iterations of the FSR. The full width of each FSR was used to determine the scale.

Pictured in Fig. 5.12 is a vertically binned image of a Brillouin spectrum of acetone with much of the noise suppressed. Much like in a Fabry-Perot cavity, the Brillouin spectrum is repeated for every iteration of the FSR of the VIPA. The peaks

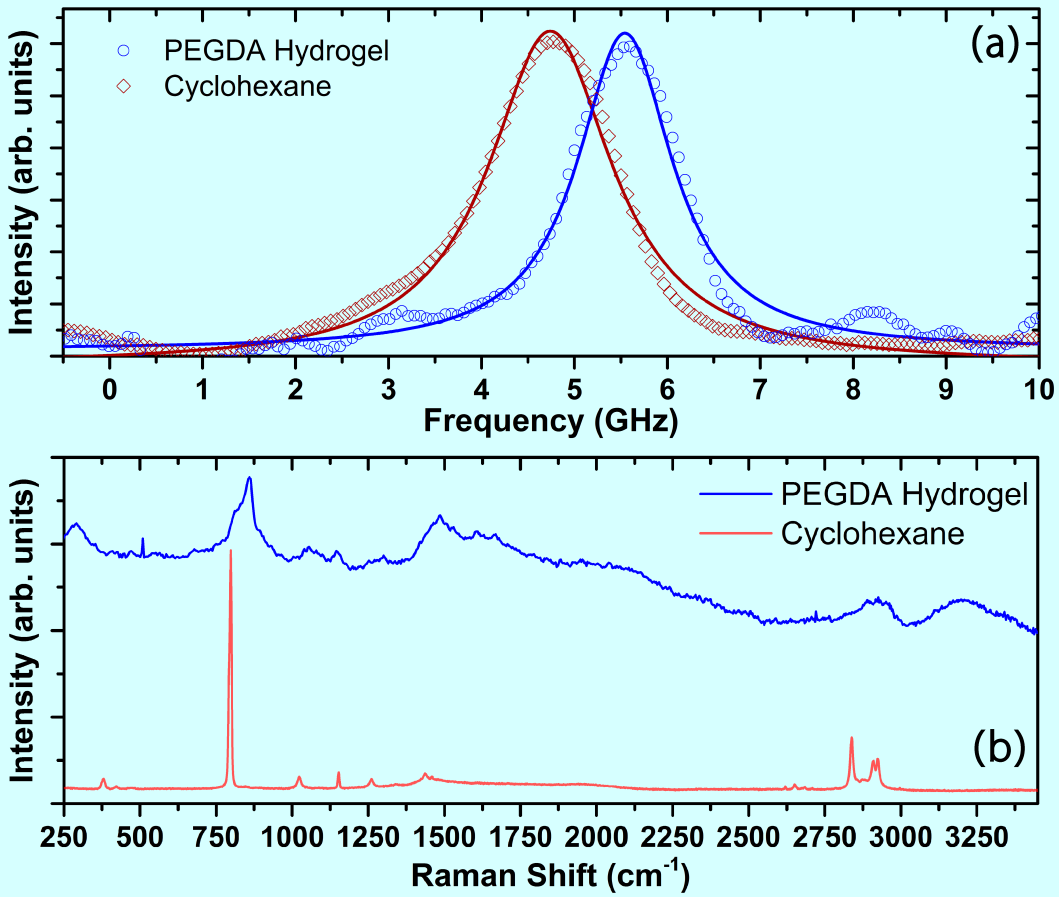

Figure 5.11: **Brillouin and Raman Spectra for PEGDA & Cyclohexane**[107] **(a)** Typical Brillouin spectra for the PEGDA hydrogel and cyclohexane, fitted with a Lorentzian distribution. Both spectra have been normalized for ease of viewing; in practice the cyclohexane Brillouin shift is nearly 10x more intense. **(b)** Typical Raman spectra for the PEGDA hydrogel and cyclohexane respectively. The scale of the PEGDA spectrum was magnified so that the spectral features would be more prominent.

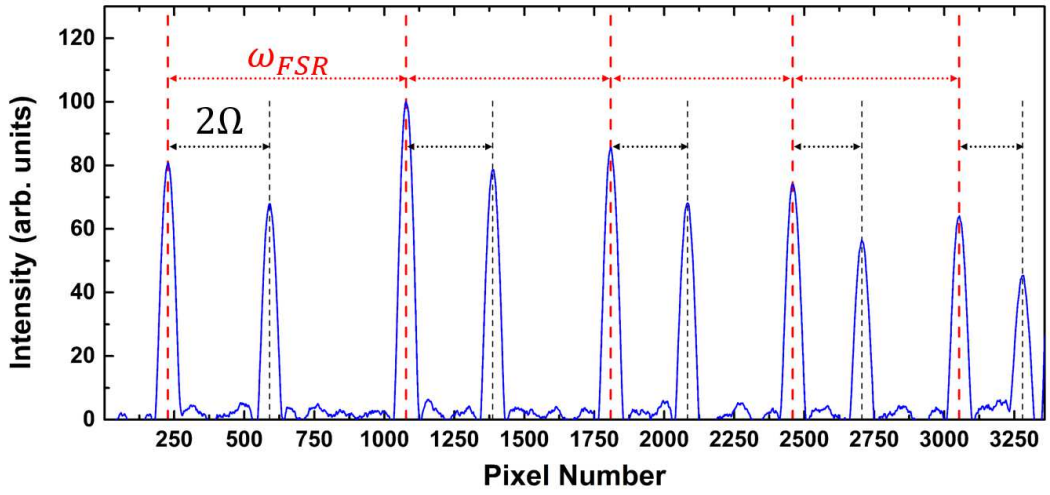

Figure 5.12: **Example of a Raw Brillouin Spectrum[107]** An example of a typical raw (unprocessed) Brillouin spectrum of acetone, where the Rayleigh light is completely suppressed by the Rb cell. Periodic pairs of Stokes and anti-Stokes Brillouin peaks are observed at each iteration of the FSR, ω_{FSR}=20.4 GHz, for the VIPA. The distance between each Stokes and Anti-Stokes peaks is 2Ω, twice the Brillouin shift.

seen in this case are all Brillouin lines, either Stokes or anti-Stokes, as the Rb cell completely suppresses the Rayleigh scattered light. Noticeably, distance between the peaks does not remain constant across each iteration of the spectrum due to the dispersion of the light from the VIPA. However, the iterative nature of the VIPA spectrum allows for a high-quality rescaling of the data, enabling very precise Brillouin measurements.

To accomplish this, we use the Stokes (or anti-Stokes) peak to set our scale, as we know that the FSR between each of the Stokes (or Anti-stokes) peaks should be the same. Intially, we took each of those peaks to be at a multiple of the FSR and performed a heuristic polynomial fit (usually 2nd or 3rd order), which provided a linear map of the frequency across our image. At this point, it becomes simply a matter of measuring the distance between our Stokes and anti-Stokes peaks for each

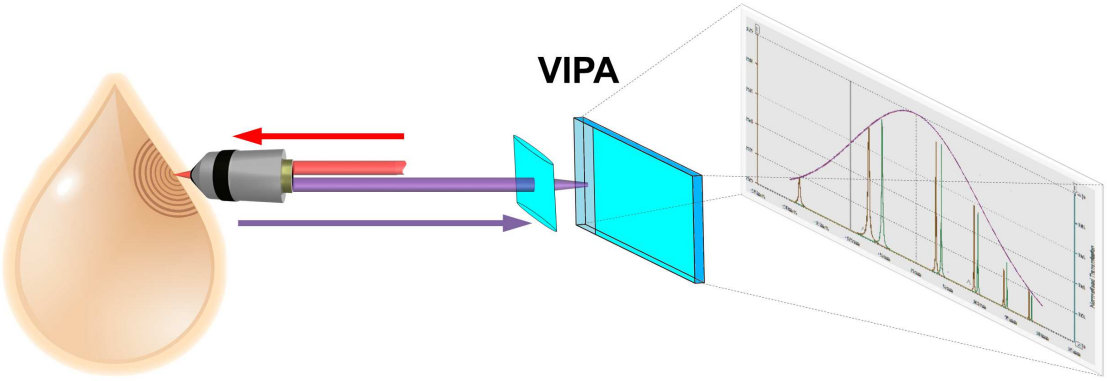

Figure 5.13: **Diagram of VIPA Output** The VIPA in some ways can be considered a transverse Fabry-Perot cavity as the light propagates along the length of the etalon. The intensity envelope is heavily determined by the focal length of the focusing lens into the VIPA.

of the spectra and converting each to a frequency difference. This frequency difference is twice the Brillouin shift, 2Ω, so by fitting multiple iterations of the spectrum we can accurately measure the Brillouin shift. In the case of the Brillouin spectrum of acetone depicted in Fig. 5.12, this approach gives a measured Brillouin shift of 4.06 ± 0.05 GHz which is within 0.6% of the expected value of 4.039 GHz calculated from the average index of refraction and the known speed of sound in acetone [84, 1]. While this approach for mapping the pixels to frequency via a heurestic polymonial fit, we wanted to lower our fitting uncertainty as we were seeing some measurement differences when the laser was locked to a slightly different portion of the absorption line.

To accomplish a better fitting, we went back to the dispersion relations of the VIPA to fit the data to the actual geometry of the system[114]. In the case of the VIPA, the intensity distribution function is:

$$I_{out}(x_F, \lambda) \propto \frac{1}{(1-Rr)^2 + (Rr)\sin^2\left(\frac{k\Delta}{2}\right)} \times \exp\left(-\frac{2f^2 x_F^2}{F^2 W^2}\right) \tag{5.1}$$

where $\Delta = 2tn_r\cos(\theta_{in}) - [(2t\tan(\theta_{in})\cos(\theta_i)\,x_F)/F] - [(t\cos(\theta_{in})\,x_F^2)/(n_r F^2)]$, x_F is the lateral displacement across the screen, t is the thickness of the VIPA, R and r are the reflectivities of VIPA for the front and back surfaces respectively, F is the focal length of the output lens, n_r is the index of refraction of the VIPA, k is the wavenumber of the incident light, Θ_i is the angle of the input laser relative to the normal of the VIPA, and $n_r\sin(\theta_{in}) = \sin(\theta_i)$. This produces a dispersion pattern similar to what is depicted in Figs. 5.13 & 5.12.

Using this approach is incredibly convenient as most of these parameters are easily known from the experimental setup, which helps limit the possible parameter space and lowers the chances of getting a bad fit. For the actual fitting we don't need the full intensity distribution function. In fact, the term $\left[(1-Rr)^2 + (Rr)\sin^2\left(\frac{k\Delta}{2}\right)\right]^{-1}$ gives the actual intensity peaks at the correct spacing between each iteration of the FSR. Furthermore, we really only need to consider when this intensity peaks which happens whenever $\sin\left(\frac{k\Delta}{2}\right) = 0$, i.e. $k\Delta = 2m\pi$. This gives us the phase matching condition:

$$k\left[2tn_r\cos(\theta_{in}) - (2t\tan(\theta_{in})\cos(\theta_i)\,x_F)/F - \left(t\cos(\theta_{in})\,x_F^2\right)/\left(n_r F^2\right)\right] = 2m\pi \tag{5.2}$$

Using this equation, we can derive an expression for the wavelength difference of two different lateral positions in a given FSR of the VIPA:

$$\Delta\lambda = -\lambda_0 \left[\frac{\tan(\theta_{in})\cos(\theta_i)}{n_r \cos(\theta_{in})} \left(\frac{x_F}{F}\right) + \frac{1}{2n_r^2}\left(\frac{x_F}{F}\right)^2 \right] \tag{5.3}$$

where $m\lambda_0 = 2tn_r \cos(\theta_{in})$, λ_0 is the pump wavelength, and m is the diffraction order. We this relation, we have a direct way of mapping the pixel number to the frequency shift of fitting the Brillouin peaks. Using this approach, we fit the parameters m, and θ_i. Our metric uses three different types of measurements across the 4 multiple FSRs in each Brillouin exposure. The three different measurements are the frequency between the each Stokes and and anti-Stokes peak, the frequency difference between each Stokes peak, and the frequency difference between each anti-Stokes peak. Each of these measurements should be uniform across all the FSRs, so we minimize the standard deviation, which allows us to converge on a best fit. This type of fitting has achieved frequency mappings with standard deviations of 2 MHz. It should be noted that the diffraction order is approximately $m \approx 18636$ given that we have 5 mm thick VIPA, $n_r = 1.4678$, and $\lambda_0 = 780.24$ nm.

The Brillouin spectra of the PEGDA/cyclohexane sample was analyzed only using the heuristic polynomial fit as extreme accuracy was not needed for this experimental demonstration. The major difference is that only the Stokes peaks for both cyclohexane and PEGDA were observed since Rb, due to its ground state splitting, has an absorption line matching the detuning of the Anti-stokes Brillouin shift. Instead, a Brillouin spectrum of acetone was used to set the frequency scale, as the location of zero detuning for each iteration of the FSR should be the same between samples.

Representative Brillouin spectra for both cyclohexane and PEGDA are depicted in Fig. 5.11a. Our measured Brillouin shift for cyclohexane is 4.584.01 GHz whereas the expected value is 4.576 GHz based on precision measurements of the speed of

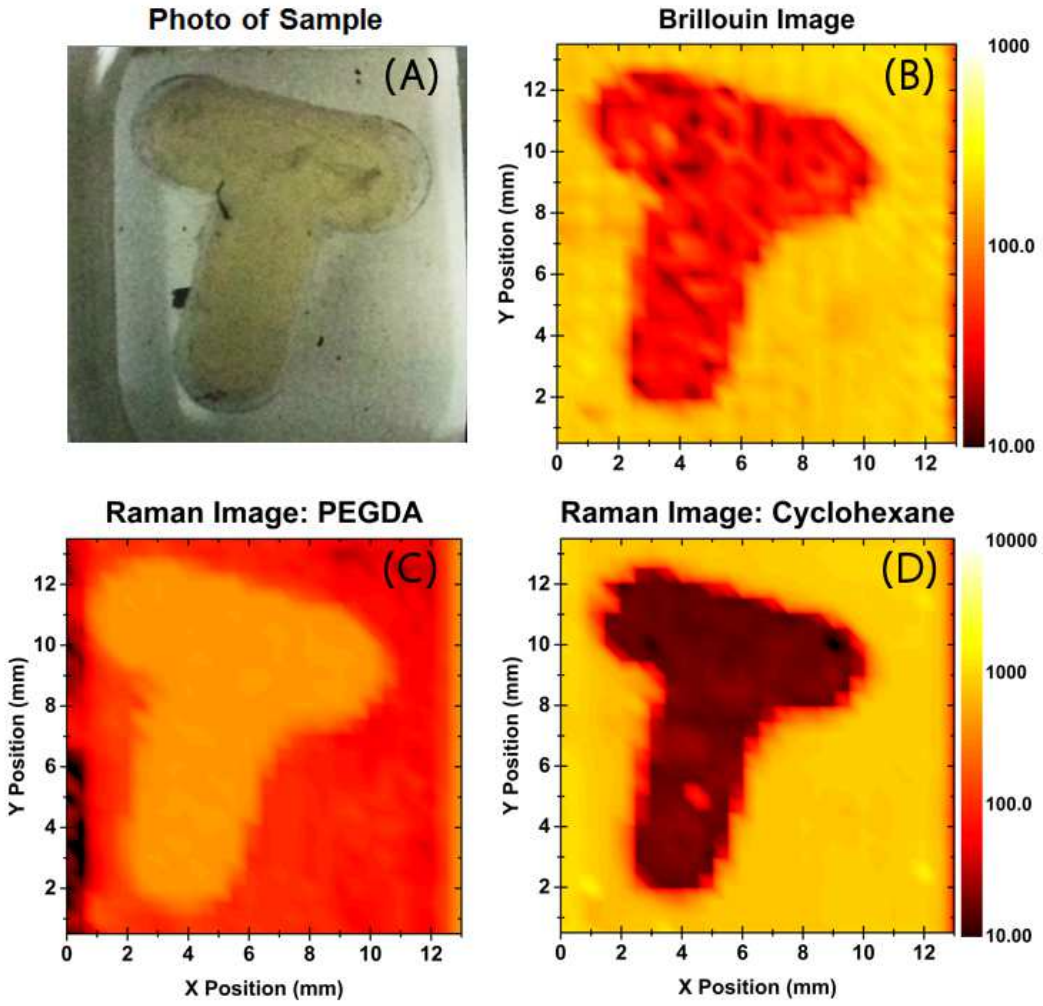

Figure 5.14: **Generated Images of the Sample[107]** **(A)** Normal photo. **(B)** Brillouin image using the intensity of the cyclohexane peak at 4.58 GHz as contrast. **(C)** Raman image using the normalized ratio between peaks at ∼1400 cm^{-1} and ∼2800 cm^{-1}. **(D)** Raman image using the cyclohexane peak near 800 cm^{-1} as contrast.

sound and index of refraction at 298.15 K[65]. While our sample was not stringently temperature controlled, which will slightly change the Brillouin shift, this still gives a difference between values of less than 0.2%. Similarly, for PEGDA the observed shift was 5.461±.03 GHz. Given that the hydrogel is mostly composed of water, this value is reasonable as the Brillouin shift for water is approximately 5.064 GHz [**?**, 31].

Similarly, Raman spectra of both PEGDA and cyclohexane are shown in Fig. 5.11b. In the Raman spectrum of cyclohexane, a strong line at ∼798 cm^{-1} is seen corresponding to alicyclic chain vibrations within the aliphatic ring structure. Likewise, a group of Raman peaks in the range of 2750-3000 cm^{-1} in cyclohexane correspond to CH_2 alkane vibrations. The CH_2 vibrations are also present in the PEGDA spectrum, but due to the hydrogels high water content, it is much less visible. The PEGDA hydrogel is expected to have a much weaker Raman spectrum, as both water and strongly polar carbonyl groups are not highly Raman active.

Finally, after acquiring the Raman and Brillouin spectra from each location, images were constructed as illustrated in Fig. 5.14. Contrast for each image was created using the intensity of a given peak in the Raman/Brillouin spectra. In the case of the Raman image of cyclohexane, the source of contrast was the distinctive alicyclic peak near 800 cm^{-1}, as this peak is weak in PEGDA. To construct the Raman image of PEGDA, a ratio of peak heights at ∼1400 cm^{-1} and ∼2800 cm^{-1} was used as contrast. For the Brillouin image, we measured the relative intensity of the cyclohexane Stokes peak at 4.58 GHz since the Brillouin peak for the PEGDA hydrogel occurred at a substantially higher frequency. In all three cases a high-contrast image was produced, whose spatial accuracy can be confirmed when compared to a normal photo of the sample (Fig. 5.14).

5.3 Discussion

While the images and spectra above illustrate the capabilities of this instrument, better sensitivity and spectral resolution can be achieved through various improvements to the system. Replacing the ECDL with a 780 nm source produced through second harmonic generation of 1560 nm radiation would reduce the noise in the Brillouin spectra because the ECDL has the inherent disadvantage of background ASE. Further, using a single isotope of Rb for the absorption cell would reduce the number of detuned absorption bands, preventing unwanted absorption of the Brillouin shifts when they match a band. Lastly, utilizing a VIPA with a larger FSR would allow for characterization of more rigid materials, as their Brillouin shifts can exceed 15 GHz. Overall, these changes would greatly enhance the effectiveness of the instrument.

We are currently in the process of upgrading the pump laser for the system to a frequency doubled source. The new laser is comprised of an extremely narrow, stable seed source at ≈1560 nm (Pure Photonics, PPCL300), an amplifier for the 1560 nm seed (IPG photonics, EAR-5K-C-LP-SF), and a heated BBO crystal. The seed, tunable from 1558-1565 nm, injects 5 mW of power into the amplifier which increases the power up to 5 W. This 1560 nm light is then focused into the BBO crystal (heated to ≈75° using a 20 cm focusing lens. This produces 250 mW of frequency doubled narrow-band light at 780.24 nm. Not only are we now getting double the laser power, but we have lowered the background ASE that was ever-present using the ECDL. This opens up the possibilities for using the system to probe higher scattering media where removing the elastically scattered light was extremely challenging.

The real significance of this dual microscopy system will be realized when it is applied to characterization of biological systems or novel materials. Its ability to

simultaneously monitor changes in a systems mechanical and chemical properties makes it an unprecedented diagnostic tool. In this capacity, it is uniquely situated to become a valuable aid for researchers.

In summary, we have demonstrated the effectiveness and potential for a dual Raman-Brillouin microscopy system in producing highly accurate measurements and providing complementary chemical and mechanical information. Simultaneous acquisition of Brillouin and Raman spectra from the same focal region allows for an expanded level of sample characterization without sacrificing quality of signal from either modality. Moreover, there is no added time cost for simultaneous acquisition of both spectra, as exposure times for Raman and Brillouin are comparable. For these reasons, this system should find widespread adoption as a very powerful tool throughout science and engineering.

6. CONCLUSION

Each of these chapters highlights a significant step forward in their respective field of study. Coherence processes are in large part becoming the key for advanced light generation techniques. In large part this is mainly due to the increased level of control we now enjoy due to the current level of technology. The work described in this manuscript is the direct result of these advancements and aims to aid in further innovations in science and engineering. Each of these coherent processes not only introduces the the potential for new exciting applications, but also presents unique insights into the fundamental physical processes. This work does not complete any of these areas of study, but rather is the first stepping stone for future fruitful inquiry.

REFERENCES

[1] J. Acosta, A. Arce, E. Rodil, and A. Soto. Densities, speeds of sound, refractive indices, and the corresponding changes of mixing at 25° C and atmospheric pressure for systems composed by ethyl acetate, hexane, and acetone. *Journal of Chemical and Engineering Data*, 46(5):1176–1180, 2001.

[2] G. S. Agarwal and R. W. Boyd. Quantum theory of Rabi sideband generation by forward four-wave mixing. *Physical Review A*, 38(8):4019–4027, 1988.

[3] S. Agrup and M. Aldén. Two-photon laser-induced fluorescence and stimulated emission measurements from oxygen atoms in a hydrogen/oxygen flame with picosecond resolution. *Optics Communications*, 113(1-3):315–323, 1994.

[4] M. Aldén, U. Westblom, and J. E. Goldsmith. Two-photon-excited stimulated emission from atomic oxygen in flames and cold gases. *Optics Letters*, 14(6):305–307, 1989.

[5] L. Allen and J. H. Eberly. *Optical Resonance and Two-level Atoms*. Courier Corporation, North Chelmsford, MA USA, 1975.

[6] G. Antonacci, M. R. Foreman, C. Paterson, and P. Török. Spectral broadening in Brillouin imaging. *Applied Physics Letters*, 103(22), 2013.

[7] K. A. Antonio and Z. D. Schultz. Advances in biomedical Raman microscopy. *Analytical Chemistry*, 86(1):30–46, 2014.

[8] D. Attwood. *Soft X-Rays and Extreme Ultraviolet Radiation: Principles and Applications*. Cambridge University Press, Cambridge, UK, 2007.

[9] I. Barman, G. P. Singh, R. R. Dasari, and M. S. Feld. Turbidity-corrected Raman spectroscopy for blood analyte detection. *Analytical Chemistry*, 81(11):4233–4240, 2009.

[10] S. E. Bisson, J. E. Goldsmith, and M. G. Mitchell. Narrow-band, narrow-field-of-view Raman lidar with combined day and night capability for tropospheric water-vapor profile measurements. *Applied Optics*, 38(9):1841–1849, 1999.

[11] R. W. Boyd. *Nonlinear Optics*. Academic Press, Cambridge, MA, USA, 2008.

[12] R. W. Boyd, M. G. Raymer, P. Narum, and D. J. Harter. Four-wave parametric interactions in a strongly driven two-level system. *Physical Review A*, 24(1), 1981.

[13] J. H. Brownell, X. Lu, and S. R. Hartmann. Yoked superfluorescence. *Physical Review Letters*, 75(18):3265–3268, 1995.

[14] D. C. Burnham and R. Y. Chiao. Coherent resonance fluorescence excited by short light pulses. *Physical Review*, 188(2):667–675, 1969.

[15] R. L. Carman, R. Y. Chiao, and P. L. Kelley. Observation of degenerate stimulated four-photon interaction and four-wave parametric amplification. *Physical Review Letters*, 17(26):1281–1283, 1966.

[16] E. A. Chauchard and Y. H. Meyer. On the origin of the so called conical emission in laser pulse propagation in atomic vapor. *Optics Communications*, 52(2):141–144, 1984.

[17] R. Y. Chiao, C. H. Townes, and B. P. Stoicheff. Stimulated Brillouin scattering and coherent generation of intense hypersonic waves. *Physical Review Letters*, (21), 1964.

[18] N. Colthup. *Introduction to Infrared and Raman Spectroscopy.* Elsevier Science, Philadelphia, PA, USA, 2012.

[19] M. E. Crenshaw and C. D. Cantrell. Conical emission as a result of pulse breakup into solitary waves. *Physical Review A*, 39(1):126–148, 1989.

[20] R. H. Dicke. Coherence in spontaneous radiation processes. *Physical Review*, 93(1):99–110, 1954.

[21] A. Dogariu, J. B. Michael, M. O. Scully, and R. B. Miles. High-gain backward lasing in air. *Science*, 331(6016):442–5, 2011.

[22] M. S. Dresselhaus, A. Jorio, M. Hofmann, G. Dresselhaus, and R. Saito. Perspectives on carbon nanotubes and graphene Raman spectroscopy. *Nano Letters*, 10(3):751–758, 2010.

[23] M. J. Dyer and D. R. Crosley. Doppler-free laser-induced fluorescence of oxygen atoms in an atmospheric-pressure flame. *Optics Letters*, 14(1):12–14, 1989.

[24] G. Eckhardt, R. W. Hellwarth, F. J. McClung, S. E. Schwarz, D. Weiner, and E. J. Woodbury. Stimulated Raman scattering from organic liquids. *Physical Review Letters*, 9(11):455–457, 1962.

[25] R. A. Ganeev, M. Suzuki, M. Baba, H. Kuroda, and I. A. Kulagin. Third-harmonic generation in air by use of femtosecond radiation in tight-focusing conditions. *Applied Optics*, 45(4):748–755, 2006.

[26] I. Golub, G. Erez, and R. Shuker. Cherenkov emission due to laser-induced moving polarisation in sodium. *Journal of Physics B: Atomic and Molecular Physics*, 19:L115–L120, 1986.

[27] B. Gonzalez, I. Dominguez, E. J. Gonzalez, and A. Dominguez. Density, speed of sound, and refractive index of the binary systems cyclohexane (1) or methyl-

cyclohexane (1) or cyclo-octane (1) with benzene (2), toluene (2), and ethylbenzene (2) at two temperatures. *Journal of Chemical and Engineering Data*, 55(1):1003–1011, 2010.

[28] J. P. Gordon, H. J. Zeiger, and C. H. Townes. The maser-new type of microwave amplifier, frequency standard, and spectrometer. *Physical Review*, 99(4):1264–1274, 1955.

[29] D. Grischkowsky. Self-focusing of light by potassium vapor. *Physical Review Letters*, 24(16), 1970.

[30] L. I. Gudzenko and L. A. Shelepin. Negative absorption in a nonequilibrium hydrogen plasma. *Soviet Journal of Experimental and Theoretical Physics*, 18(4):998–1000, 1964.

[31] G. M. Hale and M. R. Querry. Optical constants of water in the 200-nm to 200-μm wavelength region. *Applied Optics*, 12(3):555–563, 1973.

[32] R. Harley, D. James, A. Miller, and J. W. White. Phonons and the elastic moduli of collagen and muscle. *Nature*, 267(5608):285–287, 1977.

[33] S. E. Harris and R. B. Miles. Proposed third-harmonic generation in phase-matched metal vapors. *Applied Physics Letters*, 19(10):385–387, 1971.

[34] D. J. Harter, P. Narum, M. G. Raymer, and R. W. Boyd. Four-wave parametric amplification of Rabi sidebands in sodium. *Physical Review Letters*, 46(18), 1981.

[35] D. Heiman, R. W. Hellwarth, M. D. Levenson, and G. Martin. Raman-induced Kerr effect. *Physical Review Letters*, 36(4):189–192, 1976.

[36] R. Hellwarth. Theory of stimulated Raman scattering. *Physical Review*, 130(5):1850–1852, 1963.

[37] P. R. Hemmer, R. B. Miles, P. Polynkin, T. Siebert, A. V. Sokolov, P. Sprangle, and M. O. Scully. Standoff spectroscopy via remote generation of a backward-propagating laser beam. *Proceedings of the National Academy of Sciences*, 108(8):3130–4, 2011.

[38] P. J. Horoyski and M. L. W. Thewalt. Fourier transform Raman and Brillouin spectroscopy using atomic vapor filters. *Applied Spectroscopy*, 48(7):843–7, 1994.

[39] Y.-L. Huang and R. J. Gordon. The effect of amplified spontaneous emission on the measurement of the multiplet state distribution of ground state oxygen atoms. *The Journal of Chemical Physics*, 97(9):6363, 1992.

[40] R. Indralingam, J. B. Simeonsson, G. A. Petrucci, B. W. Smith, and J. D. Winefordner. Raman spectrometry with metal vapor filters. *Analytical Chemistry*, 64(8):964–7, 1992.

[41] F. E. Irons and N. J. Peacock. Experimental evidence for population inversion in C^{5+} in an expanding laser-produced plasma. *Journal of Physics B*, 7(9):1109–1112, 1974.

[42] W. Kaiser and C. Garrett. Two-photon excitation in CaF_2: Eu^{2+}. *Physical Review Letters*, 7(6):229–231, 1961.

[43] D. Kartashov, S. Aliauskas, G. Andriukaitis, A. Puglys, M. Shneider, A. M. Zheltikov, S. L. Chin, and A. Baltuka. Free-space nitrogen gas laser driven by a femtosecond filament. *Physical Review A*, 86(3):1–8, 2012.

[44] O. Katz, A. Natan, Y. Silberberg, and S. Rosenwaks. Standoff detection of trace amounts of solids by nonlinear Raman spectroscopy using shaped femtosecond pulses. *Applied Physics Letters*, 92(17):21–24, 2008.

[45] J. Kerr. XLIII. On rotation of the plane of polarization by reflection from the pole of a magnet. *Philosophical Magazine Series 5*, 3(19):321–343, 1877.

[46] J. Kerr. XXIV. On reflection of polarized light from the equatorial surface of a magnet. *Philosophical Magazine Series 5*, 5(30):161–177, 1878.

[47] D. S. Knight and W. B. White. Characterization of diamond films by Raman spectroscopy. *Journal of Materials Research*, 4(02):385–393, 2011.

[48] V. Kocharovsky, S. Cameron, K. Lehmann, R. Lucht, R. Miles, Y. Rostovtsev, W. Warren, G. R. Welch, and M. O. Scully. Gain-swept superradiance applied to the stand-off detection of trace impurities in the atmosphere. *Proceedings of the National Academy of Sciences*, 102(22):7806–11, 2005.

[49] N. M. Kroll. Excitation of hypersonic vibrations by means of photoelastic coupling of high-intensity light waves to elastic waves. *Journal of Applied Physics*, 36(1):34–43, 1965.

[50] A. Laurain, M. Scheller, and P. Polynkin. Low-threshold bidirectional air lasing. *Physical Review Letters*, 113(25):253901, 2014.

[51] M. LeBerre-Rousseau, E. Ressayre, and A. Tallet. Self-induced generation of an off-axis frequency shifted radiation from atoms. *Optics Communications*, 36(1):31–34, 1981.

[52] S. Lees, N. J. Tao, and S. M. Lindsay. Studies of compact hard tissues and collagen by means of Brillouin light scattering. *Connective Tissue Research*, 24(3-4):187–205, 2009.

[53] M. D. Levenson and N. Bloembergen. Dispersion of the nonlinear optical susceptibility tensor in centrosymmetric media. *Physical Review B*, 10(10):4447–4463, 1974.

[54] M. D. Levenson, C. Flytzanis, and N. Bloembergen. Interference of resonant and nonresonant three-wave mixing in diamond. *Physical Review B*, 6(10):3962–3965, 1972.

[55] H. Li, D. A. Harris, B. Xu, P. J. Wrzesinski, V. V. Lozovoy, and M. Dantus. Standoff and arms-length detection of chemicals with single-beam coherent anti-Stokes Raman scattering. *Applied Optics*, 48(4):B17–B22, 2009.

[56] J. Liu, J. Dai, S. L. Chin, and X.-C. Zhang. Broadband terahertz wave remote sensing using coherent manipulation of fluorescence from asymmetrically ionized gases. *Nature Photonics*, 4(9):627–631, 2010.

[57] Y. Liu, M. Durand, A. Houard, B. Forestier, A. Couairon, and A. Mysyrowicz. Efficient generation of third harmonic radiation in air filaments: A revisit. *Optics Communications*, 284(19):4706–4713, 2011.

[58] P. Longo, P. Schmitteckert, and K. Busch. Few-photon transport in low-dimensional systems: interaction-induced radiation trapping. *Physical Review Letters*, 104(2):23602, 2010.

[59] Q. Luo, W. Liu, and S. L. Chin. Lasing action in air induced by ultra-fast laser filamentation. *Applied Physics B*, 76(3):337–340, 2003.

[60] J. C. MacGillivray and M. S. Feld. Theory of superradiance in an extended, optically thick medium. *Physical Review A*, 14(3):1169–1189, 1976.

[61] M. Maier, W. Kaiser, and J. A. Giordmaine. Backward stimulated Raman scattering. *Physical Review*, 177(2):580–599, 1969.

[62] T. H. Maiman. Stimulated optical radiation in ruby. *Nature*, 187(4736):493–494, 1960.

[63] P. D. Maker and R. W. Terhune. Study of optical effects due to an induced polarization third order in the electric field strength. *Physical Review*, 137(3A), 1965.

[64] J. J. Maki, M. S. Malcuit, M. G. Raymer, R. W. Boyd, and P. D. Drummond. Influence of collisional dephasing processes on superfluorescence. *Physical Review A*, 40(9):5135–5142, 1989.

[65] E. Mascato, L. Mosteiro, M. M. Pineiro, J. Garcia, T. P. Iglesias, and J. L. Legido. Density, speed of sound and refractive index of (n-hexane + cyclohexane + 1-hexanol) at T= 298.15 K. *The Journal of Chemical Thermodynamics*, 33(9):1081–1096, 2001.

[66] P. Matousek, I. P. Clark, E. R. C. Draper, M. D. Morris, A. E. Goodship, N. Everall, M. Towrie, W. F. Finney, and A. W. Parker. Subsurface probing in diffusely scattering media using spatially offset Raman spectroscopy. *Applied Spectroscopy*, 59(4):393–400, 2005.

[67] D. Matthews, P. Hagelstein, M. Rosen, M. Eckart, N. Ceglio, A. Hazi, H. Medecki, B. MacGowan, J. Trebes, B. Whitten, E. Campbell, C. Hatcher, A. Hawryluk, R. Kauffman, L. Pleasance, G. Rambach, J. Scofield, G. Stone, and T. Weaver. Demonstration of a soft X-ray amplifier. *Physical Review Letters*, 54(2):110–113, 1985.

[68] G. McLaughlin, K. C. Doty, and I. K. Lednev. Raman spectroscopy of blood for species identification. *Analytical Chemistry*, 86(23):11628–11633, 2014.

[69] Z. Meng, A. J. Traverso, and V. V. Yakovlev. Background clean-up in Brillouin microspectroscopy of scattering medium. *Optics Express*, 22(5):5410–5, 2014.

[70] Z. Meng and V. V. Yakovlev. Optimizing signal collection efficiency of the VIPA-based Brillouin spectrometer. *Journal of Innovative Optical Health Sciences*, 8(4):1550021, 2015.

[71] R. Mock, B. Hillebrands, and R. Sandercock. Construction and performance of a Brillouin scattering set-up using a triple-pass tandem Fabry-Pérot interferometer. *Journal of Physics E*, 20:656–659, 2000.

[72] B. R. Mollow. Stimulated emission and absorption near resonance for driven systems. *Physical Review A*, 5(5):2217–2222, 1972.

[73] G. H. C. New and J. F. Ward. Optical third-harmonic generation in gases. *Physical Review Letters*, 19(10):556–559, 1967.

[74] H. Okajima and H. O. Hamaguchi. Fast low frequency (down to 10 cm^{-1}) multichannel Raman spectroscopy using an iodine vapor filter. *Applied Spectroscopy*, 63(8):958–960, 2009.

[75] E. Oliva, M. Fajardo, L. Li, M. Pittman, T. T. T. Le, J. Gautier, G. Lambert, P. Velarde, D. Ros, S. Sebban, and Ph. Zeitoun. A proposal for multi-tens of GW fully coherent femtosecond soft X-ray lasers. *Nature Photonics*, 6(11):764–767, 2012.

[76] F. Palombo, M. Madami, N. Stone, and D. Fioretto. Mechanical mapping with chemical specificity by confocal Brillouin and Raman microscopy. *Analyst*, pages 729–733, 2014.

[77] F. Palombo, C. P. Winlove, R. S. Edginton, E. Green, N. Stone, S. Caponi, M. Madami, and D. Fioretto. Biomechanics of fibrous proteins of the extracellular matrix studied by Brillouin scattering. *Journal of the Royal Society, Interface*, 11(101):20140739, 2014.

[78] E. Paradis, B. Barrett, A. Kumarakrishnan, R. Zhang, and G. Raithel. Observation of superfluorescent emissions from laser-cooled atoms. *Physical Review A*, 77(4):043419, 2008.

[79] G. I. Petrov, R. Arora, V. V. Yakovlev, X. Wang, A. V. Sokolov, and M. O. Scully. Comparison of coherent and spontaneous Raman microspectroscopies for noninvasive detection of single bacterial endospores. *Proceedings of the National Academy of Sciences*, 104(19):7776–7779, 2007.

[80] D V. Plutov and D. K. Killinger. Modeling of spectral emission-based lidar remote sensing. In *Proceedings of SPIE*, volume 7665, pages 1–9, 2010.

[81] T. Popmintchev, M.-C. Chen, D. Popmintchev, P. Arpin, S. Brown, S. Ališauskas, G. Andriukaitis, T. Balciunas, O. D. Mücke, A. Pugzlys, A. Baltuska, B. Shim, S. E. Schrauth, A. Gaeta, C. Hernández-García, L. Plaja, A. Becker, A. Jaron-Becker, M. M. Murnane, and H. C. Kapteyn. Bright coherent ultrahigh harmonics in the keV x-ray regime from mid-infrared femtosecond lasers. *Science*, 336(6086):1287–91, 2012.

[82] S. P. S. Porto and D. L. Wood. Ruby optical maser as a Raman source. *Journal of the Optical Society of America*, 52(3):251, 1962.

[83] J. F. Reintjes. *Nonlinear Optical Parametric Processes in Liquids and Gases*, volume 32. Academic Press, Cambridge, MA, USA, 1984.

[84] J. Rheims, J. Köser, and T. Wriedt. Refractive-index measurements in the near-IR using an Abbe refractometer. *Measurement Science and Technology*, 8(6):601–605, 1999.

[85] Ph. Rohwetter, J. Yu, G. Mejean, K. Stelmaszczyk, E. Salmon, J Kasparian, J.-P. Wolf, L. Woste, and L. Wo. Remote LIBS with ultrashort pulses: charac-

teristics in picosecond and femtosecond regimes. *Journal of Analytical Atomic Spectrometry*, 19(4):437–444, 2004.

[86] C. Roychoudhuri. Demonstrations using a Fabry-Pérot. I. Multiple-slit interference. *American Journal of Physics*, 43(12):1054, 1975.

[87] A. Rundquist, C. G. Durfee III, Z. Chang, C. Herne, S. Backus, and M. M. Murnane. Phase-matched generation of coherent soft X-rays. *Science*, 280(5368):1412–1415, 1998.

[88] R. Sánchez-González, R. Srinivasan, R. D. W. Bowersox, and S. W. North. Simultaneous velocity and temperature measurements in gaseous flow fields using the VENOM technique. *Optics Letters*, 36(2):196–8, 2011.

[89] G. Scarcelli, S. Kling, El. Quijano, R. Pineda, S. Marcos, and S. H. Yun. Brillouin microscopy of collagen crosslinking: noncontact depth-dependent analysis of corneal elastic modulus. *Investigative Ophthalmology and Visual Science*, 54(2):1418–1425, 2013.

[90] G. Scarcelli and S. H. Yun. Confocal Brillouin microscopy for three-dimensional mechanical imaging. *Nature Photonics*, 2(1):39–43, 2008.

[91] Giuliano Scarcelli and Seok Hyun Yun. Multistage VIPA etalons for high-extinction parallel Brillouin spectroscopy. *Optics Express*, 19(11):10913–10922, 2011.

[92] M. O. Scully, G. W. Kattawar, R. P. Lucht, T. Opatrny, H. Pilloff, A. Rebane, A. V. Sokolov, and M. S. Zubairy. FAST CARS: engineering a laser spectroscopic technique for rapid identification of bacterial spores. *Proceedings of the National Academy of Sciences*, 99(17):10994–1001, 2002.

[93] M. O. Scully and M. S. Zubairy. *Quantum Optics*. Cambridge University Press, Cambridge, MA, USA, 1997.

[94] S. L. Shapiro, J. A. Giordmaine, and K. W. Wecht. Stimulated Raman and Brillouin scattering with picosecond light pulses. *Physical Review Letters*, 19(19):1093–1095, 1967.

[95] M. Shirasaki. Large angular dispersion by a virtually imaged phased array and its application to a wavelength demultiplexer. *Optics Letters*, 21(5):366–368, 1996.

[96] A. E. Siegman. *Lasers*. University Science Books, Mill Valley, CA, USA, 1986.

[97] N. Skribanowitz, I. P. Herman, J. C. MacGillivray, and M. S. Feld. Observation of Dicke superradiance in optically pumped HF gas. *Physical Review Letters*, 30(8):309–312, 1973.

[98] Z. Steelman, Z. Meng, A. J. Traverso, and V. V. Yakovlev. Brillouin spectroscopy as a new method of screening for increased CSF total protein during bacterial meningitis. *Journal of Biophotonics*, 8(5):408–414, 2015.

[99] W. Steinbrecht, K.W. Rothe, and H. Walther. Lidar setup for daytime and nighttime probing of stratospheric ozone and measurements in polar and equatorial regions. *Applied Optics*, 28(17):3616–24, 1989.

[100] R. H. Stolen and J. E. Bjorkholm. Parametric amplification and frequency conversion in optical fibers. *IEEE Journal of Quantum Electronics*, 18(7):1062–1072, 1982.

[101] S. Suckewer and C. H. Skinner. Soft X-ray lasers and their applications. *Science*, 247(4950):1553–7, 1990.

[102] S. Suckewer, C. H. Skinner, H. Milchberg, C. Keane, and D. Voorhees. Amplification of stimulated soft X-ray emission in a confined plasma column. *Physical Review Letters*, 55(17):1753–1756, 1985.

[103] A. P. Sukhorukov and I. V. Tomov. Wave pattern of third optical harmonic generation in isotropic and anisotropic media. *Soviet Journal of Experimental and Theoretical Physics*, 31(5):872–9, 1970.

[104] S. Suntsov, D. Abdollahpour, D. G. Papazoglou, and S. Tzortzakis. Filamentation-induced third-harmonic generation in air via plasma-enhanced third-order susceptibility. *Physical Review A*, 81(3):2–5, 2010.

[105] A. A. Svidzinsky, L. Yuan, and M. O. Scully. Quantum amplification by superradiant emission of radiation. *Physical Review X*, 3(4):041001, 2013.

[106] A. J. Traverso, R. Sanchez-Gonzalez, L. Yuan, K. Wang, D. V. Voronine, A. M. Zheltikov, Y. Rostovtsev, V. A. Sautenkov, A. V. Sokolov, S. W. North, and M. O. Scully. Coherence brightened laser source for atmospheric remote sensing. *Proceedings of the National Academy of Sciences*, 109(38):15185–15190, 2012.

[107] Andrew J. Traverso, Jonathan V. Thompson, Zachary a. Steelman, Zhaokai Meng, Marlan O. Scully, and Vladislav V. Yakovlev. Dual Raman-Brillouin Microscope for Chemical and Mechanical Characterization and Imaging. *Analytical Chemistry*, 87(15):7519–7523, 2015.

[108] J. M. Vaughan and J. T. Randall. Brillouin scattering, density and elastic properties of the lens and cornea of the eye. *Nature*, 284(5755):489–491, 1980.

[109] C. Y. Wang, L. Diehl, A. Gordon, C. Jirauschek, F. X. Kärtner, A. Belyanin, D. Bour, S. Corzine, G. Höfler, M. Troccoli, J. Faist, and F. Capasso. Coherent

instabilities in a semiconductor laser with fast gain recovery. *Physical Review A*, 75(3):23–26, 2007.

[110] J. F. Ward and G. H. C. New. Optical third harmonic generation in gases by a focused laser beam. *Physical Review*, 185(1):57–72, 1969.

[111] U. Westblom, S. Agrup, M. Aldén, H. M. Hertz, and J. E. M. Goldsmith. Properties of laser-induced stimulated emission for diagnostic purposes. *Applied Physics B*, 50(6):487–497, 1990.

[112] E. J. Woodbury and W. K. Ng. Ruby laser operation in the near IR. *Proceedings of the Institute of Radio Engineers*, 50:2367, 1962.

[113] F. Y. Wu, S. Ezekiel, M. Ducloy, and B. R. Mollow. Observation of amplification in a strongly driven two-level atomic system at optical frequencies. *Physical Review Letters*, 38(I):1077–1080, 1977.

[114] S. Xiao, A. M. Weiner, and C. Lin. A dispersion law for virtually imaged phased-array spectral dispersers based on paraxial wave theory. *IEEE Journal of Quantum Electronics*, 40(4):420–426, 2004.

[115] V. V. Yakovlev, G. I. Petrov, H. F. Zhang, G. D. Noojin, M. L. Denton, R. J. Thomas, and M. O. Scully. Stimulated Raman scattering: old physics, new applications. *Journal of Modern Optics*, 56(18-19):1970–1973, 2009.

[116] A. P. Yalin, P. F. Barker, and R. B. Miles. Characterization of laser seeding by use of group-velocity dispersion in an atomic-vapor filter. *Optics Letters*, 25(7):502–4, 2000.

[117] L. Yuan, B. H. Hokr, A. J. Traverso, D. V. Voronine, Y. Rostovtsev, A. V. Sokolov, and M. O. Scully. Theoretical analysis of the coherence-brightened laser in air. *Physical Review A*, 87(2):023826, 2013.

[118] L. Yuan, A. A. Lanin, P. K. Jha, A. J. Traverso, D. V. Voronine, K. E. Dorfman, A. B. Fedotov, G. R. Welch, A. V. Sokolov, A. M. Zheltikov, and M. O. Scully. Coherent Raman Umklappscattering. *Laser Physics Letters*, 8(10):736–741, 2011.

[119] Luqi Yuan and Anatoly A. Svidzinsky. Gain without population inversion in a yoked superfluorescence scheme. *Physical Review A*, 85(March):1–7, 2012.

[120] Chang-Sheng Zha, Ho-kwang Mao, and Russell J. Hemley. Elasticity of MgO and a primary pressure scale to 55 GPa. *Proceedings of the National Academy of Sciences*, 97(25):13494–13499, 2000.

[121] A. M. Zheltikov. Coherent anti-Stokes Raman scattering: from proof-of-the-principle experiments to femtosecond CARS and higher order wave-mixing generalizations. *Journal of Raman Spectroscopy*, 31(8-9):653–667, 2000.

[122] A. Zibrov, M. Lukin, D. Nikonov, L. Hollberg, M. Scully, V. Velichansky, and H. Robinson. Experimental demonstration of laser oscillation without population inversion via quantum interference in Rb. *Physical Review Letters*, 75(8):1499–1502, 1995.

APPENDIX A

NUMERICAL METHOD FOR BRILLOUIN PEAK IDENTIFICATION

Shown below is the code used to identify peaks from the raw Brillouin data taken from the spectrometer. Moreso than the fitting, the correct identification of peaks within the data can be extremely challenging when there is a significant amount of noise. We refrain from trying to apply Lorentzian fits and focus more on extracting the information straight from the data. To accomplish this, various averaging filters are used to find the true peak centers at the closest pixel. While using a fitted Lorentzian has the potential for extrapolating a peak location better than the pixel resolution, in practice this rarely occurs as the Lorentzian fits, while good, never achieve a high enough accuracy especially with significant noise. Using the data itself allows us to avoid this issue and resolution better than the single level is achieved through our pixel to frequency mapping.

```
clear all
close all
clc
apple=0;
%%%New Camera
formatSpec = ;
delimiter = '\t';
FVBformatSpec = '%f%f%f%[^\n\r]';

vbegin=1;
%%vend is the number of pixels in the file footer
```

```
vend=300;
threshold=6.9;
offset=3110;
B_1=[0,150];
B_2=[410,720];
B_3=[1020,1300];
B_4=[1560,1850];
B_5=[2060,2290];
B_6=[2370,2680];
B_7=[offset+750,offset+950];
B_8=[offset+1400,offset+1600];
B_9=[offset+1960,offset+2120];
B_10=[offset+3210,3358];
%folder_name = 'D:\Research\Brillouin ...
    Data\2104_04_16\high_res_spectra'; %Full file extension for ...
    debugging purposes so you don't have to use uigetdir repeatedly
%folder_name = '/Users/kenmeissner/Desktop/rhodri/TAMU ...
    data/2015_05_02/Scan_2'; %%Mac
%%%
example=9;
example2=250;
example3=440;

matrixoutput=0;
ExtraBkgrnd=1;
modemedianFVB=0; %Only works when FVBread=0, If =1 then takes ...
    the mode of FVB, if =2 then takes the median, if any other ...
    number then just averages the FVB
range_suppression=1;
range_supptwo=1;
fliphoriz=1;
```

```
FVBread=1;
exp_windowrange_limiter=1; %prevents the exp_windowrange from ...
    expanding beyond the 2*MinPeakDistance
MinPeakDistance=44; %windowrange should be around 2x that of ...
    MinpeakDistance, or else can't properly converge
%N=21; %3rd order filtering
N=1; %3rd order filtering

windowrange=32; %Must be even number, sets the range that the ...
    averaging window scans over to find real peak
window=18; %Must be even number, number of points in average window
bkgrndfile=2;

%%%For everyday use, use uigetdir to open directory
folder_name = uigetdir;
bkgrndfilename='background';
if FVBread==1
    Filenames=dir(fullfile(folder_name,'FVB*.txt'));
    FVBbkgrndfilename=strcat('FVB*',bkgrndfilename,'*.txt');
    BackgroundFilenames = ...
        dir(fullfile(folder_name,FVBbkgrndfilename));
    %BackgroundFilenames = ...
        dir(fullfile(folder_name,'FVB*background*.txt'));
else
    Filenames=dir(fullfile(folder_name,'Image*.txt'));
    Imagebkgrndfilename=strcat('Image*',bkgrndfilename,'*.txt');
    BackgroundFilenames = ...
        dir(fullfile(folder_name,Imagebkgrndfilename));
    %BackgroundFilenames = ...
        dir(fullfile(folder_name,'Image*background02avg*.txt'));
end
```

```
NumofFiles=length(Filenames);
BGNumofFiles=length(BackgroundFilenames);
if BGNumofFiles==1
    bkgrndfile=1;
end
%Files=zeros{NumofFiles(1,1),1};
%%
iii=waitbar(0,'Loop 1');
tic
for i=1:NumofFiles
    waitbar(i/NumofFiles)
    if i==1
        Files={};
        NameofFile={};
    end
    splitone=regexp(Filenames(i).name,'Exp_', 'split');
    splittwo=regexp(splitone{2},'_x', 'split');
    splitthree=regexp(splittwo{2},'y', 'split');
    Position(i,1)=str2double(splitthree{1});
    splitfour=regexp(splitthree{2},'z', 'split');
    Position(i,2)=str2double(splitfour{1});
    splitfive=regexp(splitfour{2},'_Iteration_', 'split');
    Position(i,3)=str2double(splitfive{1});
    splitsix=regexp(splitfive{2},'_Temp', 'split');
    IterationNumber(i)=str2double(splitsix{1});
    splitseven=regexp(splitsix{2},'_C', 'split');
    TemperatureValue(i)=((str2double(splitseven{1}))/1000);
    NameofFile{i}=splittwo{1}; \%\%Creates a list of the ...
       filenames for reference
    if apple==1
        Files{i}=strcat(folder_name,'/',Filenames(i).name); %Mac
```

```
92      else
93          Files{i}=strcat(folder_name,'\',Filenames(i).name); %Win
94      end
95      fid=fopen(Files{i});
96      if FVBread==1
97          Data=textscan(fid,FVBformatSpec);
98      else
99          Data=textscan(fid,formatSpec);
100     end
101     fclose(fid);
102     [row,col]=size(Data);
103     if FVBread==1
104         OutputData(i,:,1)=cell2mat(Data(1,1));
105         collength=length(OutputData(i,:,1));
106         FVBOutputData(i,:,1)=1:collength;
107         FVBOutputData(i,:,2)=OutputData(i,:,1);
108         if fliphoriz==1
109             FVBOutputData(i,:,2)=fliplr(squeeze(FVBOutputData(i,:,2)));
110         end
111     else
112         for j=1:(col-1)
113             OutputData(i,:,j)=cell2mat(Data(1,j));
114         end
115         [filenum,vert,horiz]=size(OutputData(i,vbegin:vend,:));
116         if fliphoriz==1
117             OutputData(i,vbegin:vend,:) = ...
                    fliplr(squeeze(OutputData(i,vbegin:vend,:)));
118         end
119         FVBOutputData(i,:,1)=1:horiz;
120         if modemedianFVB==1
121             FVBOutputData(i,:,2)=mode(squeeze(OutputData(i,:,:)),1);
```

```
122         elseif modemedianFVB==2
123             FVBOutputData(i,:,2) = ...
                    median(squeeze(OutputData(i,:,:)),1);
124         else
125             FVBOutputData(i,:,2) = ...
                    sum(squeeze(OutputData(i,:,:)),1)/vert;
126         end
127     end
128 end
129
130 for ii=1:BGNumofFiles
131     if apple==1
132         BGFiles{ii}=strcat(folder_name,'/',BackgroundFilenames(ii).name); ...
                %Mac
133     else
134         BGFiles{ii}=strcat(folder_name,'\',BackgroundFilenames(ii).name); ...
                %Win
135     end
136     BGfid=fopen(BGFiles{ii});
137     if FVBread==1
138         BGData=textscan(BGfid,FVBformatSpec);
139     else
140         BGData=textscan(BGfid,formatSpec);
141     end
142     fclose(BGfid);
143     [BGrow,BGcol]=size(BGData);
144     if FVBread==1
145         BGOutputData(ii,:,1)=cell2mat(BGData(1,1));
146         BGcollength=length(BGOutputData(ii,:,1));
147         BGFVBOutputData(ii,:,1)=1:BGcollength;
148         BGFVBOutputData(ii,:,2)=BGOutputData(ii,:,1);
```

```
149         if fliphoriz==1
150             BGFVBOutputData(ii,:,2) = ...
                    fliplr(squeeze(BGFVBOutputData(ii,:,2)));
151         end
152     else
153         for jj=1:(BGcol-1)
154             BGOutputData(ii,:,jj)=cell2mat(BGData(1,jj));
155         end
156         [BGfilenum,BGvert,BGhoriz] = ...
                size(BGOutputData(ii,vbegin:vend,:));
157         if fliphoriz==1
158             BGOutputData(ii,vbegin:vend,:) = ...
                    fliplr(squeeze(BGOutputData(ii,vbegin:vend,:)));
159         end
160         BGFVBOutputData(ii,:,1)=1:BGhoriz;
161         BGFVBOutputData(ii,:,2) = ...
                sum(squeeze(BGOutputData(ii,:,:)),1)/BGvert;
162     end
163 end
164 close(iii)
165
166 NameofFile=transpose(NameofFile);
167 Bkgrnd=BGFVBOutputData(bkgrndfile,:,2);
168
169 kkk=waitbar(0,'Loop 2');
170 for kk=1:NumofFiles
171     waitbar(kk/NumofFiles)
172     FVBOutputData(kk,:,2)=FVBOutputData(kk,:,2)-Bkgrnd;
173     if ExtraBkgrnd==1
174         if kk==1
175             if mod(length(FVBOutputData(kk,:,2)),2)==0
```

```
176                 Bkgrndlength=length(FVBOutputData(kk,:,2))-1;
177             else
178                 Bkgrndlength=length(FVBOutputData(kk,:,2));
179             end
180         end
181         VVV = ...
                polyfit(1:length(FVBOutputData(kk,:,2)),FVBOutputData(kk,:,2),3);
182         AAA=polyval(VVV,1:length(FVBOutputData(kk,:,2)));
183         %AAA=sgolayfilt(squeeze(FVBOutputData(kk,:,2)),3,Bkgrndlength);
184         BBB=max(AAA);
185         FVBOutputData(kk,:,2) = ...
                FVBOutputData(kk,:,2)-median(FVBOutputData(kk,:,2))*AAA./BBB;
186     end
187     SmoothFVBOutputData(kk,:,1)=FVBOutputData(kk,:,1);
188     if N==1
189         SmoothFVBOutputData(kk,:,2)=FVBOutputData(kk,:,2);   % ...
                NO filter
190     else
191         SmoothFVBOutputData(kk,:,2)=sgolayfilt(FVBOutputData(kk,:,2),3,N); ...
                 % Apply 3rd-order filter
192     end
193     if ExtraBkgrnd~=1
194         SmoothFVBOutputData(kk,:,2) = ...
                SmoothFVBOutputData(kk,:,2)-median(SmoothFVBOutputData(kk,500:2200,2));
195     end
196     %SmoothFVBOutputData(kk,:,2) = ...
           SmoothFVBOutputData(kk,:,2)-min(SmoothFVBOutputData(kk,500:3000,2));
197     if mean(SmoothFVBOutputData(kk,:,2))~=0
198         SmoothFVBOutputData(kk,:,2) = ...
                (SmoothFVBOutputData(kk,:,2)/max(SmoothFVBOutputData(kk,:,2)))*100;
199     end
```

```
200     % find all peaks and locations
201     %[pks{kk}, locs{kk}]=findpeaks (FVBOutputData(kk,:,2));
202     %[rows_pks, columns_pks] = size(locs{kk});
203
204     [spks{kk}, slocs{kk}]=findpeaks (SmoothFVBOutputData(kk,:,2));
205     [srows_pks, scolumns_pks] = size(slocs{kk});
206     if kk==1
207         %create dummy matrices
208         Real_locs=[];
209         Real_pks=[];
210         Real_slocs=[];
211         Real_spks=[];
212     end
213     %find peaks for smoothed set above certain threshold
214     for i = 1:scolumns_pks
215         if i==1
216             j=1;
217         end
218         if spks{kk}(i) >threshold
219         %if spks{kk}(i) >(std(SmoothFVBOutputData(kk,:,2)) + ...
                median(SmoothFVBOutputData(kk,:,2)))
220             Real_spks(kk,j)=spks{kk}(i);
221             Real_slocs(kk,j)=slocs{kk}(i);
222             j=j+1;
223         end
224     end
225 end
226 close(kkk)
227 filestoprocess=length(Real_slocs(:,1));
228 if range_suppression==1
229     for hh1=1:filestoprocess%NumofFiles
```

```
230         for ee=1:length(Real_slocs(hh1,:))
231             if ee==1
232                 nn=1;
233             end
234             if Real_slocs(hh1,ee)>=B_1(1) && ...
                    Real_slocs(hh1,ee)<=B_1(2)
235             elseif Real_slocs(hh1,ee)>=B_2(1) && ...
                    Real_slocs(hh1,ee)<=B_2(2)
236             elseif Real_slocs(hh1,ee)>=B_3(1) && ...
                    Real_slocs(hh1,ee)<=B_3(2)
237             elseif Real_slocs(hh1,ee)>=B_4(1) && ...
                    Real_slocs(hh1,ee)<=B_4(2)
238             elseif Real_slocs(hh1,ee)>=B_5(1) && ...
                    Real_slocs(hh1,ee)<=B_5(2)
239             elseif Real_slocs(hh1,ee)>=B_6(1) && ...
                    Real_slocs(hh1,ee)<=B_6(2) && range_supptwo==1
240             elseif Real_slocs(hh1,ee)>=B_7(1) && ...
                    Real_slocs(hh1,ee)<=B_7(2) && range_supptwo==1
241             elseif Real_slocs(hh1,ee)>=B_8(1) && ...
                    Real_slocs(hh1,ee)<=B_8(2) && range_supptwo==1
242             elseif Real_slocs(hh1,ee)>=B_9(1) && ...
                    Real_slocs(hh1,ee)<=B_9(2) && range_supptwo==1
243             elseif Real_slocs(hh1,ee)>=B_10(1) && ...
                    Real_slocs(hh1,ee)<=B_10(2) && range_supptwo==1
244             elseif Real_slocs(hh1,ee)>0
245                 SReal_slocs(hh1,nn)=Real_slocs(hh1,ee);
246                 SReal_spks(hh1,nn)=Real_spks(hh1,ee);
247                 nn=nn+1;
248             end
249         end
250     end
```

```
251     clearvars Real_slocs Real_spks
252     Real_slocs=SReal_slocs;
253     Real_spks=SReal_spks;
254     clearvars SReal_slocs SReal_spks
255 end
256
257 %std(SmoothFVBOutputData(example2,:,2)) + ...
       median(SmoothFVBOutputData(example2,:,2))
258 %%Filters using an averaging window, finds more accurate centers ...
       of peaks as
259 %%well as eliminating duplicate peaks
260 hhh=waitbar(0,'Loop 3');
261 for hh=1:filestoprocess%NumofFiles
262     waitbar(hh/NumofFiles)
263     clearvars holder_slocs holder_spks
264     %holder_spks=Real_spks(hh,:);
265     holder_slocs=Real_slocs(hh,:);
266     countah=0;
267     while (any(abs(diff(holder_slocs)) > 0) && countah<200 && ...
           any(abs(diff(holder_slocs)) < MinPeakDistance)) || ...
           (countah==0 && any(abs(diff(holder_slocs)) > 0) && ...
           countah<200)
268         countah=countah+1;
269         exp_windowrange=countah*windowrange;
270         if exp_windowrange>(2*MinPeakDistance) && ...
               exp_windowrange_limiter==1
271             exp_windowrange=2*MinPeakDistance;
272         end
273         for ff=1:length(holder_slocs)
274             if ff==1
275                 ww=1;
```

```
276             end
277             peakvalue=holder_slocs(ff);
278             if peakvalue>0
279                 for dd=1:exp_windowrange
280                     if dd==1
281                         maxaverage=0;
282                         averagevalue=0;
283                         maxlocation=0;
284                     end
285                     if ...
                            (peakvalue-(exp_windowrange/2)-window/2+dd) ...
                            >= 1 && (peakvalue-(exp_windowrange/2) + ...
                            window/2 + dd) <= ...
                            length(SmoothFVBOutputData(hh, :, 2))
286                         averagevalue = ...
                                mean(SmoothFVBOutputData(hh, ...
                                (peakvalue-(exp_windowrange/2)-window/2 ...
                                + dd):(peakvalue - ...
                                (exp_windowrange/2) + window/2 + dd), ...
                                2));
287                         if averagevalue>maxaverage
288                             maxaverage=averagevalue;
289                             maxlocation=peakvalue-(exp_windowrange/2)+dd;
290                             maxlocation=round(maxlocation);
291                         end
292                     elseif ...
                            (peakvalue-(exp_windowrange/2)-window/2+dd) ...
                            < 1 && (peakvalue-(exp_windowrange/2)+dd) ...
                            >= 1
293                         averagevalue = ...
                                mean(SmoothFVBOutputData(hh, ...
```

```
                    1:(peakvalue-(exp_windowrange/2) + ...
                    window/2 + dd), 2));
294                 if averagevalue > maxaverage
295                     maxaverage = averagevalue;
296                     maxlocation = ...
                            peakvalue-(exp_windowrange/2) + dd;
297                     maxlocation = round(maxlocation);
298                 end
299             elseif ...
                    (peakvalue-(exp_windowrange/2)+window/2+dd) ...
                    > length(SmoothFVBOutputData(hh,:,2)) && ...
                    (peakvalue-(exp_windowrange/2)+dd) <= ...
                    length(SmoothFVBOutputData(hh,:,2))
300                 averagevalue = ...
                        mean(SmoothFVBOutputData(hh, ...
                        (peakvalue - (exp_windowrange/2) - ...
                        window/2 + ...
                        dd):length(SmoothFVBOutputData(hh, :, ...
                        2)), 2));
301                 if averagevalue > maxaverage
302                     maxaverage = averagevalue;
303                     maxlocation = ...
                            peakvalue-(exp_windowrange/2) + dd;
304                     maxlocation = round(maxlocation);
305                 end
306             end
307         end
308     end
309     if dd == exp_windowrange
310         if maxlocation == 0
311             maxlocation = 1;
```

```
312                 end
313                 Temp_slocs(ww) = maxlocation;
314                 Temp_spks(ww) = ...
                        SmoothFVBOutputData(hh,maxlocation,2);
315                 ww=ww+1;
316             end
317             if ff==length(holder_slocs)
318                 clearvars holder_slocs holder_spks
319                 [holder_slocs,TempIndex,holderIndex] = ...
                        unique(Temp_slocs,'stable');
320                 %Countah_holder_slocs(countah,1:length(holder_slocs)) ...
                        = holder_slocs;
321                 holder_spks = Temp_spks(TempIndex);
322                 clearvars Temp_slocs Temp_spks
323             end
324         end
325     end
326    Countahvector(hh)=countah;
327         if sum(holder_slocs)>0
328          final_length=length(unique(holder_slocs));
329          %Final_slocs(hh,1:final_length)=unique(Temp_slocs(hh,:),'stable');
330          [Final_slocs(hh,1:final_length),holderIndex,FinalIndex] ...
                = unique(holder_slocs,'stable');
331          %Final_spks(hh,1:final_length)=unique(Temp_spks(hh,:),'stable');
332          Final_spks(hh,1:final_length)=holder_spks(holderIndex);
333          clearvars holder_slocs holder_spks
334          holder_slocs=Final_slocs(hh,1:final_length);
335     end
336 end
337 close(hhh)
338 %%Filters out any peaks near Rayleigh peak, The B_x variables ...
```

```
    above specify
%%these suppression windows
if range_suppression==1
    for hh2=1:NumofFiles
        for ee=1:length(Final_slocs(hh2,:))
            if ee==1
                nn=1;
            end
            if Final_slocs(hh2,ee)>=B_1(1) && ...
               Final_slocs(hh2,ee)<=B_1(2)
            elseif Final_slocs(hh2,ee)>=B_2(1) && ...
               Final_slocs(hh2,ee)<=B_2(2)
            elseif Final_slocs(hh2,ee)>=B_3(1) && ...
               Final_slocs(hh2,ee)<=B_3(2)
            elseif Final_slocs(hh2,ee)>=B_4(1) && ...
               Final_slocs(hh2,ee)<=B_4(2)
            elseif Final_slocs(hh2,ee)>=B_5(1) && ...
               Final_slocs(hh2,ee)<=B_5(2)
            elseif Final_slocs(hh2,ee)>=B_6(1) && ...
               Final_slocs(hh2,ee)<=B_6(2) && range_supptwo==1
            elseif Final_slocs(hh2,ee)>=B_7(1) && ...
               Final_slocs(hh2,ee)<=B_7(2) && range_supptwo==1
            elseif Final_slocs(hh2,ee)>=B_8(1) && ...
               Final_slocs(hh2,ee)<=B_8(2) && range_supptwo==1
            elseif Final_slocs(hh2,ee)>=B_9(1) && ...
               Final_slocs(hh2,ee)<=B_9(2) && range_supptwo==1
            elseif Final_slocs(hh2,ee)>=B_10(1) && ...
               Final_slocs(hh2,ee)<=B_10(2) && range_supptwo==1
            elseif Final_slocs(hh2,ee)>0
                SFinal_slocs(hh2,nn)=Final_slocs(hh2,ee);
                SFinal_spks(hh2,nn)=Final_spks(hh2,ee);
```

```
359                 nn=nn+1;
360             end
361         end
362     end
363     clearvars Final_slocs Final_spks
364     Final_slocs=SFinal_slocs;
365     Final_spks=SFinal_spks;
366     clearvars SFinal_slocs SFinal_spks
367 end
368
369
370 %%Example plots, change the example variable to select which ...
       one, look at
371 %%NameofFile variable to know the dataset each number ...
       corresponds to
372 figure(1);
373 plot(SmoothFVBOutputData(example,:,1), ...
       SmoothFVBOutputData(example,:,2), Final_slocs(example,:), ...
       Final_spks(example,:), 'o')
374 figure(2);
375 plot(SmoothFVBOutputData(example2,:,1), ...
       SmoothFVBOutputData(example2,:,2), Final_slocs(example2,:), ...
       Final_spks(example2,:), 'o')
376 figure(3);
377 plot(SmoothFVBOutputData(example3,:,1), ...
       SmoothFVBOutputData(example3,:,2), Final_slocs(example3,:), ...
       Final_spks(example3,:), 'o')
378 figure(4);
379 plot(SmoothFVBOutputData(example,:,1), ...
       SmoothFVBOutputData(example,:,2), ...
       SmoothFVBOutputData(example2,:,1), ...
```

```
    SmoothFVBOutputData(example2,:,2), Final_slocs(example2,:), ...
    Final_spks(example2,:), 'o')
figure(5);
plot(SmoothFVBOutputData(example,:,1), ...
    SmoothFVBOutputData(example,:,2), ...
    SmoothFVBOutputData(example3,:,1), ...
    SmoothFVBOutputData(example3,:,2), Final_slocs(example3,:), ...
    Final_spks(example3,:), 'o')
figure(6);plot(SmoothFVBOutputData(example2,:,1), ...
    SmoothFVBOutputData(example2,:,2), ...
    SmoothFVBOutputData(example3,:,1), ...
    SmoothFVBOutputData(example3,:,2), Final_slocs(example3,:), ...
    Final_spks(example3,:), 'o')

for kkk=1:filestoprocess%NumofFiles
    endval=length(Final_slocs(kkk,:));
    peaksmatrix(kkk,1:endval,2)=transpose(Final_spks(kkk,:));
    peaksmatrix(kkk,1:endval,1)=transpose(Final_slocs(kkk,:));
end
toc
```

APPENDIX B

NUMERICAL METHOD FOR BRILLOUIN SPECTRAL FITTING

Listed below is an excerpt of matlab code used to accurately fit the peaks of the Brillouin spectra to frequency shifts. As mentioned earlier in the text, this fitting is achieved by fitting the parameters m and θ_i, the diffraction order number and the angle of incidence of the input light with the normal of the VIPA. The fitting approach used here uses a total of 4 identical loops to converge on the best fit solution by shrinking shrinking the window and step size of the parameters with each subsequent loop (only the first loop is shown below).

```
1 clearvars OutputSpectraNew SelectedNameofFileNew ...
      SelectedNameofFileHeaderNew SelectedTemperatureValueNew ...
      SelectedIterationNumberNew SelectedTemperatureValueHeaderNew ...
      SelectedIterationNumberHeaderNew
2 clearvars OutputSpectraNamesNew Total2columnTrimmed ...
      AS2columnTrimmed S2columnTrimmed Total2column AS2column ...
      S2column TotalScaling ASScaling SScaling
3 clearvars TotalMval ASMval SMval TotalFinalShiftsAbsolute ...
      ASFinalShiftsAbsolute SFinalShiftsAbsolute
4 clearvars TotalFinalShiftsAbsoluteAVERAGE ...
      ASFinalShiftsAbsoluteAVERAGE SFinalShiftsAbsoluteAVERAGE ...
      All2columnheader
5 clearvars TotalFinalangleAbsolute SFinalangleAbsolute ...
      ASFinalangleAbsolute TotalFinalstdAbsolute ASFinalstdAbsolute ...
      SFinalstdAbsolute
6 clearvars OutputSpectraNewTrimmed OutputSpectraNamesNewTrimmed
```

```
Totalchoice=1;
differencefit=0;
splittingsfit=1;
FirstPeakOnLeftIsStokes=0;
NumofLevels=4;
ScaleAll=1;
firstafterbackground=2;
NumFSR=4;
%datasets=[firstafterbackground:68,165:185];
%datasets=[4,5,6,11,12,13,22,23,24,25,26,27];

[TotalDataSets2,TotalPixels,TotalCols]=size(SmoothFVBOutputData);
[TotalDataSets,Totaldummy1,Totaldummy2]=size(peaksmatrix);
Pixvector=1:TotalPixels;
%datasets=2:TotalDataSets;
if ScaleAll==1
    datasets=firstafterbackground:TotalDataSets;
end
MaxDev=.0055;
pixelsize=6.48*10^(-6);
%pixelsize=5.39*10^(-6); %%Old Camera
c=2.99792458*10^8; %speed of light (m/s)
%%%VIPA parameters
R=.98; %backside reflectivity
r=.995; %frontside reflectivity
W=3*10^(-3); %beam diameter (m)
F=1; %output lens focal length  (m)
t=5*10^(-3); %thickness of VIPA (m)
%%%%VIPA Index of Refraction Calculation
%n=1.45406; %index of refractiion (fused silica)
lambda=780.24*10^(-9); %center wavelength (m)
```

```
fshift = 10*10^9; %simulated brill shift (Hz)
upperfreq = c/lambda+fshift; %simulated brill frequency (Hz)
lowerfreq = c/lambda-fshift; %simulated brill frequency (Hz)
lambdalower = c/upperfreq; %simulated brill wavelength (m)
lambdaupper = c/lowerfreq; %simulated brill wavelength (m)
SB=[0.696166300,0.407942600,0.897479400];
SC=[4.67914826*10^(-15),1.35120631*10^(-14),97.9340025*10^(-12)];
indexfun=@(lambda) sqrt(1 + ...
    ((SB(1)).*(lambda.^2)/(lambda.^2-SC(1))) + ...
    ((SB(2)).*(lambda.^2)./(lambda.^2-SC(2))) + ...
    ((SB(3)).*(lambda.^2)./(lambda.^2-SC(3))));
Dindexfun=@(lambda) ...
    (1./indexfun(lambda)).*(-1).*((SB(1).*SC(1).*lambda./(lambda.^2-SC(1)).^2) ...
    + (SB(2).*SC(2).*lambda./(lambda.^2 - SC(2)).^2) + ...
    (SB(3).*SC(3).*lambda./(lambda.^2 - SC(3)).^2));
ng=@(lambda) indexfun(lambda)-lambda.*Dindexfun(lambda);
n=ng(lambda);
%%%Functions
k= @(x) 2*pi/x; %wavenumber
TinF=@(n,theta1) asin((1./n).*sin(theta1));
linearfunc=@(n,theta1) ...
    (tan(TinF(n,theta1)).*(cos(theta1))./(n.*cos(TinF(n,theta1)));
rootfunc=@(t,n,theta1) 2*t.*n.*cos(TinF(n,theta1));
delfreqfunc = @(m,t,n,F,x,theta1) m*c*( ...
    (1/2).*((1./n).^2).*((x./F).^2) + ...
    linearfunc(n,theta1).*(x./F) )./ ((rootfunc(t,n,theta1)).*(1 ...
    - linearfunc(n,theta1).*(x./F) - ...
    (1/2).*((1./n).^2).*((x/F).^2)));
Freqfunc = @(m,t,n,F,x,theta1) m.*c*(1)./ ...
    ((rootfunc(t,n,theta1)).*(1 - linearfunc(n,theta1).*(x./F) - ...
    (1/2).*((1/n).^2).*((x./F).^2)));
```

```
lambdafunc=@(m,t,n,F,x,theta1) c./Freqfunc(m,t,n,F,x,theta1);

trialanglelow=0.1;
trialanglestep=.005;
trialanglehigh=0.45;
% trialanglelow=0; trialanglestep=.05; trialanglehigh=2.5;
trialangledeg=trialanglelow:trialanglestep:trialanglehigh;
trialangle=pi*trialangledeg./180;
totalpts=length(trialangledeg);
%beginningM=18400;
beginningM=18225;
offset2=offset;
offsetval=-.02;
%offsetval=.06;
tt=1;
stepsize=100;
%stepsize=0;
iii=waitbar(0,'Looping');
tic
if NumFSR>3 && FirstPeakOnLeftIsStokes==1
    AS2column=zeros(length(datasets),9);
    S2column=zeros(length(datasets),9);
    Total2column=zeros(length(datasets),9);
else
    AS2column=zeros(length(datasets),8);
    S2column=zeros(length(datasets),8);
    Total2column=zeros(length(datasets),8);
end
for dw=1:length(datasets)
    waitbar(dw/length(datasets))
    clearvars delfreqpeaks delfreqpeaks1 delfreqpeaks2 ...
```

```
    delfreqpeaks3 Freqpeaks Freqpeaks1 Freqpeaks2 Freqpeaks3 ...
    deviations deviations1 deviations2 deviations3 ...
    ASdeviations ASdeviations1 ASdeviations2 ASdeviations3 ...
    Sdeviations Sdeviations1 Sdeviations2 Sdeviations3 ...
    Totaldeviations Totaldeviations1 Totaldeviations2 ...
    Totaldeviations3
87  clearvars diffdelfreqpeaks diffdelfreqpeaks1 ...
    diffdelfreqpeaks2 diffdelfreqpeaks3 normdiffdelfreqpeaks ...
    normdiffdelfreqpeaks1 normdiffdelfreqpeaks2 ...
    normdiffdelfreqpeaks3 DiffFreqdiff DiffFreqdiff1 ...
    DiffFreqdiff2 DiffFreqdiff3
88  clearvars ASFreqdiff ASFreqdiff1 ASFreqdiff2 ASFreqdiff3 ...
    SFreqdiff SFreqdiff1 SFreqdiff2 SFreqdiff3 TotalFreqdiff ...
    TotalFreqdiff1 TotalFreqdiff2 TotalFreqdiff3
89  clearvars diffdelfreqpeaksAbs diffdelfreqpeaksAbs1 ...
    diffdelfreqpeaksAbs2 diffdelfreqpeaksAbs3 Mval Mval1 ...
    Mval2 Mval3
90  clearvars TotalFinalstd TotalFinalstd1 TotalFinalstd2 ...
    TotalFinalstd3 TotalFinalangle TotalFinalangle1 ...
    TotalFinalangle2 TotalFinalangle3
91  clearvars trialangledeg1 trialangledeg2 trialangledeg3
92  SelectedNameofFileNew{dw}=NameofFile{datasets(dw)};
93  SelectedNameofFileHeaderNew{2*dw-1}=NameofFile{datasets(dw)};
94  SelectedNameofFileHeaderNew{2*dw}=NameofFile{datasets(dw)};
95  SelectedTemperatureValueNew(dw,1)=TemperatureValue(datasets(dw));
96  SelectedIterationNumberNew(dw)=IterationNumber(datasets(dw));
97  SelectedTemperatureValueHeaderNew(2*dw)=TemperatureValue(datasets(dw));
98  SelectedIterationNumberHeaderNew(2*dw)=IterationNumber(datasets(dw));
99
100 %%%%%%%%%%%%%%FIRST
101 %%%%%%%%%%%%%%LOOP%%%%%%%%%%%%%
```

```
102     for jj=1:31
103         Mvalue=beginningM+stepsize*(jj-1);
104         Mval(jj,1)=Mvalue;
105         for j = 1:(length(peaksmatrix(datasets(dw),:,1))/2)
106             if FirstPeakOnLeftIsStokes==1
107                 delfreqpeaks(2*j-1,1:totalpts) = ...
                        delfreqfunc(Mvalue-(j-1), t, n, F, ...
                        peaksmatrix(datasets(dw), 2*j-1, 1)*pixelsize ...
                        - offsetval*tt, trialangle);
108                 delfreqpeaks(2*j,1:totalpts) = ...
                        delfreqfunc(Mvalue-(j-1), t, n, F, ...
                        peaksmatrix(datasets(dw), 2*j, 1)*pixelsize - ...
                        offsetval*tt, trialangle);
109             else
110                 delfreqpeaks(2*j-1,1:totalpts) = ...
                        delfreqfunc(Mvalue-(j), t, n, F, ...
                        peaksmatrix(datasets(dw), 2*j, 1)*pixelsize - ...
                        offsetval*tt, trialangle);
111                 if j ~= length(peaksmatrix(datasets(dw),:,1))/2
112                     delfreqpeaks(2*j,1:totalpts) = ...
                            delfreqfunc(Mvalue-(j), t, n, F, ...
                            peaksmatrix(datasets(dw), 2*j+1, ...
                            1)*pixelsize - offsetval*tt, trialangle);
113                 end
114             end
115             if FirstPeakOnLeftIsStokes==1
116                 Freqpeaks(2*j-1,1:totalpts) = ...
                        Freqfunc(Mvalue-(j-1), t, n, F, ...
                        peaksmatrix(datasets(dw), 2*j-1, 1)*pixelsize ...
                        - offsetval*tt, trialangle);
117                 Freqpeaks(2*j,1:totalpts) = ...
```

```
                    Freqfunc(Mvalue-(j-1), t, n, F, ...
                    peaksmatrix(datasets(dw), 2*j, 1)*pixelsize - ...
                    offsetval*tt, trialangle);
118             else
119                 Freqpeaks(2*j-1,1:totalpts) = ...
                    Freqfunc(Mvalue-(j-1), t, n, F, ...
                    peaksmatrix(datasets(dw), 2*j-1, 1)*pixelsize ...
                    - offsetval*tt, trialangle);
120                 Freqpeaks(2*j,1:totalpts) = Freqfunc(Mvalue-(j), ...
                    t, n, F, peaksmatrix(datasets(dw), 2*j, ...
                    1)*pixelsize - offsetval*tt, trialangle);
121             end
122         end
123         for u=1:(floor(length(delfreqpeaks(:,1))/2))
124             diffdelfreqpeaks(u,:)=delfreqpeaks(2*u,:)-delfreqpeaks(2*u-1,:);
125             diffdelfreqpeaksAbs(u,:)=Freqpeaks(2*u,:)-Freqpeaks(2*u-1,:);
126             if u==(floor(length(delfreqpeaks(:,1))/2)) && ...
                    differencefit==1
127                 for uu=1:(floor(length(delfreqpeaks(:,1))/2))
128                     normdiffdelfreqpeaks(uu,:) = ...
                            diffdelfreqpeaks(uu,:)./mean(diffdelfreqpeaks);
129                 end
130             end
131         end
132         if differencefit==1
133             deviations=std(normdiffdelfreqpeaks,0,1);
134             [stdval(jj,:),stdindex(jj,:)]=min(deviations);
135             Finalfreqshifts(:,jj) = ...
                    (diffdelfreqpeaks(:,stdindex(jj,:))./2).*10^(-9);
136             Finalstd(jj,tt)=std(Finalfreqshifts(:,jj));
137             Finalangle(jj,tt)=trialangledeg(stdindex(jj,:));
```

```
138         end
139         %%Diff Freq Fitting
140         if FirstPeakOnLeftIsStokes==1
141             DiffFreqdiff(1,:)=abs(Freqpeaks(1,:)-Freqpeaks(2,:));
142             DiffFreqdiff(2,:)=abs(Freqpeaks(3,:)-Freqpeaks(4,:));
143             DiffFreqdiff(3,:)=abs(Freqpeaks(5,:)-Freqpeaks(6,:));
144             if NumFSR>3
145                 DiffFreqdiff(4,:)=abs(Freqpeaks(7,:)-Freqpeaks(8,:));
146             end
147         else
148             DiffFreqdiff(1,:)=abs(Freqpeaks(2,:)-Freqpeaks(3,:));
149             DiffFreqdiff(2,:)=abs(Freqpeaks(4,:)-Freqpeaks(5,:));
150             DiffFreqdiff(3,:)=abs(Freqpeaks(6,:)-Freqpeaks(7,:));
151         end
152         %%anti-Stokes Fitting
153         ASFreqdiff(1,:)=abs(Freqpeaks(2,:)-Freqpeaks(4,:));
154         ASFreqdiff(2,:)=abs(Freqpeaks(2,:)-Freqpeaks(6,:));
155         ASFreqdiff(3,:)=abs(Freqpeaks(4,:)-Freqpeaks(6,:));
156         if NumFSR>3
157             ASFreqdiff(4,:)=abs(Freqpeaks(2,:)-Freqpeaks(8,:));
158             ASFreqdiff(5,:)=abs(Freqpeaks(4,:)-Freqpeaks(8,:));
159             ASFreqdiff(6,:)=abs(Freqpeaks(6,:)-Freqpeaks(8,:));
160         end
161         ASdeviations=std(ASFreqdiff,0,1);
162         [ASstdval(jj,:),ASstdindex(jj,:)]=min(ASdeviations);
163         %minASFreqdiff(:,jj)=ASFreqdiff(:,ASstdindex(jj,:));
164         ASFinalfreqshifts(:,jj) = ...
               (diffdelfreqpeaks(:,ASstdindex(jj,:))./2).*10^(-9);
165         %ASFinalfreqshiftsDiff(:,jj) = ...
               (DiffFreqdiff(:,ASstdindex(jj,:))./2).*10^(-9);
166         ASFinalstd(jj,tt)=std(ASFinalfreqshifts(:,jj));
```

```
167         %ASFinalDiffstd(jj,tt)=std(ASFinalfreqshiftsDiff(:,jj));
168         ASFinalangle(jj,tt)=trialangledeg(ASstdindex(jj,:));
169         %%%Stokes Fitting
170         SFreqdiff(1,:)=abs(Freqpeaks(1,:)-Freqpeaks(3,:));
171         SFreqdiff(2,:)=abs(Freqpeaks(1,:)-Freqpeaks(5,:));
172         SFreqdiff(3,:)=abs(Freqpeaks(3,:)-Freqpeaks(5,:));
173         if NumFSR>3
174             SFreqdiff(4,:)=abs(Freqpeaks(1,:)-Freqpeaks(7,:));
175             SFreqdiff(5,:)=abs(Freqpeaks(3,:)-Freqpeaks(7,:));
176             SFreqdiff(6,:)=abs(Freqpeaks(5,:)-Freqpeaks(7,:));
177         end
178         Sdeviations=std(SFreqdiff,0,1);
179         [Sstdval(jj,:),Sstdindex(jj,:)]=min(Sdeviations);
180         %minSFreqdiff(:,jj)=SFreqdiff(:,Sstdindex(jj,:));
181         SFinalfreqshifts(:,jj) = ...
               (diffdelfreqpeaks(:,Sstdindex(jj,:))./2).*10^(-9);
182         %SFinalfreqshiftsDiff(:,jj) = ...
               (DiffFreqdiff(:,Sstdindex(jj,:))./2).*10^(-9);
183         SFinalstd(jj,tt)=std(SFinalfreqshifts(:,jj));
184         %SFinalDiffstd(jj,tt)=std(SFinalfreqshiftsDiff(:,jj));
185         SFinalangle(jj,tt)=trialangledeg(Sstdindex(jj,:));
186
187         TotalFreqdiff(1,:)=ASFreqdiff(1,:);
188         TotalFreqdiff(2,:)=ASFreqdiff(2,:);
189         TotalFreqdiff(3,:)=ASFreqdiff(3,:);
190         TotalFreqdiff(4,:)=SFreqdiff(1,:);
191         TotalFreqdiff(5,:)=SFreqdiff(2,:);
192         TotalFreqdiff(6,:)=SFreqdiff(3,:);
193         if splittingsfit==1
194             TotalFreqdiff(7,:)=abs(DiffFreqdiff(1,:)-DiffFreqdiff(2,:));
195             TotalFreqdiff(8,:)=abs(DiffFreqdiff(1,:)-DiffFreqdiff(3,:));
```

```
196             TotalFreqdiff(9,:)=abs(DiffFreqdiff(2,:)-DiffFreqdiff(3,:));
197         end
198         if NumFSR>3
199             if splittingsfit==1
200                 TotalFreqdiff(10,:)=ASFreqdiff(4,:);
201                 TotalFreqdiff(11,:)=ASFreqdiff(5,:);
202                 TotalFreqdiff(12,:)=ASFreqdiff(6,:);
203                 TotalFreqdiff(13,:)=SFreqdiff(4,:);
204                 TotalFreqdiff(14,:)=SFreqdiff(5,:);
205                 TotalFreqdiff(15,:)=SFreqdiff(6,:);
206                 if FirstPeakOnLeftIsStokes==1
207                     TotalFreqdiff(16,:) = ...
                        abs(DiffFreqdiff(1,:)-DiffFreqdiff(4,:));
208                     TotalFreqdiff(17,:) = ...
                        abs(DiffFreqdiff(2,:)-DiffFreqdiff(4,:));
209                     TotalFreqdiff(18,:) = ...
                        abs(DiffFreqdiff(3,:)-DiffFreqdiff(4,:));
210                 end
211             else
212                 TotalFreqdiff(7,:)=ASFreqdiff(4,:);
213                 TotalFreqdiff(8,:)=ASFreqdiff(5,:);
214                 TotalFreqdiff(9,:)=ASFreqdiff(6,:);
215                 TotalFreqdiff(10,:)=SFreqdiff(4,:);
216                 TotalFreqdiff(11,:)=SFreqdiff(5,:);
217                 TotalFreqdiff(12,:)=SFreqdiff(6,:);
218             end
219         end
220         Totaldeviations=std(TotalFreqdiff,0,1);
221         [Totalstdval(jj,:),Totalstdindex(jj,:)]=min(Totaldeviations);
222         %minTotalFreqdiff(:,jj)=TotalFreqdiff(:,Totalstdindex(jj,:));
223         TotalFinalfreqshifts(:,jj) = ...
```

```
            (diffdelfreqpeaks(:,Totalstdindex(jj,:))./2).*10^(-9);
224         %TotalFinalfreqshiftsDiff(:,jj) = ...
            (DiffFreqdiff(:,Totalstdindex(jj,:))./2).*10^(-9);
225         TotalFinalstd(jj,tt)=std(TotalFinalfreqshifts(:,jj));
226         %TotalFinalDiffstd(jj,tt)=std(TotalFinalfreqshiftsDiff(:,jj));
227         TotalFinalangle(jj,tt)=trialangledeg(Totalstdindex(jj,:));
228     end
```